Università degli Studi di Torino
Doctoral School of Sciences and Innovative Technologies
PhD Program in Chemical and Material Sciences XXX Cycle

Synthesis of new nanostructured biomaterials derived from starch

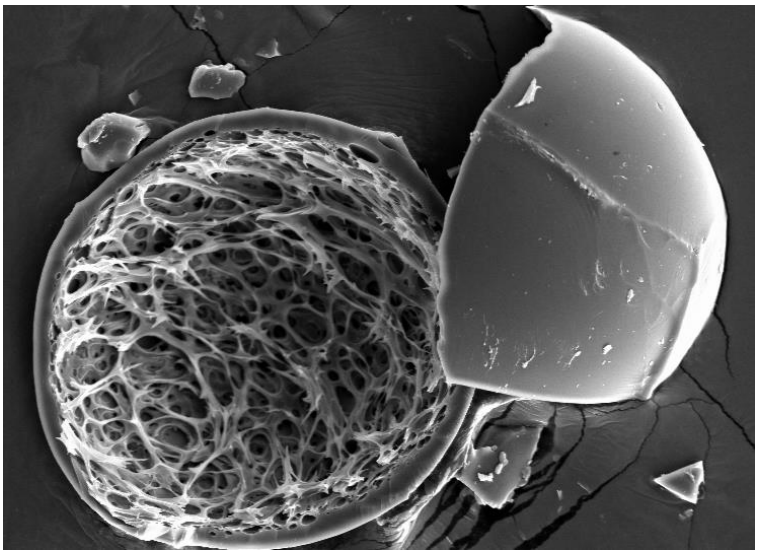

Anastasia Anceschi

Supervisor:
Prof. Francesco Trotta

Università degli Studi di Torino

Doctoral School of Sciences and Innovative Technologies

PhD Programme in Chemical and Material Sciences XXX cycle

Synthesis of new nanostructured biomaterials derived from starch

Candidate: **Anastasia Anceschi**

Supervisor: Prof. **Francesco Trotta**

Jury Members: Prof. **Andrea Mele**
Politecnico di Milano
Dipartimento di Chimica, Materiali e Ingegneria Chimica "Giulio Natta"

Prof. **Renzo Di Felice**
Università di Genova
Dipartimento di Ingegneria Civile, Chimica e Ambientale

Prof. **Marco Zanetti**
University of Torino
Department of Chemistry

Head of the Doctoral School: Prof. Massimo Maffei
PhD Programme Coordinator: Prof. Mario Chiesa

Torino, 2018

Abstract

Porous materials are becoming very interesting industrial materials due to the possibility to tailor their properties based on specific applications. For this reason, many research groups study the novel synthesis or improvement in the performance of different classes of porous materials, such as metal organic framework (MOFs), porous organic polymers (POPs), zeolites, covalent organic framework (COFs) and porous carbons. Among these materials, porous carbon ones have received great attention due to their many applications such as gas separation and purification, catalyst support, fuel cell and supercapacitors. Many precursors can be used for the synthesis of porous carbon materials. Various methods have been applied for obtaining porous carbon materials, such as: chemical and physical activation; pyrolysis of carbonaceous matters; and template synthesis. In this Ph.D. thesis, it is described the production of microporous carbons from hyper cross-linked polymers, also known as nanosponges (NS). For this Ph.D. thesis the Ns were synthetized using as a cross-linking agent the pyromellitic dianhydride.

It is reported a method for preparing porous carbon materials with quite high surface area and a narrow pore size distribution using as carbon precursor the NS from βCD and Lc cross-linked with the pyromellitic dianhydride simply pyrolyzing the samples at 800°C. The carbons obtained from the two NS, labelled C-βNS and C-LcNS, were fully characterized during my Ph.D. using a large variety of techniques. Thermal gravimetric and the ATR analyses were used for investigating the decomposition of the NS. The physical characteristic of the carbons was investigating using a gas-volumetric method using the ASAP 2010. It was found out that after the pyrolysis at 800°C the C-βNS possesses a specific surface of 560 m^2 g^{-1} and pores range size of 5-16 Å, whereas the C-LcNS has a specific surface of 682 m^2 g^{-1} and pores range size of 5-17 Å

The carbons obtained from the pyrolysis of NS were tested in three different applications. Firstly, it was investigated the possibility to use the carbons for the CO_2 carbon capture and storage. Secondly, it was evaluated the possibility to use the carbon from βCD nanosponges for be employed in Li-S batteries.

In the end, the capability of C-βNS to remove emerging pollutants from wastewaters was investigated by testing the adsorption of dyes. In this preliminary study two dyes were investigated, a cationic (methylene blue) and an anionic one (methyl orange). The results suggest that the materials are charge-selective sorbents and can be proposed as sustainable alternative materials for wastewater treatments.

Acknowledgments

I would like to express my sincere gratitude to my advisor Prof. Francesco Trotta for the continuous support of my Ph. D study and related research, for his patience, motivation, and immense knowledge. His guidance helped me in all the time of research and life.

I would also like to thank the committee members that will evaluate my work.

I would like to say a great thank you to prof. Marco Zanetti for the numerous encouragements and opportunities that he has given to me. Sincerely thank you for being a friend and a guide for me.

I would like to express my deeply appreciation to dr. Dominique Scalarone who provide me the opportunity to explore other research field and who gives me the opportunity to live one of the most exciting experience abroad of my life, in terms of research and life-experience.

I thank dr. P. Bracco and dr. V. Brunella for the stimulating discussions and for the funny moments.

A very great thank you to dr. Giuliana Magnacca…I love you!! Thank you for any precious suggestions that you gave me!!!

I would like to thank Claudio Cecone for the many funny moments that we shared, for our insightful discussions and for all the support you gave me. You were always on my side in the difficult and successful moments. It is an immense pleasure working with you and being your friend!

Special thanks to Alberto Rubin Pedrazzo. You are able to make my always smiling. Your infinite support, enthusiasm and the optimistic vision of life were essential for me. Thank you for working with me.

I would like to say a great thank you to Giorgia Musso. Your philosophy of life helps me to hold on when I was getting crazy.

I am very grateful to Fabrizio Caldera, you support me, you make me smile and you were a source of knowledge for me.

Thanks to all the people I had the chance to meet in the lab in the past years. In particular, thank you to Dafne, Chiara, Moira, Maria Pia, Enea, Sushil, Nilesh and Shohreh for every important and funny moments that we had.

A specially thank you goes to Marco Fabbiani. You were my guide in the chemical-physical word and I am very grateful to have the possibility to share with you many important moments of my life.

Chiara Negri, you are one of my best friends and I with you a shared all the most important life moment. I will be never thankful enough to you, who believed and encourage me in each single minute of my life.

A special thank you to Federica Giaccardi. Thank you for loving, supporting, encouraging, entertaining and helping me in the most positive way.

Thanks to my father for your endless support, to my sister Gaia for your understanding and to my brother Massimiliano for your positive sense of life.

Lastly, the greatest thank you goes to my mother, Caterina, for being the first who believed in me as scientist and as a woman. You always supported me, this thesis is dedicated to you.

TABLE OF CONTENTS

1 INTRODUCTION

Porous materials are becoming very interesting industrial materials due to the possibility to tailor their properties based on specific applications.

For this reason, many research groups study the novel synthesis or improvement in the performance of different classes of porous materials, such as metal organic framework (MOFs) [1] , porous organic polymers (POPs) [2], zeolites [3], covalent organic framework (COFs) [4] and porous carbons. Nowadays, the porous carbon materials are performing an increasingly more important role in many industrial fields. In this context many challenges are present [5]:

1. Based on sustainable and renewable materials;
2. Tunable structure suitable of a wide range of applications;
3. Heavy metal free in case of catalysis;
4. Produced via low cost and clean synthesis.

Therefore, regarding these topics, new porous carbon materials using sustainable and renewable precursor have been produced via different synthetic routes. The following are representative traditional methods [6]:

1) Chemical activation, physical activation, and a combination of the physical and chemical activation processes.

2) Catalytic activation of carbon precursors using metal salts or organometallic compounds.

3) Preparation of the carbon precursor with different polymers composite.

4) Carbonization of a polymer aerogel synthesized under supercritical drying conditions.

Porous carbons have been studied and used extensively for several environmental and energy applications such as water purification [7], CO_2 capture [8], electrode materials, batteries [9], electrode materials for microbial fuel cell [10] for waste water treatment [11], and so on. It is important to note that these different applications require carbons with different properties. For example, for removing pollutants form water, micropore dominated

carbons are preferred. Also, in the case of direct CO_2 capture using porous carbons, the presence of micropores plays a very important route. Moreover, the future of portable devices, electric vehicles and smart grids demands long life and high energy density batteries. The serious energy crisis and environmental pollution have brought about an urgent demand for commercial hybrid electric vehicles the electronic market, but their application is still hindered [12]. So, new electrode materials and advanced next-generation lithium battery systems have been continuously explored. Sulfur is a very promising cathode candidate for the next generation batteries. The use of Sulfur presents many drawbacks, but the use of composites with sulfur particles embedded within microporous carbon frameworks has proven promising.

In the way of anthropogenic problems, many green-house gases were emitted in the atmosphere in the last years and the contamination of water by organic molecules is becoming a very important problem[13]. Therefore, there is a need to find effective materials and techniques for removing pollutants from water and from atmosphere. The porous carbon materials seem to be very useful for both these applications. Because their unique structure, porous carbon materials can be used for gas separation. An example can be the separation of the nitrogen from air in which a very narrow pore size is required. Another commercial application in which the porous carbon is very useful is the separation of CO_2. Indeed, it was find out the possibility to use the carbons with the diameter of the pore less than 0,5 nm for separate the CO_2 from a mixture contained the nitrogen using the Pressure Swing Adsorption process (PSA).

Another problem caused by the anthropogenic activities is the contamination of water by the colored organic molecules is calling for the development of effective purification techniques. As a kind of adsorption material, porous carbons can be widely used as industrial adsorbents for this purpose [11]. The use of them for removal of dyes present in aqueous solution is of considerable importance due to their well-developed porous structure. Recent research has placed emphasis on modifying the surface of porous carbon materials for being effective on adsorption of chemical species from aqueous solutions. Carbons can be represented by a model of a twisted network of defective hexagonal carbon layer planes (typically 5 nm wide), which are cross-linked by aliphatic bridging groups. Heteroatoms are incorporated into the network and are also bound to the periphery of the planes. Acidic and basic functional groups present on the

surface can enhance or reduced adsorption capacity and selectivity on a certain adsorbate in the gaseous or liquid phase. For example, it can be postulated that higher adsorption of methylene blue can be related with the presence of negative charged on the surface of the carbons, the adsorption of negative ions. It is possible with various techniques, for example changing the pyrolysis condition, to render the surface more negatively charged, facilitating adsorption of positive charged molecules of methylene blue.

Therefore, regarding these topics, in this Ph. D thesis, new porous carbon materials using sustainable and renewable precursor have been produced via different synthetic routes and tests in some possible industrial application.

1.1 BRIEF HISTORY OF CARBON MATERIALS

Porous carbons, especially activated porous carbons, constitute one of the most important types of industrial carbons and have been in use for thousands of years. Their use in water purification can be dated back to 2000 BC when ancient Egyptians used charcoal to purify water for medicinal purposes [11]. In 1773, Car Wilhem found out the absorptive properties of the carbon-derived materials. In 1911, the first industrial production of activated carbon, called *Eponit*, was done. Currently, different kinds of carbon materials were produced for several industrial applications. In the following paragraphs is presented an overview of the type of carbon materials that can be produced.

1.2 HISTORICAL STUDIES ON POROUS CARBON MATERIALS

The structure of the porous carbon was firstly described by Paul Emmett in 1948 as slit-like voids between the approximated aligned graphene flakes [14]. Another different model was described by Franklin in 1951 dividing the structure in two types of carbon: soft carbon in which the graphitic domains are orientated randomly and hard carbon in which the graphitic domains are orientated more parallel than in soft carbon [15]. A new theory for porous carbon materials was established using the TEM. It was found curved graphene sheets to enclose voids within a ribbon-like structure [16]. This model is controversial and affected by the type of analysis. Indeed, with the discovery of fullerenes and carbon nanotubes, more stable structures were suggested. For example, the analysis of the broad Bragg peaks in XRD proposes a long-range disordered structure, but the inclusion of the diffuse scattering allows the have a weighted histogram of atom-to-atom distance called a Pair Distribution Function (PDF) [17]. The PDF studies show that porous carbon often exhibit a local order and mainly hexagonal carbon rings in which the atoms of carbon are sp^2 hybridized. Moreover, the TEM analysis seems to confirm this concept and shows that the carbon is composed by sheets in a curvature

configuration embed in a disordered matrix [18]. A further contribution to the knowledge of porous carbon material structures is given by the gas adsorption experiments and the Raman spectroscopy. Raman analysis provides a measure of disorder in the carbon bonding network [17]. Incompletely graphitized carbon materials have two characteristic spectral features: the first is a G-mode between 1580 cm^{-1} and 1590 cm^{-1} that indicates the presence of sp^2-hybridized carbon; the second is a D-mode between 1330 cm^{-1} and 1342 cm^{-1} which represents the breathing mode of the 6-fold carbon ring, active when defects, such as edges or vacancies, are present. The gas adsorption analysis is a well-established method for characterized porous solids and it provides information about the pore size distribution and the surface. This technique studies the interaction between the gas and the solid interface. The amount adsorbed on the surface is strictly correlated with the temperature, the pressure and the interaction potential between the gas and the surface. Moreover, the gas-adsorption method is a useful tool for evaluating the ability of a material in gas capture and storage.

1.3 GENERAL ASPECTS OF POROUS CARBON MATERIALS.

Universally, porous materials are considered a specific solid state in which the physical properties are strictly correlated with the assets of the surface and the volume and dimensions of pores [19]. Based on a classical definition, a porous material is described as a solid matrix composed of an interconnected network of pores. The International Union of Pure and Applied Chemistry (IUPAC) divided the porous materials in three categories relating of their pore size regime: micropores, mesopores and macropores. Each of this class presents a different condensation mechanism of gas inside them, as reported in table 1:

Pore type	Pore size range	Condensation mechanism
Micropore	< 20 Å	Three dimensional
Mesopore	≥20≤50 Å	Capillary
Macropore	>50 Å	No condensation

Table 1: IUPAC pore size classification and adsortion mechanism

As will be explained in Chapter 2, gas adsorption is the most used techniques for determining the physical features of a porous materials. Basically, each pore size has an influence on gas-adsorption, leading to manifest different and specific isotherm profile. In micropore, the narrow pore dimension leads to three-dimensional adsorbate condensation. In mesoporous materials, the adsorption proceeds with the formation of consecutive adsorbate layers that finishes with the capillary condensation phenomena. In macropores, the great dimension of the pores inhibits any condensation activity.

The large variety of pore size makes a porous carbon material suitable for a large variety of application. The microporous materials, for instance, have been utilized in liquid- and gas-separation, the mesopores have been applied in catalysis or chromatography application and the macropores have been used for filtering processes. It is possible to obtain a porous

material that has only a type of pore or a coexistence of the three categories. A schematic representation of this is reported in Fig. 1:

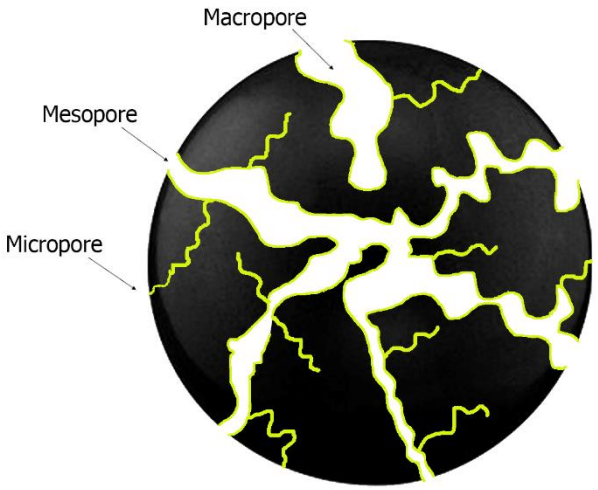

Figure 1: Schematic representation of pores in a porous carbon.

The demand of very efficient porous carbon materials drives to find a new synthetic route for increase the selectivity of these. Therefore, the necessity to produce a material in which it is possible to tune the bulk and the surface properties is becoming increasingly important. For this reason, many type of porous carbon materials has been synthetized with different techniques.

1.4 POROUS CARBON SYNTHESIS AND AN OVERVIEW ON THE STARTING MATERIALS.

The porous carbon materials can be produced from a large scale of carbon-based sources such as woods [20], biomasses [21], coals [22] and polymers [23]. The development in technologies made possible to successfully convert these feedstocks in porous carbon materials essentially through thermal decomposition. Anyway, the preparation of novel carbonaceous materials is a relatively new area and can bring economic and sustainable advantages and applications. In the past, a large part of carbon materials was synthesized from fossil fuel using techniques like chemical vapor deposition and laser ablation [24]. In the past two decades, the process extensively used was the hydrothermal carbonization [25]. Basically, an aqueous solution or dispersion of a saccharide, for instance glucose, starch, etc., is heated at moderate temperature (150-350°C) under pressure. The carbonaceous material obtained is insoluble and it is collected and dried [26]. Another common method used for the preparation of porous carbon materials involves the use of a template. The hard template method includes inorganic colloids or preformed porous inorganic structures, such as silica and zeolite. In the soft template method polymers are widely used [27]. However, in both methods, the template is impregnated with the precursor and then carbonized to generate carbon. Generally, the template is removed using HF etching and the carbon obtained is a negative replica of the original structure. One of the ancient approach to produce porous carbon materials, but actually widely used, is the pyrolysis. It is a thermal process in which solid materials is converted to gas, liquid and new solid formation. It is in general a flexible process regarding the use of feedstocks; indeed, it is possible to use as sources different materials, from wood to wastes. The chemical reaction driving the pyrolysis is endothermic, but the gas produced can be reused to produce energy and so turning the pyrolysis into a self-sustaining process. Anyway, many compounds are obtained from the pyrolysis. A schematic representation is reported in fig. 2:

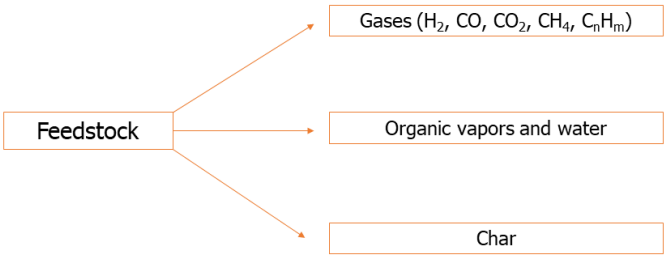

Figure 2: Products from a pyrolysis process

The pyrolysis method and some parameters (particle size, temperature, time of residence) have a great influence on the final product. Thus, the pyrolysis process can be divided in two: fast and slow pyrolysis. The fast pyrolysis, also called flash pyrolysis, is mainly applied to produce liquids, in particular a brown mobile liquid (like fuel oil) and it is a high temperature process in which the feedstock is rapidly heated in an inert atmosphere [28]. Conversely, the slow pyrolysis is the method used when the char is the desired product. The temperature used is between 400°C and 800°C with a heating rate about 10°C min^{-1} [29]. During the pyrolysis, the feedstock undergoes to several physical and chemical modifications and volatilization causes mass loss. In addition, it involves many other changes in porosity, surface properties, area and elemental composition [30]. The phenomena that can be traced during the pyrolysis process depend on the composition of the feedstock and on the reaction conditions. However, many studies were carried out on the pyrolysis of the cellulose, biomasses and carbohydrates [30]. For the cellulose many data were accumulated over the years. It is found that when the pyrolysis of the cellulose is carried out at low temperature, less than 300°C, causes the reduction in the degree of polymerization and the appearance of free radicals, elimination of water, evolution of CO and CO_2 [31]. The high temperature pyrolysis can be expressed by two competitive pathways and a schematic representation of them is reported in fig. 3 [32]:

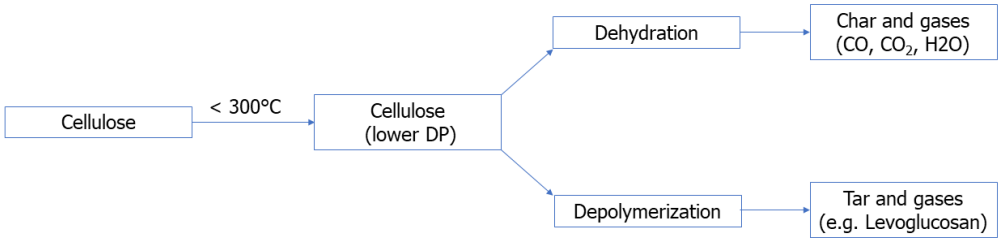

Figure 3: Scheme of cellulose decomposition

As summarized in Fig. 3, if the dehydration of cellulose prevails, evolution of CO, CO_2 and H_2O with formation of solid char take place. If the depolymerization occurs, volatilization of tar, mainly composed by levoglucosan, is observed. The high boiling products present in tar can further decompose leading to the generation of light gases [31]. The composition of the tar is very complicated and difficult to be fully characterized. Anyway, many works [32,33,34,35] propose the formation of products like levoglucosan, 5-hydromethylfurfural, furfural, hydroxylacetone and hydroxylacetaldehyde. The main component of the tar is the levoglucosan, but the yield of this is affected by the source and by the pyrolysis conditions. At higher temperature the levoglucosan is formed by the cleavage of the 1,4-glycosidic linkage in the feedstock and intramolecular rearrangement of the monomer units [34]. Other anhydrous hexoses are formed during the formation of the levoglucosan, such as anhydro-D-mannose and 1,6-anhydro-glucofuranose that are isomers of the levoglucosan. However, during the pyrolysis these anhydrous sugars, especially levoglucosan, can be subjected to a secondary decomposition to CO e CO_2 at 400°C, if it is allowed by the pyrolysis conditions [36]. In conclusion, a slow pyrolysis is the best suitable method for the preparation of porous carbon materials.

1.5 TYPE OF POROUS CARBON

A large variety of porous carbon materials have been reported in literature ranging from activated carbons, templated carbons, carbon nanotubes, carbon nanofibers, carbon aerogels and combinations thereof. In the following paragraphs are reported the most commonly type of porous carbon materials:

1.5.1 **Activated carbon**

Activated carbon is one of the most important adsorbent with a very high ability in removing of organic pollutants and high adsorption capability [37]. After the carbonization of a carbon precursor, the interstices present in the carbon become filled or partially blocked by disorganized amorphous carbon as a result of the decomposition of tarry substances [38]. For remove the tarry products it is possible to use some activation agents performing a physical activation or a chemical activation. The chemical activation is carried out using some activating agents such as H_3PO_4, $ZnCl_2$, H_2SO_4, K_2S, alkali metal hydroxide, carbonates ad chlorides of Ca^{2+}, Mg^{2+} and Fe^{3+}. The physical activation is a process by which the carbonaceous products develops a porous structure and so extended their specific surface area during a heating treatment at temperature between 800-1000°C in presence of oxidizing gases such as steam, CO_2 and air. Usually, the activation with water is faster than the one with the carbon dioxide, because the H_2O is smaller than the CO_2 and so it diffuses faster into the pores. Nevertheless, the CO_2 promotes the external oxidation of the surface leading to the development of larger pore. Basically, the activation burns preferentially the disorganized carbon causing the opening of the blocked pores. Subsequently, the carbon of the aromatic ring system starts burning, producing active sites and wider pores. But, excessive activation reaction produces a knocking down of the pore walls and consequence abundant weight loss. The results of this is a decreasing of the pore volume and there is no a significant increase in adsorption capacity and in specific surface area.

Activated carbons are complex products and so it difficult to classify them. A general classification takes in account the physical characteristic of them and so it possible to have:

- Powdered activated carbon: granules less than 100 mm
- Granulated activated carbon: large size of particles. They usually find application in water treatment, deodorization and separation of components in gas mixture.
- Spherical activated carbon: Small spherical balls with high mechanical strength and they can be used for the adsorption of SO_2 and NO_2.
- Impregnated carbon: The carbon is impregnated with several inorganic impregnant, such as iodine, silver, cations. They are generally applied in air pollution control especially in museum and galleries.
- Polymers coated carbon: The porous carbon is coated with a biocompatible polymer to give a smooth and permeable coat without occluding the pores.

The importance of activated carbon is related with their unique and versatile structure that makes them suitable for a large variety of application. Regarding this topic, the activated carbon finds application mainly in the removal of odor, dyes, taste and other organic pollutants form water. Other applications are in gas separation and purification, pharmaceutical and food fields. An interesting study was carried by Johnson et al. in which they found out that a car cannister with activated carbon was able to adsorb gasoline vapor in the tank of a car during parking and running [39].

1.5.2 **Carbon Aerogels**

The IUPAC defines the aerogels as non-fluid network composed of interconnected colloidal particles as the dispersed phase in a gas, typically air [40]. The aerogels can be constructed of organic, inorganic or metal compounds. From a microscopic point of view, they are made of a network of clustered nanoparticles resulting in unique physical properties. The aerogels present any type of porosity, from micro- to macropores. They are generally produced from organic/polymeric aerogels that are then carbonized for forming carbon aerogels. The synthetized precursor is converted in carbon aerogel via controlled thermal annealing or carbonization under inert gas. The resulting carbons are generally microporous or mesoporous with a well-defined structured and a very high surface area. The precursor generally used for the synthesis of the starting aerogels are derived from condensation of resorcinol/formaldehyde [41], saccharides [42], polysaccharides [43] and doped resorcinol/formaldehyde with flavonoids, tannins and lignin [19]. The synthetic aerogels can be successfully converted in microporous carbon and mesoporous carbons, but the pore dimensions of the precursor are not automatically transferred in the carbon structure. Carbon aerogels are generally light weight, for example, the carbon aerogel shown in the Fig. 4 has a density of 0,16 milligrams per cubic centimeter [44].

figure 4: A 100 cm^3 carbon aerogel cylinder standing on a flower like dog's tail [19].

1.5.3 **Carbon nanotubes (CNTs)**

CNTs can be considered as a classical and demonstrative example of carbon-based nanomaterials [19]. Classically, they are produced from chemical vapor deposition in which a carbon precursor, e.g. methane, xylene acetylene, is decomposed with an appropriate catalyst (metal or metallic nanoparticles) [45]. The researchers focused their attention on the development of a method to convert the carbon precursor in very efficient way. Catalysts play a crucial role in the chemical vapor deposition synthesis of CNTs. The nanotubes are usually synthesized using transition metal nanoparticles as catalysts [46]. The structure of CNTs has been found to be determined by the size and chemical composition of the metal catalysts. However, at present, the diameter, length, and chirality of CNTs have not been controlled sufficiently in a single process due to incomplete understanding of the role of the catalyst in nanotube nucleation and growth. The Transition metals used to date as catalysts include Fe, Ni, Co, and Mo. However, more recent studies have shown that other metals such as In, Cu, Ag, Pd, Mn, Mo, Cr, Al, and Au are effective for the synthesis of the CNTs [47]. Another problem related with the synthesis of the CNTs is the carbon precursor. These carbon precursors widely used come from fossil fuels, such as methane, acetylene, benzene, xylene and toluene and in view of a green future, it is necessary to consider developing carbonaceous materials from the natural resource. Over the past several years, natural renewable resources have been investigated, like camphor, turpentine oil, eucalyptus oil, castor oil, coconut oil, and palm oil for synthesis of CNTs [48,49]. Recently, our research group finds a method for synthetizing the CNTs from plastic waste. For the treatment of the wastes the pyrolysis is carried out between 300°C-800°C to convert the material from the solid state into gaseous compounds and liquid products. An unsupported organometallic catalyst is injected into the flow in order to convert the carbon-contained gas into nanotubes [50].

Carbon nanotubes are classified in following two types: SWCNTs—Single-walled carbon nanotubes and MWCNTs—Multiple-walled carbon nanotubes and a schematic representation is reported in Fig. 5.

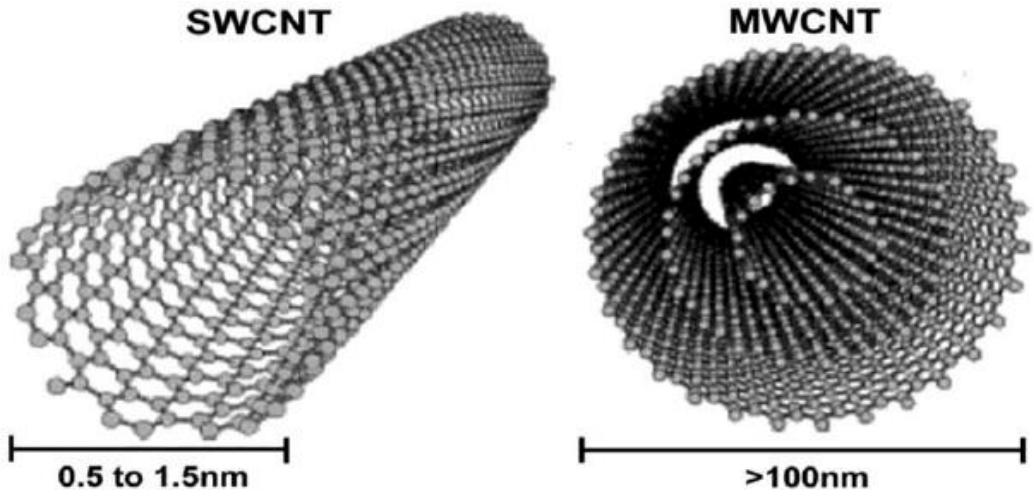

Figure 5: Representation of SWCNTs and MWCNTs [51]

SWCNT can be visualized as rolled-up tubular shell of graphene sheet which is made up of benzene type hexagonal rings of carbon atoms whereas a MWCNT is a stack of graphene sheets rolled up into concentric cylinders. Each nanotube is a single molecule composed of millions of atoms and the length of this molecule can be tens of micrometers long with diameters as small as 0.7 nm [52]. The SWCNTs usually contain only 10 atoms around the circumference and the thickness of the tube is only one-atom thick.

The strength of the carbon-carbon bonds gives carbon nanotubes amazing mechanical properties. The highest measured tensile strength or breaking strain for a carbon nanotube was up to 63 GPa which is around 50 times higher than steel [53]. Moreover, CNTs have high thermal conductivity high electrical conductivity. Various biomolecules (proteins, enzymes, or DNA/RNA) can interact and be immobilized on the CNTs, leading to possible application of them in biomedicine [46].In the end, CNTs have already proven to serve as safer and more effective alternatives to previous drug delivery [54].

1.5.3.1 Fullerene

Fullerene is a third form of carbon along with graphite and diamond that features unique properties that make it ideal for photo-resists, organic photovoltaics, spin-on carbon hard masks and organic photo detectors. Their discovery in 1985 was rewarded with a Nobel prize in chemistry 10-years later. Fullerenes consist of 20 hexagonal and 12 pentagonal rings as the basis of an icosohedral symmetry closed cage structure. Each carbon atom is bonded to three others and is sp^2 hybridised. It is not "superaromatic" compounds as it tends to avoid double bonds in the pentagonal rings, resulting in poor electron delocalization and so it behaves like an electron deficient alkene, and reacts readily with electron rich species. A representation of a fullerene is reported in Fig. 6

Figure 6: Schematic representation of a C_{60} fullerene

Fullerene are proposed for use in optical, electronic, cosmetic, and biomedical applications.

1.5.4 **Carbon Molecular Sieves**

Carbon molecular sieves (CMS) are a special class of activated carbons. Their structure is a twisted network of defective carbon layer planes, cross-linked by aliphatic bridging groups [55]. CMS are mainly non-graphitic, amorphous and the randomly cross-linked network inhibits reordering of the structure. The surface area, dimensions, and distribution of the pores depend on the precursor and on the conditions of the carbonization and of the possible activation. The distinction between the CMS and the activated carbon is not clearly defined. The main distinction can be that activated carbons separate molecules through differences in their adsorption equilibrium constants whereas the CMS provide molecular separations based on rate of adsorption rather than on the differences in adsorption capacity. The fundamental building blocks of CMS are aromatic microdomains and so-called amorphous carbon [56]. The pyrolysis of the precursor forms void spaces in the carbon matrix and they are generated by the misalignment of the aromatic microdomains. These misalignments provide the porosity the system and so the pore size is a crude measure of the averaged displacements between these microdomains. A schematic representation is reported in Fig. 7:

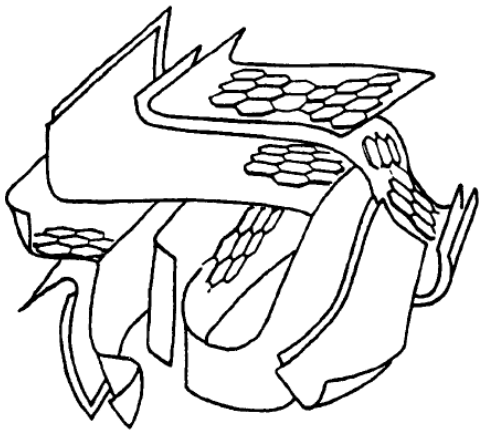

Figure 7: Schematic of folded graphite-like layers [57].

The so-formed amorphous carbon is ill-defined and it has been described as sp^2 hybridized in two-dimensional graphite-like layers with hexagonal rings bent out of the plane and possibly stabilized by heteroatoms. Anyway, the chaotic structure of the CMS material is strongly influenced

by the thermal history of the sample, its post-pyrolysis treatments and its precursor.

Despite the amorphous nature of CMS, they show remarkable properties and these are the following:

- Stability at high temperature;
- They are stable in acid media;
- They have low affinity to water;
- They are easy to make;
- The pore sizes can be controlled by the method of preparation.

The preparation of these materials involves many starting materials such as coal, wood and polymers. For reasons of economy, the most favored starting material for making carbon molecular sieves is coal that itself has some sieving properties [55]. Many methods can be applied for transform the coal into a CMS. The first approach consists in a gas activation, called Fluidized, in which coal is heated in nitrogen up to 800-900°C, then cooled to 400°C and expose to air. After that, the sample is reheated in nitrogen to 900°C. A second method that can be applied is a chemical activation, mixing the coal with $ZnCl_2/H_3PO_4$ and heat to 900°C under inert atmosphere. Another approach is a gas activation plus hydrocarbon cracking. In this case, the coal is heated and treated like in the first method, but it is involved the cracking of the propylene at 400°C-500°C. The last technique is a melt spinning. The melt spinning process consists of first dissolving coal in a solvent, such as coal oil. The solvent is, then, evaporated from the material and a melt is left with a melting point of around 200°C. It is heated up and can be spun out into fibers. These fibers can then be treated either to produce graphitic carbon fibers by heating at high temperatures or by activating with air to produce porous carbons or carbon molecular sieves.

Carbon molecular sieves can also be made from various polymers such as polyvinylidene chloride, polyacrylonitrile, phenol formaldehyde, etc. Pioneer workers in producing carbon molecular sieves from polymers [55] had originally hoped to make carbons of similar structure to the original polymer framework. Unfortunately, during the heat treatment, the polymer structure collapsed.

In the way to use low cost materials, biomasses are becoming attractive materials as a precursor for preparation of CMS. Biomass is a renewable source of carbon which can be converted to solid, liquid and gaseous product through various conversion processes [58]. During thermal treatment, moisture and volatile compounds are removed from the biomass and solid chars are generated whose properties are different from the origin of the biomass materials. The carbon materials obtained could have a high porosity, large surface area and high pore volumes. Therefore, the generated char can be attractive for the preparation of CMS. Basically, preparation of the CMS from lignocellulosic material involves carbonization of the lignocellulosic biomass and a further activation.

1.5.4.1 Recent perspetives in the uses of polysaccharides as carbon precursor

Recently, researchers focused their attention on the transformation of polysaccharides into porous carbon materials. Many types of polysaccharides can be used as carbon source, actually starch. Starch is a polymeric carbohydrate consisting of anhydroglucose units linked together primarily through α-(1,4) glucosidic bonds. It contains two microstructures. The first is amylose, a linear structure of α-1,4 linked glucose units. The second is the amylopectin, a high branched structure composed by of short α-1,4 chains linked and by α-1,6 bonds [59]. The ratio of amylose/amylopectin depends on the source and age of the starch. Wang et al. [60] prepared carbon spheres using porous starch as a precursor. However, the procedure was rather complex. In details, the porous starch was prepared mixing the corn-starch in an acetic acid–sodium acetate solution and, then, an enzyme mixture was added in order to create a porous structure. After that, the porous starch was mixed with various inorganic coating and heated up to 600° C in a tubular furnace. After the carbonization, the coating agent has been removed with aqueous HF leaving mesoporous carbon spheres. Pang et al. reported the fabrication of porous carbon with a high specific surface area of 1239 m^2 g^{-1} and a large pore volume of 1,40 cm^3 g^{-1} from corn starch by a two steps process: hydrothermal carbonization followed by a chemical activation with H_3PO_4 [61]. A simpler methodology to prepare porous carbon

from starch without any templating agent has been proposed by Budarin et al. [62]. They obtained mesoporous carbon with a pore size of 7 nm pyrolyzing under nitrogen flow a porous starch patented with the name of Starbone®. However, the total porosity of this carbon is not well known since the pore diameter was assessed by TEM while the specific surface area was not measured.

Other saccharides that have attracted attention for the synthesis of porous carbon with sieving properties are the cyclodextrins and the cyclodextrins compound. For example, Wang et al. [60] used hydroxypropyl-β-cyclodextrin to synthesize a mesoporous material, by preparing a composite with silica. Specifically, hydroxypropyl-β-cyclodextrin is dissolved in water and then added with tetrahydroxysilane (TEOS). The mass is then left for three days with continuous removal of ethanol and then heated at 100° C for 12 h. The final solid is then filtered and dried at 40° C. The material so obtained consisting of HPCD/silica is then carbonized at 900° C in nitrogen. After the carbonization the material is treated with hydrofluoric acid in order to remove silica. Following to the thermal initial treatment, BET specific surface areas between 500 and 1200 m^2g^{-1} were obtained. The volume of the pores of the obtained material was between 0,11 and 1,22 cm^3g^{-1}, the total volume of the micropores was between 0,022 and 0,239 cm^3g^{-1}. The study about the carbonization pathway of β-cyclodextrin and β-cyclodextrins-derivatives, finding them capable to produce under pyrolysis condition valuable amounts of carbon [63]. More recently, cyclodextrins have been taken as pyrogens and carbon precursors to yield nanoporous carbon materials. Many researchers [64,65] synthesized mesoporous carbons by a templating method using silica from tetramethyl orthosilicate as template to produce bimodal mesoporous carbons.

In this doctorate work of thesis, The CMS were prepared using as a precursor two types of hyper-cross-linked polymers, also known as nanosponge,s using the β-cyclodextrins and a starch-derivative, named Linecaps ® . Basically, it has been discovered that it is possible to produce microporous carbon materials with sieving properties simply pyrolyzed the nanosponges. A wide presentation about these starting materials and the method use for producing porous carbon materials is reported in Chapter 2.

1.6 SOME APPLICATIONS OF POROUS CARBON MATERIALS

Porous carbon materials find application in many industrial fields like shown in Fig. 8 and in the following paragraph are reported all the areas investigated.

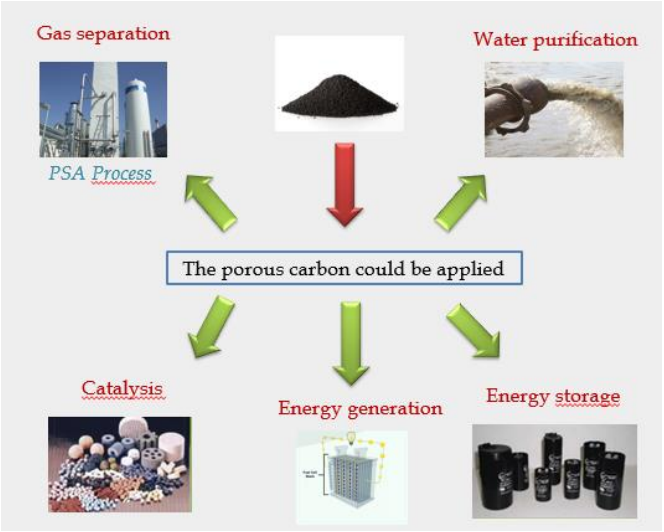

Figure 8: Some applications of porous carbon materials.

1.6.1 **Catalysis**

For their shape-selective properties, the porous carbon materials have been used as a catalyst support and possibly as catalyst in their own right. For example, it is possible to incorporate some metal particles or metal oxide [56] and so render them catalyst for many applications. Porous carbon materials that contain Pt can be used for the dehydrogenation chemistry. The combination with the pore structure and the presence of active metal provides the molecular discrimination of the reactants and so a selective hydrogenation/dehydrogenation material.

The presence of iron in the structure of the porous carbon materials seems to make them suitable for the Fisher-Tropsch reaction [66]. The use of them in the reactor under mild conditions has shown a very interesting selectivity data indicating that this type of catalyst produces mostly methane and a lower amount of higher hydrocarbons. Moreover, the conversion of CO is comparable with the one obtained using traditional catalyst.

Recently, the CMS found application in the synthesis of methylamines from methanol and ammonia [67].

Remarkably, the porous carbon materials have also been used as a catalyst for the deep oxidation. Brendley et al. [68] found a material, called Ambersorb, that are very effective for the decomposition of halogenated hydrocarbons by air a relatively low temperature (less than 250°C). This material is formed by micro-, meso- and macropores that rend it suitable for being active as a catalyst without the incorporation of any type of metals or metal oxides.

The versatility of the design and of the pore structure provides to the porous carbon materials technological properties and so to be a very useful resources for the catalysis.

1.6.2 **Gas separation and purification**

The primary use of porous carbon materials is for the separation and purification of gases. For example, separation of hydrogen from product gases used for refinery applications [69], separation of methane from CO_2 [70], separation of light hydrocarbon gases [71], separation of olefins from isoprene and butadiene [72]. Numerous patents have also been obtained for the purification of gas streams when certain pollutants are present in small quantities. These include the separation of carbon disulfide from pentane, the removal of mercury from stack gases, and finally, the removal of SO_X from off gases in sulfuric acid plants [73]. However, the standard process used in gas separation is Pressure Swing Adsorption, PSA. Fig. 9 shows a schematic representation of a Pressure Swing Adsorber for the separation of nitrogen from oxygen. In this typical example a reactor A is filled with 4 bar of air and after 60 seconds the pressure is released. The product obtained is 99.9% pure nitrogen. The reactor is then evacuated in order to eliminate all the other components of air. While the reactor A is outgassed the reactor B is compressed with air. In this way, continual operation is maintained during the cycling operation, of the two parallel units.

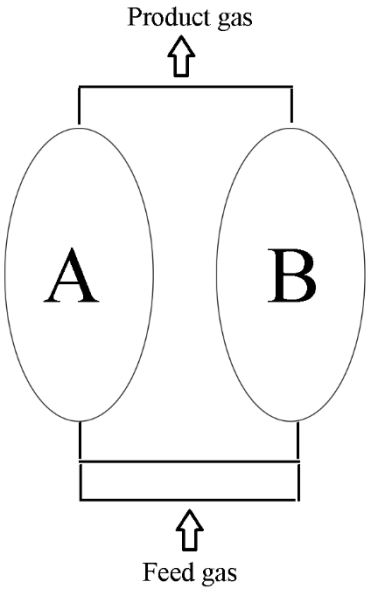

Figure 9: Scheme of a typical PSA adsorption unit (A and B are adsorbent reactors)

Recently, a PSA cycle for CO_2 separation from a low-CO_2-concentration flue gas containing CO_2 has been studied using carbons as the adsorbents [74]. The Global warming and the Green-house effects leads to find some efficient method for capturing and storing the CO_2. The existing industrial CO_2 capture systems are based on chemical absorption using a large range of liquids, in particular aqueous amine solutions, such as monoethanolamine and (2-aminoethyl)ethanolamine and this technology is commercialized over 60 years [75]. The CO_2 recovery rate is 98% using the monoethanolamine. In the process used for removing the CO_2, the monoethanolamine is put in contact with flue gas stream and it reacts with CO_2 in the gas stream to form monoethanolamine carbamate. The solution obtained is then sent to a stripper and heated in order to release the almost pure CO_2 and the monoethanolamine is then recycled to the absorber. This process is expensive and required an intensive energy input even using mix of amines. For avoiding the drawbacks of the use of the amines, Yeh et al. [76] reported the capture of the carbon dioxide with ammonia solution. In this case, the flue gas needs to be pretreated in

order to eliminate SO_2 and NO. Afterwards, the purified gas is put in contact with the aqueous ammonia solution in a wet scrubber. The regeneration requires again a heating treatment. They estimated that this process saves energy up to 60% comparted with the use of the amine. Another proposed approach consists in the use of Solvay dual-alkali method [77]. It employs the ammonia as a catalyst for the reaction of the CO_2 with NaCl to produce sodium carbonate and then sodium bicarbonate. The ammonia is recovered using lime in form of limestone. This process shows many drawbacks: the use of limestone renders the process ineffective, requires a high use of energy and, obviously, the decomposition of the $CaCO_3$ produces CO_2. Another method involves the use of membranes. They are widely used in many industrial applications. The driving force for the membranes in gas separation is the pressure. Indeed, they required high pressure to be very effective, but the low pressure of CO_2 in the flue gas makes the membranes unsuitable for many industrial applications. Many types of membranes have been applied: polymeric membranes, inorganic membranes, carbon membranes, alumina membranes, silica membranes, zeolite membranes and hybrid membranes. Anyway, membrane separation processes provide several advantages, but need to combine high flux, high selectivity and high stability not actual practicable.

As reported previously one of the most promising method for recovering the carbon dioxide is the PSA process. Historically, the recovery of CO_2 using pressure swing adsorption systems has been applied in some industrials fields such as natural gas processing and hydrogen production. In these industries, the feed gas is available at a high pressure and low temperature, and thus, CO_2 can be recovered by using a readily available driving force such as the pressure difference between the high feed pressure for adsorption and a lower pressure for desorption. The driving force is generally referred to as the pressure ratio in terms of difference between desorption pressure to the adsorption pressure. Many adsorbents commonly used in PSA processes have a very strong affinity for CO_2. The PSA shows many advantages: it is simple to operate and it requires regenerative adsorbents. The increase in interest in Carbon Capture and Storage (CCS) technologies has resulted in many researchers investigating CO_2 recovery from flue gases using PSA systems. Carbon capture and storage is considered one of the powerful method for reduce the emission

of carbon dioxide in the atmosphere from industry activities. CCS works in three different ways: pre-combustion, oxyfuel combustion and post-combustion. In pre-combustion capture process, the first step is the production of a mixture of hydrogen and carbon monoxide (syngas) from a primary fuel. The syngas can be obtained adding steam or oxygen to the fuel. In the first case, the process in called "steam reforming"; in the latter case "partial oxidation". The oxy-fuel CCS eliminates N_2 from the fuel gas by the combustion of hydrocarbons or carbonaceous fuel in pure oxygen [78]. The temperature required for the combustion of fuel in a pure oxygen atmosphere is 3500°C. Obviously, no typical combustion plant can reach this temperature and, so it is limited to 1300°C-1400°C in a gas turbine cycle and 1900°C in a oxy-fuel coal-fired boiler. The combustion products consist of carbon dioxide and water vapor. The water is then condensed for being separated from the carbon dioxide. The CO_2 is compressed, purified and delivered into a pipeline for being storage. The post combustion process consists in catching the CO_2 after the combustion of the fuel. In a typical procedure, the gas-mixture passes at atmosphere pressure and at temperature of 40°C-60°C in a unit in which the CO_2 is captured through chemical or physical interaction. The importance to have a material that is selective for the CO_2 at high temperature and different pressures becomes evident. Anyway, the interest in CCS favorites the studies about the possibility to use the PSA process for separate the CO_2 in a gas mixture. These studies using vacuum desorption conditions show that high and/or moderate rates of CO_2 recovery and purity can be achieved without the need of excessive compression of the feed gas stream by utilizing vacuum desorption conditions.

For all these reasons, one of the aim of my Ph.D. work was to use the nanosponge-derived carbons as adsorbent materials for the PSA process, investigating the possibility to selectively adsorbed the CO_2 even at high temperature.

1.6.3 **Li-S batteries**

For their high surface area, carbons are also finding application in other fields such as electrical storage and specifically, the electrical capacitor field. The future of portable devices, electric vehicles and smart grids demand long life and high energy density batteries. State-of-the-art Li-ion batteries are limited in specific capacity and energy density (~300 W h kg^{-1}), and being a mature technology, it is not to be expected any marked improvement in the performance [79]. Li/S batteries offer high theoretical capacity (1675 A h kg^{-1}) [80] and they can be applied for this purpose. The development of Li/S system faces several challenges such as low degree of Sulphur utilization, gradual capacity fading, poor rate capability and low Coulombic efficiency. These drawbacks are mainly due to low conductivity of S_8, used as a cathode, and the ability of it to generate polysulphides that inhibits the restore of the cathode. Lithium polysulphides (PS) (Li_2Sn, n = 4–8) are soluble in the liquid electrolyte and cause the shuttle phenomenon. Therefore, new approaches for the design of the cathode must be considered. Many carbonaceous structures appear to be appropriate for hosting the Sulphur, such as micro, meso and microporous carbons, carbon nanotubes, carbon fibers and graphene [81]. In recently studies, microporous carbon matrices were investigated because they can entrap short-chain Sulphur species (predominately S_2) and metastable sulfur allotropes S2–4 via confining them into micropores [9]. Ryu et al. [82] had shown that it is possible to achieve high capacity Suphur cathode using solution impregnation only. Others reported ball mixing, melt infusion and vapour-phase diffusion to achieve homogenous impregnation of Sulphur into the pores [83].

In this Ph.D. thesis, in collaboration with the Politecnico of Torino, microporous carbons with a narrow range of pore size distribution are synthesized by carbonizing β-cyclodextrin nanosponges. Sulphur is incorporated via solvent impregnation and thermal infusion inside the carbons and used as a cathode for Li-S batteries for automotive applications.

1.6.4 **Removal of organic pollutants form water solution**

The water contamination by organic molecules is a demanding problem that request the development of effective purification techniques [13]. Textile, paper print leather, food and plastic industries are the major contributors of colored effluents [84]. It is estimated that over $7x10^5$ tons of dye-stuff are annually produced and the real problem is the discharging of the effluent by the industries. Indeed, the presence of colored compounds in water is visible even at low concentration and so undesirable [85]. Furthermore, dyes in water resources can affect the aquatic life and cause allergic dermatitis, skin irritation, cancerogenic and mutagenic diseases for aquatic organisms and humans [86,87]. One of the most commonly used dyes in textile industries is methylene blue (MB), but it causes several effects from headache to red blood cell breakdown [88]. Therefore, an adequate treatment of the colored wastewater before the discharging is necessary.

Many difficulties have been found during the removal of dyes [89]. Indeed, they are stable to biodegradation [90] and photodegradation [88], designed to be soap and oxidizing agent resistant [91] and some of their degradation compounds are toxic. For these reasons, many methods and technologies were applied to abate the content of organic dyes in wastewater such as coagulation and flocculation [92], reverse osmosis [93], chemical oxidation [94], ozone [95] and bacterial action [96]. Therefore, the aim of this ph.D work is the preparation, the physicochemical characterization and the performance comparison of β-cyclodextrins nanosponge-derived porous carbon sphere obtained via pyrolysis at mild conditions (pyrolysis temperatures set in the 300-500°C range). The obtained carbonaceous materials were tested as adsorbent for the removal of dyes from aqueous environment. Dyes selected were the cationic methylene blue and the anionic methyl orange.

2 MATERIALS AND METHODS

2.1 CHEMICALS

Dimethylsulfoxide, acetone, triethylamine, pyromellitic dianhydride, 1,4-diazabicyclo[2.2.2]octane, Sulphur, 1,2-dimethoxyethane (DME) and 1,3-dioxolane (DIOX), lithium trifluoromethanesulfonate ($LiCF_3SO_3$, LiTFSI), LiNO3, Methylene Blue and Methyl Orange were purchased from Sigma-Aldrich and used as received. The graphene oxide was bought from Graphenea.

All other chemicals, used and not listed above, were commercially available analytical grade products.

β-cyclodextrin (β-CD) was kindly gifted by Roquette Frères Spa (Lestrem, France).

Linecaps® (Lc) was kindly supplied by Roquette Italia (Cassano Spinola, Italy).

Both β-CD and LC were desiccated, before use, in oven at 80°C for at least one night, in order to remove the absorbed moisture.

Deionized and milliQ® water were obtained using a Millipore Direct-QTM[5] production system.

2.2 MATERIALS

In the following paragraph is reported an overview of the materials used and the synthesis.

2.2.1 **Cyclodextrins**

Cyclodextrins are cyclic oligosaccharides composed by six, seven or eight glucopyranose units linked by α-(1-4) bonds to form the main representative family of α, β and γ-cyclodextrins. They are also known as cycloamyloses, cyclomatoses and Schardinger dextrins [97]. They are produced by the enzymatic degradation of the starch by cyclodextrins glucanotransferase (CGTase) [98] enzyme and they are the result of intramolecular transglycosylation reaction. The properties of the cyclodextrins are reported in table 2:

Properties	α-cyclodextrin	β-cyclodextrin	γ-cyclodextrin
Number of glucopyranose units	6	7	8
Molecular weight (g/mol)	972	1135	1297
Water solubility (% w/v) 25°C	14.5	18.5	23.5
Cavity diameters (Å)	4.7-5.3	6.0-6.5	7.5-8.3

Table 2: Physical properties of the cyclodextrins

Apart from these natural cyclodextrins, many derivatives can be synthetized and usually they are produced by aminations, esterifications and etherifications of primary and secondary hydroxyl groups of the cyclodextrins. The presence of the substituents modifies the physical properties of the native cyclodextrins in term of dimension of the cavity, solubility, chemical activity and stability [99].

Cyclodextrins are famous for the formation of inclusion complexes with a very wide range of solid, liquid and gaseous compounds by molecular

complexation [100]. The lipophilic cavity of cyclodextrin molecules provides a microenvironment into which appropriately sized non-polar substrates can enter to form inclusion complexes [101]. Moreover, the formation of multiple complexes may be observed: according to the geometrical structure of these molecules, two or more cyclodextrins might be involved, leading to a stoichiometry or more ratio cyclodextrins: guest molecules.

In the end, cyclodextrins are generally used as a building block for the construction of supramolecular structures [102]. The most common used type of cyclodextrins are the β-cyclodextrins (βCD) because they are the most accessible and lowest-priced.

2.2.2 **Linecaps**

Similarly to the cyclodextrins, the Kleptose Linecaps® is a starch derivatives and it is a polymeric carbohydrate consisting in anhydroglucose units linked together primarily through α-(1-4)-glucosidic bonds. It contains two microstructures. The first is amylose, a linear structure of α-1,4 linked glucose units. The second is the amylopectin, a high branched structure composed of short α-1,4 chains linked by α-1,6 bonds [103]. Fig. 10 shows schematic representation of the starch:

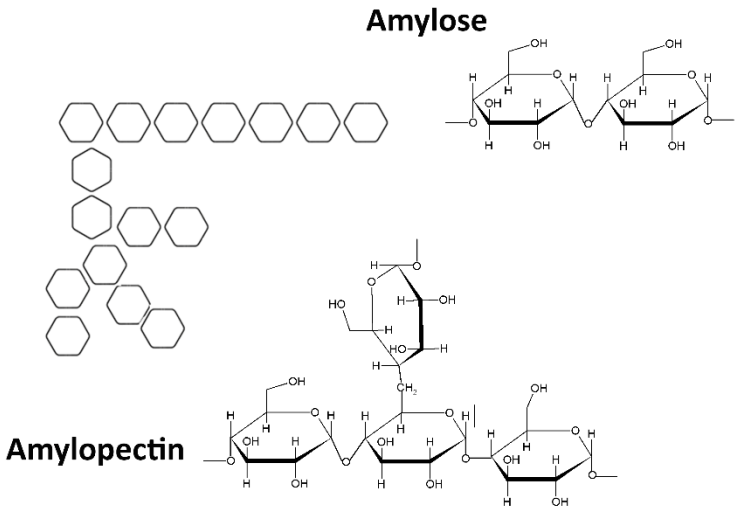

Figure 10: Schematic representation of the components of the starch

Basically, amylose is a linear structure whereas amylopectin is a highly branched structure of short chains. Amylose and amylopectin are packed in granules which are in part crystalline and in part amorphous [104]. The content in amylose and amylopectin in starch depends on the source and it has a great influence on the properties of the starch, such as swelling and gelatinization ability. As the cyclodextrins, the starch has inclusion-complex properties.

Among the variety of starch commercially available, the Linecaps (Lc) is one of the most interesting products. The Lc is a soluble high amylose starch obtained by the partial hydrolysis of pea starch and its molecular weight is about 12 KDa. It is composed by 40% of amylose and the remaing 60% is glucose, oligosaccharides and polysaccharides as amylopectin. The Lc has a helical design with an outer hydrophilic surface whereas the inner surface is hydrophobic.

Both βCD and Lc used for this thesis were kindly gifted by Roquette Freres.

2.2.3 **Nanosponges**

The term *nanosponge* (NS) denotes a class of polymers insoluble with a nanometric and subnanometric porosity [105]. NS can be synthesized using either organic or inorganic compounds. Some examples are metal oxide-based NS [106], silicon nanosponge particles [107], carbon coated metallic Ns [108], hyper cross-linked polystyrene NS [109] and, of course, cyclodextrins based NS. The common characteristic of these materials is the presence of nanoscale pores which gives them peculiar properties.

The well-known cross-linking agent is the epichloridrine [108]. The epichlororidrine based Ns have been used for several purposes from columns for inclusion chromatography to cobalt and copper elimination in food [110]. Glutaraldehyde [111] is also reported to give a cross-linked cyclodextrins for molecular recognition purposes. More recently, the NS are obtained using different kind of cross-linking agents, such as diisocyanates, diarylcarbonates and carbonyl diimidazole , carboxylic acids and dianhydrides and 2,2-bis(acryloamino)acetic acids [108].

Thanks to the great amount of reactive hydroxyl groups, starch derivatives, like cyclodextrins and Linecaps, can act as polyfunctional monomers and be cross-linked using a wide variety of chemicals. Thus, βCD and Lc can be the suitable building blocks for the synthesis of the NS. The commonly method for the synthesis of the NS consists in dissolving the βCD or the Lc in an appropriate solvent, usually an aprotic organic solvent. After that, it is possible to add a catalyst, if required by the reaction, and to introduce the cross-linker under continuous stirring or sonication.

The NS can be grouped in four generations. The simple reaction between the cross-linker and the polysaccharide can be ascribed to the first generation. The second generation is formed by the functionalized NS and they are characterized by peculiar properties such as charge and fluorescence. In the third generation, the stimuli-responsive NS are present. This kind of Ns can modify their behavior according to the external environment. Variations, like pH and temperature have an important influence on the release of drugs loaded in them. Finally, the fourth generation of NS are represented by Molecular Imprinted Polymer (MIP) that exhibits a high selectivity towards specific molecules [105].

Therefore, during years, the architecture of these kind of polymers was subjected to changes in order to be used for different purposes.

In this thesis, the first generation of NS has been applied. This group can be divided in four further classes depending on the nature of the functional group of the cross-linker in urethane, carbonate, ester and ether NS. The urethane NS are obtained cross-linking the polysaccharides with diisocyanates, such as toluene-2,4-diisocyanete and hexamethylene diisocyanate [112]. These NS are characterized by a rigid structure and high chemical degradation resistance without any swelling properties. The carbonate NS are made using carbonyl compounds, for instance 1,1′-carbonyldiimidazole [108]. They found application in pharmacological field [113]. The ether NS are synthetized by reacting the polysaccharides with cross-linking having epoxide groups, like epichlororidrine[114]. This kind of Ns exhibits a high chemical resistance and a tunable swelling capability. They find many applications, for example in pharmacological fields as anti-inflammatory and anti-fungal [114]. The last type of first generation NS is characterized by ester bonds. Generally, they are synthesized using as a cross-linking agent dianhydrides or di/polycarboxylic acids, like ethylendiamine-tetraacetic dianhydride, butanetetracarboxylic dianhydride, citric acid and pyromellitic dianhydride [105]. These NS have a remarkable swelling ability and they are able to form hydrogels. The swelling property is correlated with the degree of cross-linking and, concerning the chemical stability, ester NS tend to undergo hydrolysis in water solution [108]. Recently, a new application for ester NS has been found: they can be used as a precursor for the production of porous carbon materials [115].

2.2.3.1 Synthesis of β-cyclodextrins based Ns as precursor for porous carbon materials

The βCD based NS (βNS) were synthetized using as a cross-linking agent the pyromellitic dianhydride (PMDA), as a catalyst the triethylamine (TEA) and dimethylsulfoxide (DMSO) as a solvent. The NS used as a precursor for the production of porous carbon materials was prepared in 1:4 molar ratio of βCD and PMDA. In a typical procedure 11,35 g of anhydrous βCD were dissolved in 100 ml of DMSO. After the complete dissolution of the βCD, 2,7 ml of TEA was added as catalyst. Few minutes later, 17,45 g of PMDA were mixed and allowed to react at room temperature overnight. Once the reaction was concluded, the block polymer was grounded in a mortar and then washed in a Buchner funnel with water and acetone. For further purification a Soxhlet extractor with acetone was used for 48 h. A schematic representation of the reaction is reported in Fig. 11:

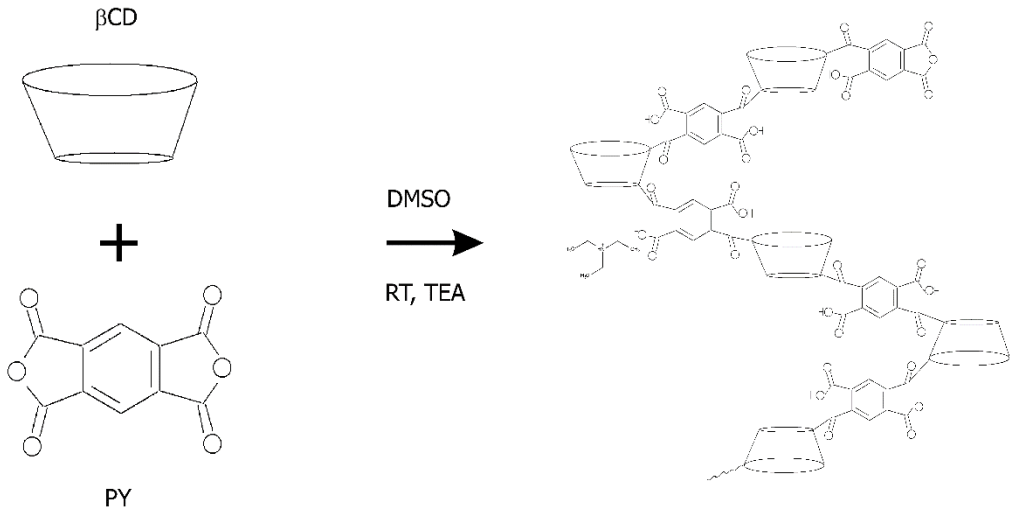

Figure 11: Synthesis of βNS

For better characterized the porous carbon materials obtained after the pyrolysis of the βNS different quantities of catalysts were used. Table 3 reports the amounts of TEA:

Molar ratio βCD-triethylamine	Yield	Time
1-8	98%	few seconds
1-4	98%	few seconds
1-2	85%	30 minutes
1-0,8	60%	2 days
1-0,08	20%	1 week

Table 3: Molar ratio of TEA, the yield and the time required for the synthesis

2.2.3.2 Synthesis of Linecaps based Ns as precursor for porous carbon materials

The Linecaps (Lc) can be cross-linked with the PMDA as the βNS in order to obtain a Linecaps based NS (LcNS). In a typical procedure, 4,89 g of Lc was solubilized in 20 ml of DMSO in a bottom-rounded flask. 5 ml of TEA was added and then the 3,76 g of PMDA. The molar ratio between the Lc and the PMDA is 1:057 expressed as molar ratio of one mole of glucose of the maltodextrin with respect to 0,57 moles of PMDA. After few minutes the cross-linking reaction occurred, and the NS is left to react overnight in order to be considered competed. The LcNS is grounded in a mortar and purified in a Soxhlet extractor with acetone for 48 h. Fig. 12 represents the reaction for the synthesis of the NS:

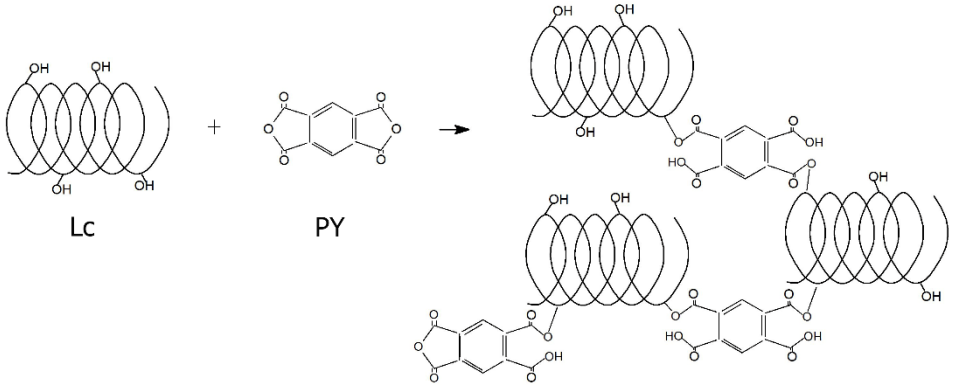

Figure 12: Synthesis of LcNS

2.2.4 **Carbon preparation**

In a typical procedure 2 g of βNS or LcNS were put in a Coors combustion boat and the insert inside a Lenton tubular furnace. The samples were heated to 800°C using 10°C min^{-1} as heating rate under 100 ml min^{-1} of nitrogen flux. For better characterized the samples, different heating ramps were used (20°C min^{-1} and 30°C min^{-1}) and also the final temperature were changed (300°C and 500°C). The furnace was left to cool under nitrogen flux until the ambient temperature was reached. The residue collected after the pyrolysis is labeled C-βNS and C-LcNS, respectively.

For better understand the processes of carbonization and to evaluate the role of the cross-linking in the production of porous carbon materials, also the native Lc and βCD were subjected to a pyrolysis with the same procedure has been just described.

2.2.5 **Preparation of C/S composites for Li-S batteries**

1,5 g of Sulphur was dissolved in DMSO at 90 °C. 1 g of C-βNS was added in the solution. The mixture was heated for 6 h under magnetic stirring to impregnate the C-βNS. The mixture was cooled down to room temperature to crystallize the sulphur in the structure of carbon. The solution-impregnated was collected by centrifugation and washed with ethanol in order to have a carbon Sulphur-impregnated, called C-βNS_SI, Then, a part of it was subjected to a heating treatment to 115°C for 6 h. The temperature is then raised to 155 °C for 12 h. The residue, named C-βNS_MI is then grinded using a mortar.

2.2.6 **Wrapping of C/S composite into rGO for Li-S batteries**

0,14 g of graphene oxide was reduced at 700 °C for 2 h under 3% H_2/Ar atmosphere. The resultant 0,06 g of rGO was well dispersed in 100 mL ethanol using sonication. 1 g of C-βNS_MI was dispersed in rGO ethanol solution under magnetic stirring for 5 h. The ethanol is evaporated at 80°C in an oven and then under vacuum at 60 °C for 8 h. The residue is called C-βNS_MI_rGO.

2.3 METHODS

The instrument and the techniques applied for the characterization of the NS and of the carbon are reported in the following paragraphs.

2.3.1 **Determination of the specific surface area and porosity.**

The carbons were characterized by nitrogen adsorption–desorption isotherms at 77K obtained with an automatic adsorption instrument (ASAP 2010, Micromeritics). This instrument uses two independent vacuum systems one for the samples preparation and another for the samples analysis. Consequently, this instrument measures the pressure and then computes volume adsorbed as a result of change in pressure. It is a very sensitive tool, but for the higher accuracy possible, right amount of sample and the best method for the analysis should be found and used. All the carbon investigated in this Ph. D thesis were prepared outgassing at 300°C for 12 h. Then the samples are left free to cool and then moved in the port analysis. Therefore, the samples are cooled at 77 K, temperature of liquid nitrogen, and exposed at a series of precisely controlled doses of gas (from 0 to 1 of p/p°). Each pressure is recorded, and the universal gas law is applied for evaluate the amount of adsorbed gas. When the bulk condensation is reached, the desorption process begins. These two sets of data describe the adsorption and desorption isotherms. The shape of the isotherms yields information about the type of solid in terms of available surface and so of the porosity (quantity and kind of pores) of the analyzed samples. In 1985, IUPAC published a classification of six sorption isotherms [116]. The appropriate IUPAC classification is reported in Fig. 13:

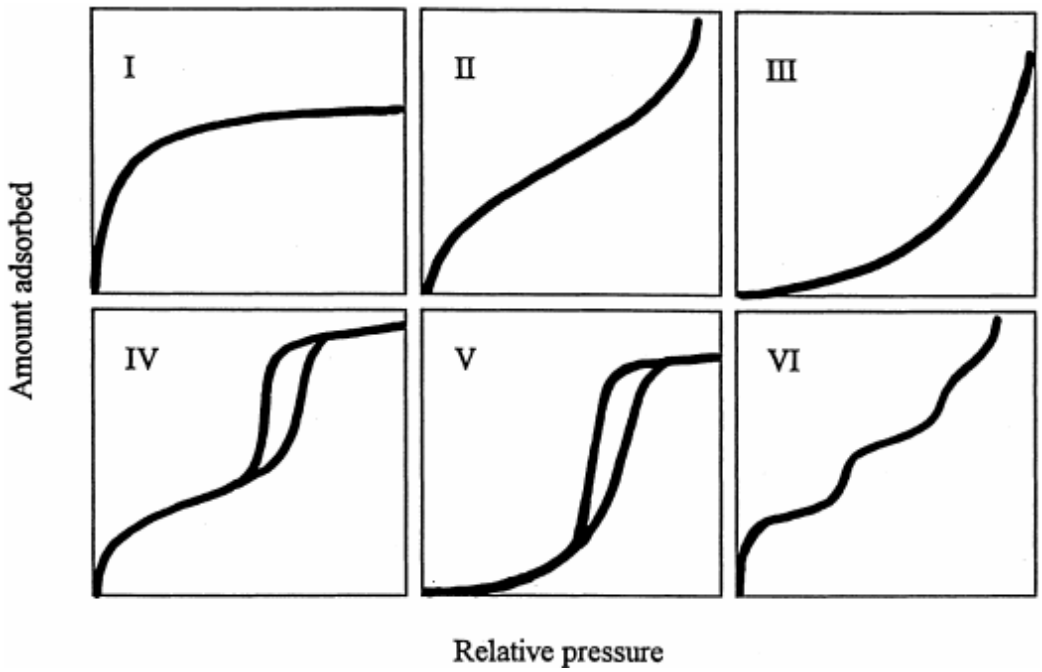

Figure 13: Types of adsorption isotherms according to the IUPAC classification.

The reversible Type I isotherm is obtained when the adsorption is limited to the monolayer and it is typical of microporous materials. The micropore filling and the high uptakes are observed at relatively low pressures, because of the narrow pore dimension and the high adsorption potential. Type II isotherms are typically recorded in case of nonporous or macroporous materials because unrestricted monolayers/multilayer adsorption can happen. In this type of isotherm, it is possible to observe an inflection point (knee) and this indicates the stage at which the monolayer is fully coverage and so the multilayer adsorption begins. The reversible type III isotherm does not show any inflection points and so this indicates that the attractive interaction between the adsorbate and the adsorbent are relatively weak. This kind of isotherm is not common. Type IV isotherms are typical of mesoporous materials. The most distinguished characteristic is the presence of the hysteresis loop which is associated with the pore condensation. The presence of the plateau covers a range of high p/p° which indicates complete pore filling. The initial part can be associated with to monolayer coverage like the Type II isotherms.

Type V isotherm shows pore condensation and hysteresis, but contrarily to type IV isotherm, the first part is similar to the type III, indicating a weak attractive adsorbent/adsorbate interaction. The type VI isotherm is a special case and formed by steps because the adsorption is non-uniform on a nonporous surface. The sharpness of the steps depends on the homogeneity of the surface and on the temperature.

Many models can be used for estimating the specific surface area depending on the shape of the isotherm. In the case of our carbons, all the sample show Type I. For this kind of isotherm, the suitable equation for evaluate the specific surface area is the Langmuir calculation. Using a kinetic approach, Langmuir can describe the type I isotherm with the assumption that the adsorption is limited to the monolayer. This type of isotherm usually describes microporous system, so it is possible to affirm that the carbon used in this thesis are microporous. Anyway, a convenient form of the Langmuir equation used is:

$$\frac{P}{W} = \frac{1}{KW_m} + \frac{P}{W_m} \qquad 1)$$

P is the gas equilibrium pressure, W and W_m are the adsorbate weight and monolayer weights, respectively. K is a constant. Plotting P/W vs P a straight line is obtained where $1/W_m$ is the slope- The specific surface area, S, of the samples is calculated with equation 5):

$$S = N_m A_y = \frac{W_m \bar{N} A_x}{\bar{M}} \qquad 2)$$

A_y is the cross-sectional adsorbate area, M is the gas molecular weight and N is the Avogadro's number.

The volume and the pore size distribution were evaluated with the Density Functional Theory (DFT). Many methods can be applied for estimate the

microporosity in a system, such as Horvath and Kawazoe, and Saito and Foley, but they do not give a realistic description of the filling inside the micropores and they tend to underestimate the porosity of the samples. Therefore, for the best fitting of the pore size and pore distribution in this thesis has been given by DFT simulation method assuming a slit geometry of the pores. The porosity evaluated is affected using the Nitrogen as gas analysis. Indeed, the Nitrogen is not satisfactory regarding to the assessment of the microporosity, especially in the range of ultra micropores (pores width less than 0,7 nm). The bilayer thickness of the nitrogen molecules is around 0,7 nm, so it cannot entre inside the ultra micropores. Moreover, at relative pressure of 10^{-7} to 10^{-5} the rate of diffusion and the adsorption equilibrium is very slow. These factors lead to time-consuming measurements and they can cause an under-equilibration of the adsorption isotherms affecting the result of the analysis. Anyway, the data obtained from the Nitrogen adsorption-desorption are suitable for the characterization of the carbon materials analyzed in this thesis.

2.3.2 Characterization of the samples with Attenuated Total Reflection (ATR) FT-IR

The ATR FT-IR (Perkin-Elmer Spectrum 100) was applied for understand the pyrolysis process that lead to the production of the porous carbon materials, from βCD, Lc, βNS and LcNS. Therefore, the ATR was used for collecting the spectra form the native materials and from the residue obtained at different pyrolysis temperature. In a typical procedure, 16 scans were recorded in the range of 4000-650 cm^{-1} with a resolution of 4 cm^{-1} employing as a detector a Globar source, DTGS.

2.3.3 Characterization of the samples with Scanning Electron microscopy (SEM)

The SEM (Leica streo-scan 410) was used for investigating the morphology of the samples before and after different pyrolysis temperature. The samples were set on a metallic stub with a double-sided conductive tape and covered with gold by a sputter coater (Bal-tec SCD 050) for 60 s under vacuum with a current intensity of 40 mA. The thickness of the gold layered is about 20 nm.

For the studies about C-βNS with S a field emission scanning electron microscopy (FESEM, JEOL-JSM-6700F) was used. Energy dispersive X-ray spectroscopy (EDS) of the composites was also performed using JEOL-JSM-6700F to investigate the Sulphur presence onto the structures of carbon.

2.3.4 **X Ray Diffraction (XRD)**

The XRD patterns were recorded on a Panalytical X'Pert PRO diffractomer with a PIXcel detector, using Cu Ka radiation, under the conditions of 2θ = 10–100° and 2θ step size = 0,03, to observe the presence of Sulphur in the S-loaded C-βNS samples.

2.3.5 **Pyrolysis studies**

The studies about the behavior of the βCD and LC and their relative NS was performed using the thermogravimetric analysis (TGA 2950 – TA Inc.). Precisely, about 15 mg of sample were sited in an alumina pan and then heated to 800°C under nitrogen flux (100 ml/min) with different ramp rate (from 10°C min^{-1} to 30°C min^{-1}).

2.3.6 **Gas adsorption properties**

For test the ability of the porous carbon materials in selectivity and capture of the CO_2, two methods were applied. The first approach is based on the heat develops during the adsorption; the second is a gravimetric system that allows to evaluate the adsorption in terms of weight of gas adsorbed. These techniques are widely explained in the two-following sub-paragraphs.

2.3.6.1 Microcalorimeter

The material was tested in gas adsorption through an adsorption microcalorimeter (Tian-Calvet type by Setaram) that allows to assess adsorbed amounts and heats of adsorption. The heat generates during the adsorption process is caused by a certain dosage of gas that produces a small difference in temperature. This alteration makes a voltage signal that is proportional to the heat flux and can be recorded. The heat of adsorption allows to evaluate the enthalpy changes related to the

adsorption process. The microcalorimeter is a high vacuum system (pressure residue 10^{-5} torr) and it is a gas-volumetric glass apparatus. During the experiment, both integral heats evolved, and adsorbed amounts can be measured. Two calorimetric cells are employed: one cell contains the sample in study whereas one cell is the reference and it is a blank used for minimizing the heat signal caused by the gas sent inside the system. Thanks to the construction of the apparatus, all parasitic phenomena (i.e., thermal effects that not provides form the adsorption) are successfully compensated. The microcalorimeter is composed by a metallic cylinder isolated from the surrounding and so the isotherms were performed at 303 K. For the measure of the pressure a transducer gauge is used (Barocell). The adsorbed amounts, reported per unit mass as a function of the equilibrium pressure (n_a vs p_e), are taken as a measure of the number of active sites involved in the gas adsorption. The differential heat of adsorption is expressed in function of the coverage (q_{st} vs n_a), is a result of the energy interaction between the gas and the surface. Another parameter that can be obtained from this type of measure, is the initial heat value (q_0). It is extrapolated from the heat of adsorption curve when the coverage is zero and, so it describes the energy of the most active sites. The calorimetric measures are performed in two runs. The first run (ads I) is performed on the sample after activation (outgassed overnight), the second one (ads II) is carried out after pumping off the reversible amount of gas adsorbed, in order to evaluate the irreversible component of the process.

Different gases were used, such as CO_2, CO, N_2 and O_2 (Rivoira 99,99% purity) keeping the samples (carbon from βNS and LcNS) at 30°C after a preliminary outgassing in vacuo at 30°C.

A scheme of the instrument is reported in Fig. 14:

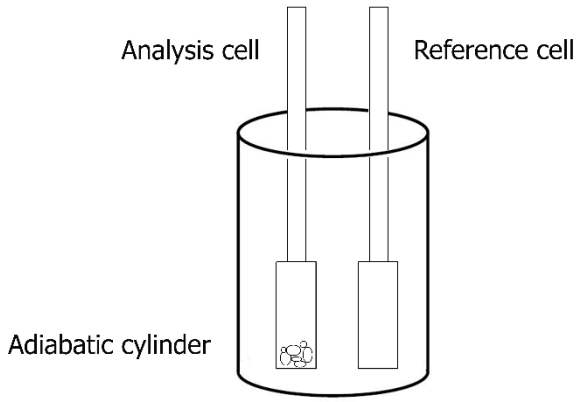

Figure 14: Scheme of the microcalorimeter apparatus

2.3.6.2 Microbalance

For better characterize the adsorption of CO_2 on the carbons from βNS and LcNS, the IGA 002 (Hiden) microbalance was used. This instrument allows to evaluate the vapor or gas sorption. The IGA is a very sensitive balance mounted in a thermostatic heatsink. It allows to control and measure the mass change, the pressure and the temperature in order to determinate the reproducibly of the isotherms in different analysis conditions. The microbalance is set up for working in the range of 0-20 bar (read with three different pressure transducer) and the temperature range of 77-1273 K thanks to the possibility to use three thermostats: a cryofurnace (77-323 K), a water bath (253-353 K) and a furnace (353-1273 K). The software investigates the relaxation behavior of the interaction process after pressure change in order to evaluate the kinetic parameters and the asymptotic uptake. The scheme of the apparatus is reported in Fig. 15 [116]:

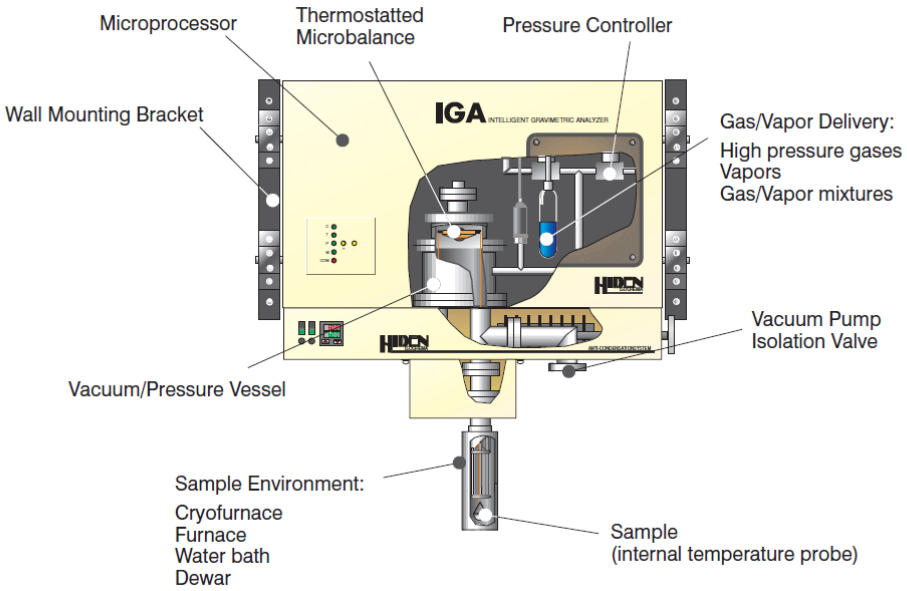

Figure 15: Scheme of the microbalance

For build the CO_2 adsorption/desorption isotherms the microbalance was used using both the water bath and the furnace for performing the experiments in the temperature range of 303-423 K. The pressure of 0-20 bar were used for the runs.

2.3.6.3 Temperature Programmed Desorption study

Temperature programmed apparatus allows the pre-treatment of solid material by heating and evacuation, its exposure to molecular species of and subsequent programmed desorption performed by heating in a controlled manner with the possibility to detect the desorbed gas in the carrier.

The interaction of gases with the C-LcNs sample has also been investigated by TPD experiments in a flow-reactor apparatus consisting of a quartz tube reactor (7 mm i.d.) connected to a mass spectrometer (Omnistar 200, Pfeiffer Vacuum), to a UV analyzer (Limas 11HW, ABB) and to a micro GC (Agilent 3000A) for the on-line analysis of the outlet

gases. The gases investigated were after a preliminary outgassing at 300°C:

1. C_3H_6 (1000 ppm)
2. H_2 (1000 ppm)
3. CO (1000 ppm)
4. NH_3 (1000 ppm)
5. CO_2 (1000 ppm)
6. NO (1000 ppm) + O_2 (3%)

All these gases have been adsorbed at 50 °C for several hours; then the samples were heated (10 °C/min) in He up to 300°C.

This analysis was carried out in collaboration with prof. Luca Lietti, dr. Chungcheng Liu and Valentina Azzariti of Politecnico of Milano

2.3.7 **Elemental analysis**

The elemental analysis was carried out using a Flash EA 112 serie CHNS-O Analyzer (Thermo Nicolet). The sample is weighed in Tin capsules, placed inside the instrument and then dropped into an oxidation/reduction reactor kept at a temperature of 900-1000 °C. All the organic and inorganic substances are converted into elemental gases which, after further reduction, are separated in a chromatographic column and finally detected.

2.3.8 **Electrochemical measurements**

Cells were assembled in Ar-filled dry glove box using an ECC-STD electrochemical cell configuration. The geometric area of the electrodes

was 2,54 cm^2. The cathode contained the different S-composite materials. To prepare them, acetylene carbon and poly-(vinylidenefluoride) binder, in the weight ratio of 80:10:10, were mixed in N-methyl-2-pyrrolidone solvent. The mixture was then casted on Al foil with film applicator to achieve Sulphur loading from 1,5 to 2 mg cm^{-2}. A lithium disc (18 × 0,2 mm) was used as the anode. A Celgard EH2010 (trilayer PP/PE/PP) and glass fibre 18 mm × 0.65 mm saturated in the electrolyte were used as the separator. In other cell configuration, glass fiber separator is replaced by carbon fiber paper (GDL, SIGRACET GDL-24BC) to adsorb catholyte. The electrolyte consisted of 1,2-dimethoxyethane (DME) and 1,3-dioxolane (DIOX) 1:1 (v/v) with 1 M lithium trifluoromethanesulfonate ($LiCF_3SO_3$, LiTFSI) and 0,25 M $LiNO_3$. The electrolyte to Sulphur ratio was kept 15 µL per mg of Sulphur. Cells were galvanostatically charged and discharged on an Arbin BT-2000 battery tester at room temperature. The cells were first discharged from open circuit potential to 1,8 V and then charged to 2,6 V. Initially, galvanostatic charging and discharging was performed at C/10 for the first 5 cycles. Onward cycling was carried out at C/5. The C rate and specific capacity calculation were made using a theoretical capacity of Sulphur (i.e. 1672 mA h g^{-1}).

2.3.9 **Isothermal adsorption of dyes from water**

The adsorption experiments were carried out in separate batch in closed test tubes (containing 10 mL solutions) under continuous shaking at 25°C. Prior to adsorption experiments, ca. 10 mg of the carbonaceous material were dispersed in 0,01M KCl solution to keep constant the ionic strength of the suspension. The final pH value was adjusted at 6,0±0,5 by drop wise addition of 0,1 M HCl or 0,1 M NaOH solutions and equilibrating for 24 hours. The isothermal study was conducted by adding to the suspensions the dye-containing solutions (previously prepared in KCl 0,01M and at pH=6) at different concentrations (C_0 from 50 to 1300 mg L^{-1} of dye). The adsorption was tested at circumneutral pH, which did not change during the experiments. Afterwards, suspensions were shaken in the dark for 24 hours at 25°C. After centrifugation, 3 mL of the supernatant was collected and directly measured by UV-Vis spectrophotometry (after performing an external calibration). The two

dyes selected for testing were examined at λmax(MB) = 664 nm and λmax(MO) = 465 nm. Furthermore, in order to optimize the capability of such materials in removing the probe dyes, an initial screening was realized by monitoring the depletion of the dyes main UV-Vis signals fixing the dye initial concentration at 100 mg L^{-1}.

The dyes concentration (C_e, mg L^{-1}) was determined spectrophotometrically using a double-beam spectrophotometer UNICAM UV 300 (Thermospectronic), equipped with both deuterium (for UV) and W (for Vis) lamps, using a PMMA cuvette of 1 cm of optical path, whereas the amount of dye sorbed (q_e, mg g^{-1}) was estimated as follows:

$$q_e = [V(C_0-C_e)]\ m^{-1} \qquad (3)$$

where C_0 is the initial dye concentration in the solution (mg L^{-1}), C_e is the equilibrium concentration of unadsorbed dye measured by UV-Vis analysis (mg L^{-1}), V is the solution volume (10 mL) and m is the sample mass (ca. 10 mg). To evaluate the efficiency of the sorbing materials, q_e can also be expressed as mg m_{-2} by dividing q_e for the BET specific surface area (m^2 g^{-1}) in order to obtain the adsorption capacity of 1 m^2 of adsorbing material.

To evaluate the regeneration capability of the materials, desorption experiments were performed for each separate batch by adding directly to the wet dye-containing samples (after filtration) the extracting media. Basically, two desorption washing steps were selected in sequence: a first washing step was carried out in 0,01M KCl at pH = 6, whereas the second one was performed subsequently in 0,1M NaOH. Contacts were performed by shaking the suspensions for 24 hours at 25°C in the dark.

In the end, for characterizing the adsorption exhibits by the C-βNS, a time-adsorption was performed, leaving the carbon in contact with the dye solution from 1 h to 7 h.

3 RESULT AND DISCUSSION

The results are divided in 4 paragraphs, in order to well-distinguished the characterization of the carbon obtained from NS and their application in three different fields: gas-adsorption, Li-S batteries and water treatment.

3.1 CHARACTERIZATION OF THE POROUS CARBON MATERIALS

In this part is widely treat the study on the pyrolysis of the Ns and the way to reach the better feature for the porous carbon materials form the βNS and LcNS.

3.1.1 Pyrolysis studies

Thermal gravimetric analysis was used for investigating the decomposition of the NS and for understanding the thermal stability of the carbon obtained in oxidative conditions. Thus, the TGA were primarily performed under nitrogen flow at different temperature, from RT to 800°C, to predict the best temperature to produce carbon materials with particular features and for determining the thermal behavior exhibited by the Ns. For better understand the thermal performances of the NS, a TGA under the same condition was performed for both βCD and LC.
The TGA in air on the residues collected at 800°C was used for providing information about the thermal stability of the samples and it allows to determinate the initial outgas condition necessary for the sorption analysis.
Fig. 16 shows the TGA curved obtained for the βNS and the βCD in nitrogen atmosphere with a ramp rate of 10°C/min to 800°C:

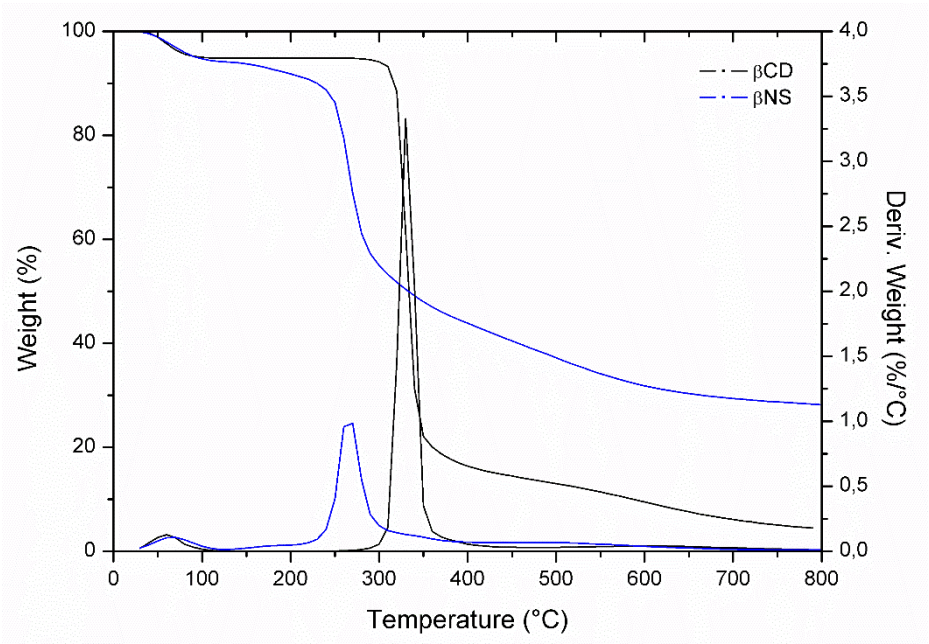

Figure 16: TGA and DTGA of βCD and βNS

During the thermal degradation of βCD and βNs a first step of weight loss can be observed. This represents the evaporation/dehydration and it starts immediately and finishing at 110°C. Following the thermal behavior exhibited by the βCD (black line) a main step of weight loss followed by a char rearrangement can be observed. This step is very sharp and fast and occurs between 270°C and 400°C with a 90% of weight loss. The second step starts from 400°C and it is a slow degradation of the char until 800°C. At the end of the measurement, the yield in carbon is about 9%. The βNS (blue line) shows the main step of weight loss at lower temperature than the βCD, between 220°C and 350°C with an only 42% of weight loss. Also, the rate of weight loss is different in this step and it is lower than the βCD, as it is possible to observe comparing the two DTGA curves. The second step goes from 350°C and 800°C and the nanosponge losses 14% of its weight and it leads to a yield carbon three times higher than the one observed for βCD (28%). It seems clear that the cross-linker strongly influence the pyrolysis, both in term of thermal stability and carbon yield. Thus, in order to clarify the role of the cross-linker during the thermal degradation, an ATR-IR analysis was carried out. In Fig. 17 the infrared spectra collected at several temperatures of the solid residues were

reported. In the bottom of the Fig. 17 it is possible to see the spectrum collected at room temperature and moving up, the spectra recorded at increasing temperature of pyrolysis.

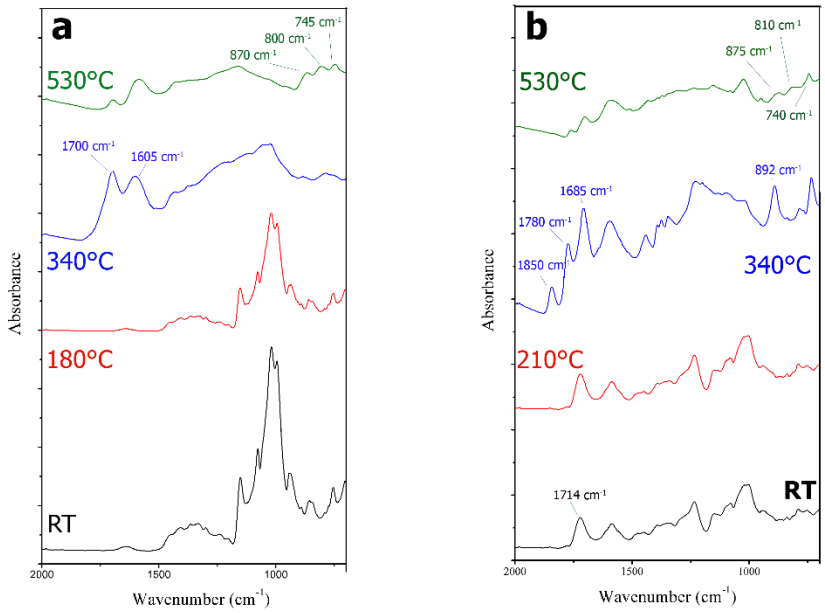

Figure 17: ATR Spectra of βCD (a), βNS (b) at ambient temperature and after heating in TGA.

Moving from RT to 180°C for the βCD (a), it is not possible to see any modification in the spectra. Increasing the temperature, up to 340°C, the sample shows a peak assigned to C=O bond stretching at 1700 cm^{-1}, but a further heating it tends to disappear. Simultaneously, a peak at 1600 cm^{-1} attributed to the C=C stretching of unsaturated species becomes stronger. Moreover, in the region between 1200 cm^{-1} and 900 cm^{-1} ascribed to the C=O stretching of the cyclodextrin tend to undergo to a series of modification with the temperature till disappearing. In the portion of spectra between 900 cm^{-1} and 700 cm^{-1} the formation of aromatic species is evidenced by the presence of three bands at 865 cm^{-1}, 805 cm^{-1} and 745 cm^{-1} ascribable to the out-of-plane mode of aromatic C-H. Fig.18 (b) shows the modification in the signals of the βNS caused by the pyrolysis. In the spectrum recorded at RT, it is possible to see the typical signal at 1714 cm^{-1} ascribable to the bonds between the βCD and the

cross-linker. This peak exhibits a gradual red-shift during the pyrolysis confirming the transformation of the ester bond. The spectra recorded at 340°C displays two new signals, at 1850 cm^{-1} at 178o cm^{-1}, characteristic of the pyromellitic dianhydride evidencing the breakage of the ester bonds of the NS. Moreover, in low frequency region the same three typical signals of out-of-plane mode appear, as shown for the βCD.

The same analysis was carried for the LcNs comparing the thermal degradation of the nanosponge with the one exhibited by the Lc. Thus, Fig. 19 depicted the TGA and the DTGA of the two samples carried out at 800°C under nitrogen flux.

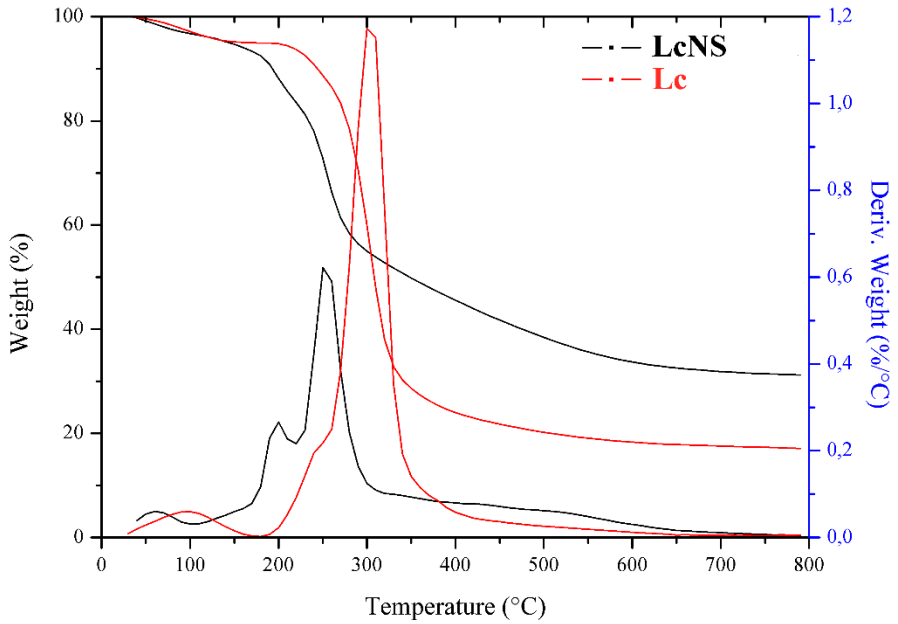

Figure 18: TGA of the Lc (red curves) and LcNS (black curves)

In the thermal degradation of the Lc (red line) three step of degradation can de distinguished. The first one denotes the evaporation/dehydration and it starts immediately and it finished at about 110°C. The weight loss in this step is around 5% and it depends on the moisture adsorbed by the sample. The second step corresponds to the thermal decomposition of the Lc. This stage starts at 200°C and finishes at 400°C and it represents the main step of weight loss in which the Lc losses the 76% of its initial weight.

The last step of degradation occurs between 410°C and 650°C and it can be defined as a slow thermal degradation of the char that leads to 17% of carbon yield. The thermal profile exhibited by the LcNS (black line) shows also three steps of degradation. The first step occurs before 100°C and it represent again the evaporation/dehydration of the moisture adsorbed by the NS. The second step takes place between 160°C and 310°C and it is caused by the thermal decomposition of the organic matter. The weight loss in this step is around 51% and so it is the main step of weight loss. Between 310°C and 600°C there is again a slow thermal rearrangement of the char leading at 32% of carbon yields. As shown by Fig. 18, there are some differences between the Lc and LcNS reactivity. The main step of degradation for the nanosponge begins at lower temperature, but with a realise of volatile lower than the Lc. Moreover, the pyrolysis lead to a higher amount of carbon. This differences in thermal behavior revealed that the presence of the cross-linker has a great influence on the carbonization, improving the charring reactions increasing the pyrolysis yield, as just discovered for the βNS.

For this reason, the same IR analysis was carried for the LcNs comparing the thermal degradation of the nanosponge with the one exhibited by the Lc. All the spectra recorder al different pyrolysis temperature for the two samples are shown in Fig. 19.

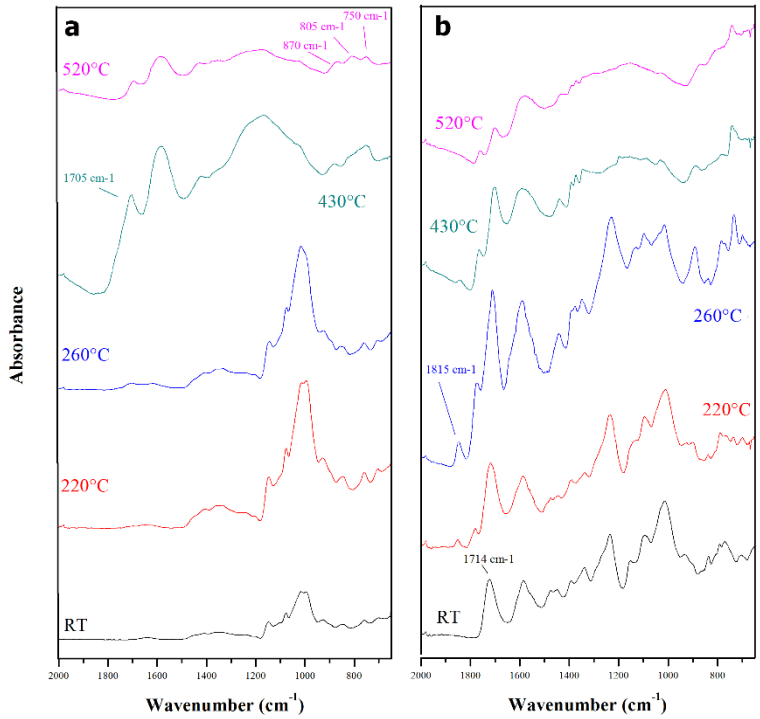

Figure 19: ATR spectra collected at different temperatures for the Lc (a) and LcNS (b)

Firstly, according to the TGA, there are no significant alterations among the spectra of Lc collected at RT, 220°C and 260°C. The degradation starts at 430°C where a peak around 1700 cm^{-1}, assigned to the C=O stretching, appears. Furthermore, a signal at 1600 cm^{-1}, attributed to C=C stretching, appears, testifying the presence of unsaturated species in the sample. Moving to the spectrum collected at 530°C, the peak at 1700 cm^{-1} decreases and in the low frequency region the three typical signals, already found in the spectra of the βCD and βNS, (870-806-750 cm^{-1}), of the out-of-plane aromatic C-H mode, appear. However, the same trend of degradation is showed by LcNS, but it also possible to see the signals belonging to the PMDA. Indeed, in the spectrum collected at RT it is visible a peak at 1714 cm^{-1} the is correlated with the ester bond between the Lc and cross-linker. Increasing the temperature, this bond decomposes generating a peak around 1815 cm^{-1} that it is attributed to the C=O stretching of the dianhydrides.

From the data collected for both the βCD and Lc and both the nanosponges, the conclusion is that the pyrolysis leads to an alteration of the saccharide structure and the scission of the bonds of the cross—linking bridges. Numerous unsaturated species are generated, and they increase in number during the pyrolysis, acting as a precursor for the rearrangement of the structure and the formation of the polycyclic aromatic structure typical of the char. The thermal decomposition of the βCD was widely studied and it was found out that there are many similarities with the one exhibited by the cellulose or starch [117]. The Lc showed the same degradation trend of the βCD, so the two decomposition routes can be compared. The analogies with the pyrolysis of the cellulose or of the starch are that both the materials can undergo pyrolysis via two competitive pathways. The first, called *dehydration*, in the matter the evolution light gases, such as CO_2, CO and H_2O prevails during the formation of the char. Simultaneously, the second path, named *depolymerization,* occurs leading to the formation of high boiling products, (tar) and the volatilization of them generating volatile products, particularly levoglucosan. This route involves intramolecular reaction and it is possible to affirm that the βCD and Lc follow, during the degradation, mainly this path. The presence of the cross-linker has a great influence on the pyrolysis path, favoring mostly the dehydration and so the formation of char. Thus, the PMDA alters the amount of residue produced affecting the competition between volatilization and carbonization. Basically, the cross-linking bridge is a very thermolabile ester bond which can be easily broken by the temperature and the formation of fragments that can interact among them reducing the quantity of volatiles released and consequently increase the amount of carbon produced. Moreover, the dehydration of the glucose rings of the βCD and of the Lc can also promote the generation of C=C bonds increasing the quantity of char produced. Fig. 19 shows this proposed route. Lastly the presence of an aromatic group in the PMDA can give a further contribution to the char yield. A schematic representation of the reactions involved during the pyrolysis is reported in Fig. 20:

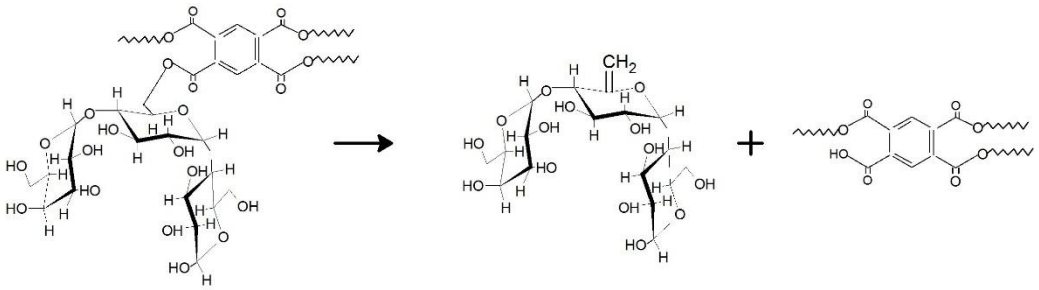

Figure 20: Schematic representation of decomposition of the NS

In term of thermal stability, the TGA in air condition was carried out for the carbons obtained after the pyrolysis of both the Ns, labelled C-βNs and C-LcNS. Fig. 21 depicts the curves of C-βNs (a) and C-LcNS (b) evaluated in air condition with a ramp rate of 10°C min^{-1} to 800°C:

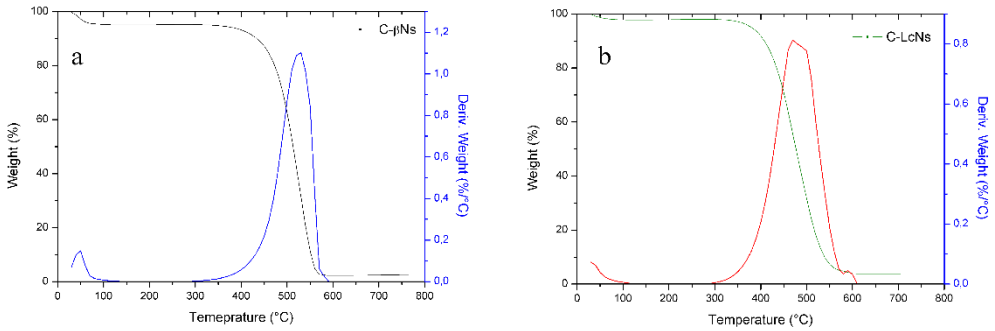

Figure 21: TGA curves of the thermal decomposition of the C-bNs and C-LcNs

As can be seen, the quantity of initial moisture for the two samples is different. Indeed, the carbon form βNs is able to adsorb a large amount of water (c.a 7%) respect to the LcNs (c.a 1%). Anyway, form the TGA curves it is possible to see that the sample mass of both the samples remains constant until 380-410°C. Then the mass of the carbons decreases dramatically up to 600°C where the samples are burned off completely, leaving no residue.

3.1.2 **Particle size and morphology**

For revealing the morphology and the particles dimension, the SEM was applied. This instrument can provide information about the particle size and geometry of the NS before and after the pyrolysis process. In Fig. 22 the micrographs of the βNS and C-βNS at different magnifications are reported.

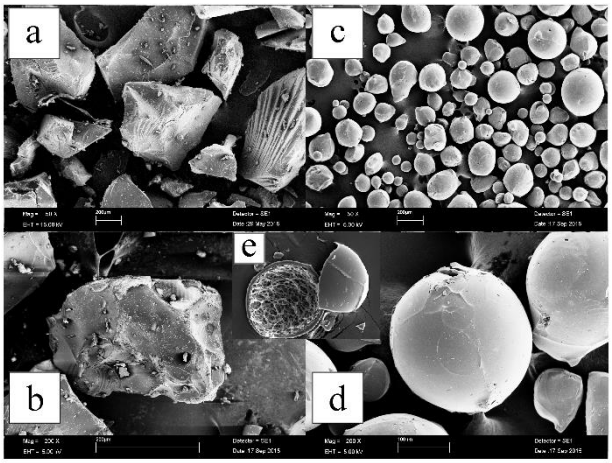

Figure 22: SEM micrographs of βNs (a-b) and C-βNS (c-d-e).

The βNs shows a polyhedral shape of the particles as can be revealed in panels a and b. This morphology is the result of the grinding process carried out after the synthesis. Indeed, the synthesis of the Ns leads to the formation of a solid block that requires to be grinded to obtain a homogeneous powder with a particle size about 200 mm. As it can be seen in panels c and d, the resulting carbon from βNs is composed of homogeneous spherical particles with a smooth surface. These particles were broken by mortar grinding, observed at a higher magnification (panel e) and were found to be hollow inside.
The same analysis was carried out for the LcNS and C-LcNS and the micrographs obtained at different magnification is reported in Fig. 22.

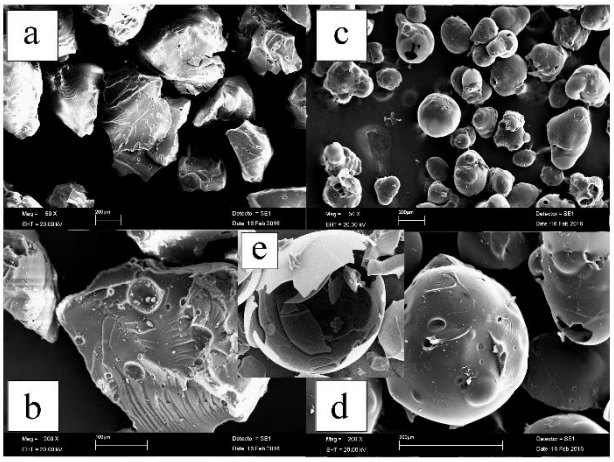

Figure 23: SEM micrographs of LcNs (a-b) and C-LcNS (c-d-e).

The particles of LcNS have the same polyhedral shape shown by the βNS for the reason described before. After the pyrolysis at 800°C, the carbon residue is composed of almost homogeneously distributed, spherical particles (panels c-d) and it is interesting to note that these particles are not stuck to each other but are physically distinct. Panel e in Fig. 23 shows that the particles are perfectly hollow inside, like observed for the carbon from βNs.

Having recognized that both the Ns leads to the formation of spherical particles perfectly hollow inside, it is possible to suppose that this peculiar morphology derived from a step of fluid phase before the carbonization. The surface tension during this stage drives to the formation of particles with spherical morphology. The cavity inside these particles suggest that after the charring of the surface, the volatile generates during the thermal degradation belongs essentially to the core. Since the surface of each particles seems to be almost smooth, but the volatile from the core permeates trough the walls of the sphere. Also, it is interesting to note that these particles are physically distinct probably due to the permeating volatiles that contributes to the separation of the single surface, voiding the sintering process.

3.1.3 **Outgas conditions**

The outgas procedure is a crucial step for obtaining a well-defined and reproducible surface, so a cleaning of the surface is required and all the adsorbed species, such as water, that could inhibit the adsorption of the gas analysis needs to be removed. This level of cleaning can be achieved keeping the samples at high temperature and high vacuum (typically about 10^{-6} mbar). The TGA was used for investigating the thermal stability of the samples. As can be seen in Fig. 18 reported in paragraph 3.1.2, the samples outgassing can be performed at any temperature from the range of 110°C-380°C. Basically, it was decided to outgas the C-βNs and C-LcNs at 300°C after a preliminary outgassing at RT for 2 hours. The thermal treatment at 300°C was applied for 6 hours, until the pressure residue is about 10^{-6} mbar and this value remain constant for 1 hour. This outgas method was applied for the preparation of the samples before any type of gas-adsorption measurement (ASAP 2010 and microbalance), except for the microcalorimetric studies, where the outgass was performed at 30°C.

3.1.4 **Nitrogen adsorption isotherm: determination of the specific surface area and porosity**

For determine the specific surface area of the samples and the porosity the ASAP 2010 volumetric analyzer was used.
Fig. 24 shows the nitrogen adsorption isotherm obtained for the C-βNs at 77K.

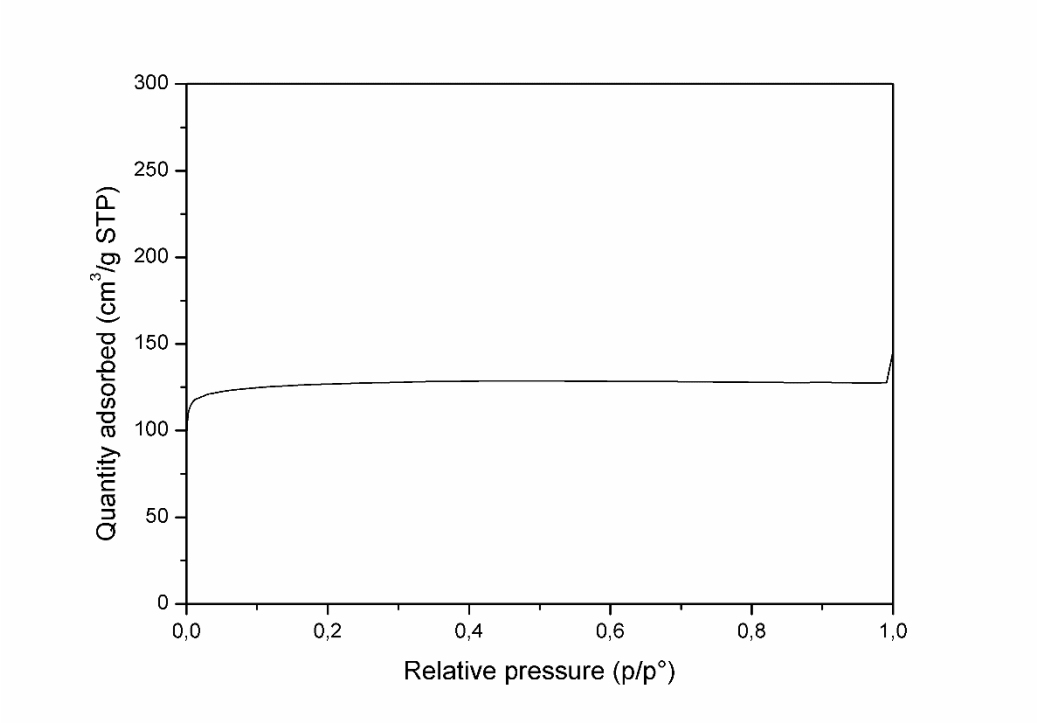

Figure 24: N_2 adsorption isotherm at 77K performed for C-βNs

The shape of the nitrogen isotherm is very important for understanding which type of porosity is present in the system. For the C-βNS, it is possible to see that the isotherm depicted in Fig. 24 is a typical Type 1 isotherm (according to the IUPAC classification). This is characterized by a long horizontal plateau until the saturation pressure is reached (p/p°=1). The isotherm shows a steeply increasing region at low relative pressure, less than 0,02, which stands for the adsorption or condensation in micropores.

Then the N_2 adsorbed amount remains constant, with no evidence of the presence of capillary condensation, indicating the absence of mesopores. The same trend of adsorption in showed by the C-LcNS, as reported in Fig. 25.

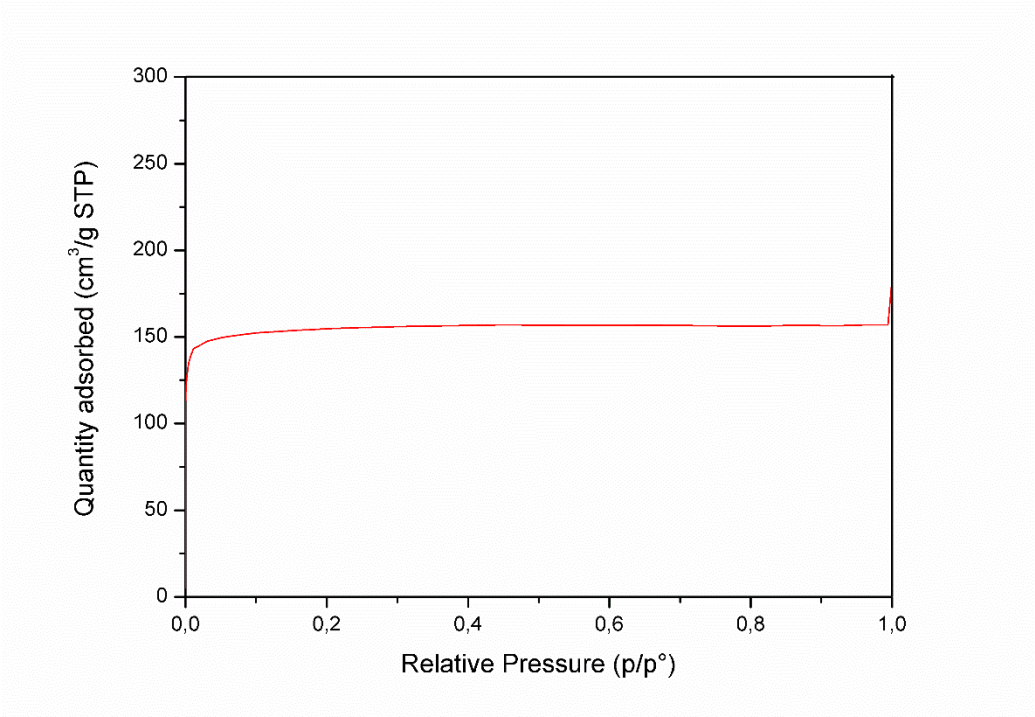

Figure 25: N2 adsorption isotherm at 77K performed for C-LcNs

For evaluating the specific surface area of the carbons, the Langmuir equation has been applied. Otherwise, for determining the micropore volume and the pore size distribution, the Density Functional Theory (DFT) method has been used assuming a slit pore geometry in carbon materials for the N_2 77K adsorption. Table 4 summarizes the results in terms of area and porosity obtained for the two samples:

Sample	Specific surface area (m^2/g)	Volume of micropores (cm^3/g)	Pore width (Å)
C-βNS	560	0.05	5-16
C-LcNs	682	0.18	5-17

Table 4: Specific surface area, cumulative pore volume and pore width of different carbonized

The C-LcNS has a higher specific surface area than the C-βNs (682 m^2/g with respect to 560 $m^2\ g^{-1}$) resulting in a more extended microporosity (0,16 cm^3/g with respect to 0.05 cm^3/g). Fig. 26 depicts the DFT elaboration of the adsorption data in order to have a graphical elaboration of the pore diameter size:

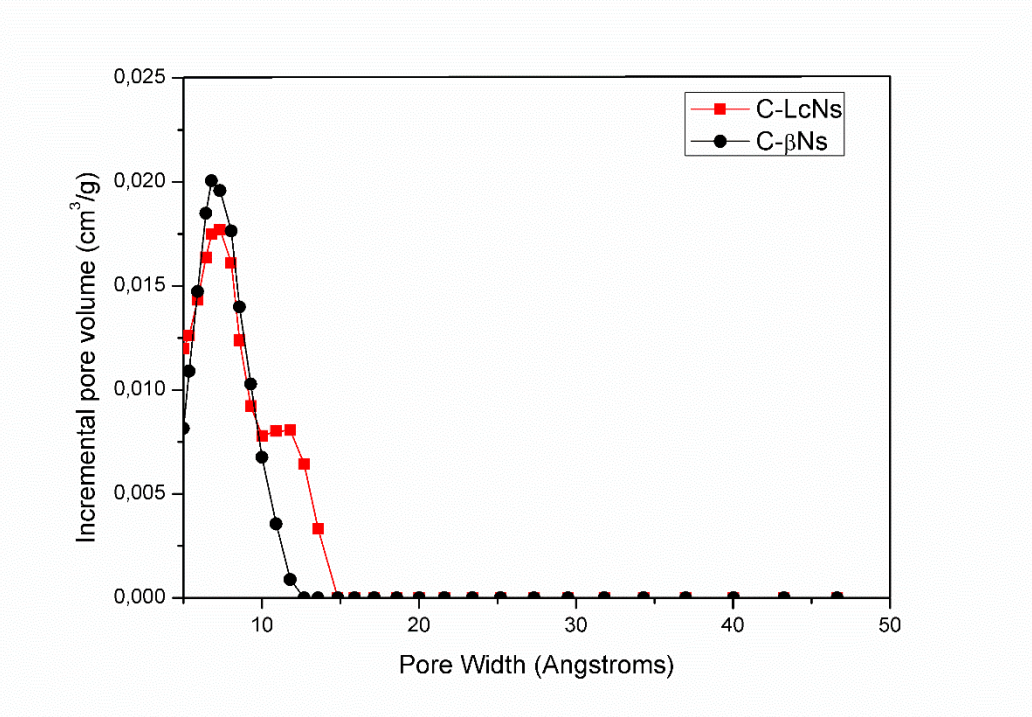

Figure 26: DFT pore size distribution curves of the C-LcNs (red line) and of the C-βNs (black line)

All the curves start from 5 Å, because this is the limit of the nitrogen measurement. It is interesting to note the bimodal distribution of the pores shown by the C-LcNS.
In conclusion, the carbon from C-LcNS has a wider area and consequently a higher porosity than the carbon form C-βNS. This result could be interesting for potential gas adsorption applications.

3.1.5 **Effect of the heating rate on the final carbon**

The βNs and LcNS were subjected to three different heating rates, 10°C min^{-1}, 20°C min^{-1} and 30°C min^{-1} in the tubular furnace under Nitrogen flux. The residue collected for the samples were analyzed using the ASAP 2010 in order to evaluate the physical properties of the carbon. In table 5 are reported the specific surface area evaluated with the Langmuir model and the porosity in term of volume and dimension measured with the DFT method for the C-βNS and C-LcNS.

Samples	**Specific surface area ($m^2 g^{-1}$)**	**Pore Volume ($cm^3 g^{-1}$)**	**Pore width (Å)**
C-βNS 10°C min^{-1}	498	0,07	5-8
C-βNS 20°C min^{-1}	450	0,12	5-11
C-βNS 30°C min^{-1}	502	0,12	5-16
C-LcNs 10°C min^{-1}	682	0,16	5-15
C-LcNs 20°C min^{-1}	434	0,11	8-15
C-LcNs 30°C min^{-1}	34	0	0

Table 5: Specific surface area, pore volume and pore width of the different carbons.

It is possible to see that for the βNS the heating rate has not an influence on the physical properties of the final carbons. For the LcNS, a fast heating rate inhibits the development of the specific surface area and of the porosity of the systems. Probably, 30°C min^{-1} prevents the rearrangement of the structure. It is note that the pyrolysis of the precursor forms void spaces in the carbon matrix and they are generated by the misalignment of the aromatic microdomains. These misalignments provide the porosity the system. A fast ramp rate avoids, in the case of LcNS, the development of this empty spaces. Moreover, it is possible to suppose that the volatiles could be generated too fast during the pyrolysis and so they not have enough time for leaving the system blocking the pores developing. All these events can only cause the decreasing of the specific surface area and the reduction of the total volume of the pores.

3.1.6 **Effect of the catalyst in the synthesis of the βNS and on the final carbon**

In the classical synthesis of the βNS the molar ratio between the βCD and the TEA is 1:8. For obtaining a carbon with better physical characteristics, the quantity of catalyst has been decreased in order to improve the properties of the sample and to lead the synthesis towards more green preparation, amine-free. In table 6 are reported the quantity of reactants used, the yield of the synthesis and the time required for completing the cross-linking reaction.

Molar ratio βCD-TEA	**Yield**	**Time**
1-8	98%	few seconds
1-4	98%	few seconds
1-2	85%	30 minutes
1-0,8	60%	2 days
1-0,08	20%	1 week

Table 6: Amount of TEA, yield and time required for the synthesis

The molar ratio 1:8 and 1:4 βCD:TEA leads to have a high yield of synthesis and the cross-linking reaction is very fast. Moving to the βCD:TEA 1:2 the amount of nanosponge that can be obtained decreases and the reaction needs more time. Decreasing the TEA amount of 10 times or 100 times respect to the classical synthesis, slows dramatically the cross-linking reaction and the yield in nanosponge falls. In conclusion, high amount of TEA is required for rendering the synthesis efficient. Anyway, all the samples obtained with different molar ratio between the βCD and TEA were subjected to pyrolysis at 800°C. The residues were collected, and the specific surface area and the porosity were evaluated using the ASAP 2010. The specific surface area was evaluated with the Langmuir

equation, while the porosity with the DFT method. The results are reported in table 7:

Sample	Surface Area	Micropore Volume	Pore Width
	($m^2\ g^{-1}$)	($cm^3\ g^{-1}$)	(Å)
1-8 Post pyrolysis	560	0.15	5-13
1-4 post pyrolysis	524	0.16	5-12
1-2 post pyrolysis	531	0.11	5-12
1-0.8 post pyrolysis	434	0.15	5-13
1-0.08 post pyrolysis	606	0.11	6-12

Table 7: Physical properties of the carbon from different βNS:TEA ratios

From these data, it is possible to conclude that the TEA has not any type of influence in the development of the specific surface area or in the growth of the pores. It seems that the TEA is not involved in the pyrolysis reactions that lead to the formation of the porous carbon materials form βNS. Anyway, for an efficient and fast synthesis of the NS high amounts of TEA are compulsory.

In the way of synthesis of NS with different molar ratio βNS:TEA, it was evaluated the possibility to obtained NS and so carbons with higher physical characteristic, employing other two catalysts were employed: triethanolamine (TEAOH) and 1,4-diazabicyclo[2.2.2]octane (DABCO). The synthetic conditions were the same used in the classical synthesis. It was possible to obtained a cross-linking reaction using only 1:1 βCD:TEAOH and 1:4 βCD:DABCO. The two NS were pyrolyzed and then their residues were collected and analyzed using the ASAP 2010, using the Langmuir equation for the specific surface area and the DFT for the pore system. The results are listed in table 8:

Sample	Surface Area	Micropore Volume	Pore Width
	($m^2\ g^{-1}$)	($cm^3\ g^{-1}$)	(Å)
C-βNS TEAOH	587	0,16	5-9 10-16
C-βNS DABCO	323	0,07	5-16

Table 8: Physical characteristics of the two carbons from βNS TEAOH and βNS DABCO

The use of the TEAOH in the synthesis seems to lead to a carbon with the same characteristic obtained with the one with TEA. Cornerwise, the presence of DABCO inside the structure of the NS has an influence on the pyrolysis that generates a carbon with less pores and consequently a lower specific surface area respect to the carbons from βNS with the TEA as catalyst.

3.1.7 **Effect of the cross-linker in the synthesis of the βNS and on the final carbon**

For obtaining a carbon with better physical characteristics, the other dianhydride has been used in order to improve the properties of the final product. The dianhydride investigated were:

- Epliclon;
- 1,4,5,8-Naphthalene-tetracarboxylic dianhydride (NTD);
- 3,3',4,4'-Biphenyltetracarboxylic dianhydride (BD);
- Ethylenediaminetetraacetic dianhydride (EDTA);
- Benzophenone-3,3',4,4'-tetracarboxylic dianhydride (BPD);
- Perylene-3,4,9,10-tetracarboxylic dianhydride (PD);
- 4,4'-(Hexafluoroisopropylidene)diphthalic anhydride (HFEDA).

For obtaining this Ns the classical synthesis used for the βNs has been done, so the same amount of triethylamine was used and the ratio between the βCD:cross-linker was 1:4.

Following the classical procedure, was not possible to obtain a hyper-cross-linked polymer for all the cross-linker reported. Fig. 27 is a schematic representation of the results obtained for the various synthesis:

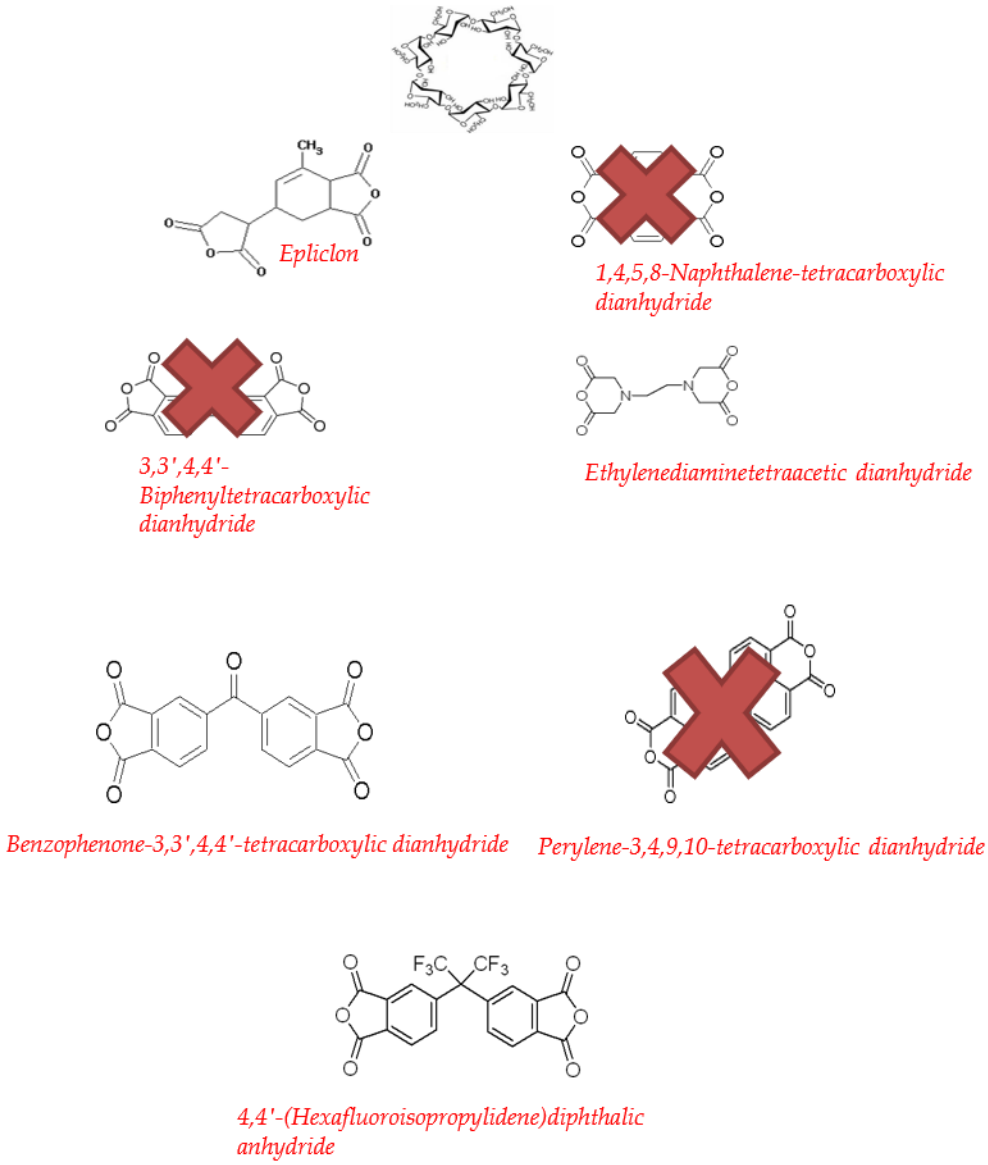

Figure 27: Schematic representation of the results obtained for the synthesis

From Fig. 27, it is possible to see that only epiclon, EDTA, BPD and HEFSA work as a cross-linker using the classical synthesis. For understanding if the synthesis for being performed required time, all the samples were left to react for one month. After that time, the reaction was considered not possible.

In table 9 are reported the yield of the synthesis and the time required for completing the cross-linking reaction for the four cross-linker considered suitable for the synthesis:

Cross-linker	Yield	Time
epiclon	89%	few seconds
EDTA	75%	2 days
BPD	40%	1 week
HEFSA	97%	few seconds

Table 9: Yield and time required for the synthesis

For understanding if it was possible to obtain a porous carbon material, all the samples were subjected to pyrolysis at 800°C. The yield in pyrolysis for the four Ns were reported in table 10:

Cross-linker	Yield
epiclon	10%
EDTA	13%
BPD	21%
HEFSA	25%

Table 10: Yield in carbon after the pyrolysis

All the Ns have a yield in pyrolysis that is less than the one observed fot the βCDNs (28%).

The residues were collected, and the specific surface area and the porosity were evaluated using the ASAP 2010. The specific surface area was

evaluated with the Langmuir equation, while the porosity with the DFT method. The results are reported in table 11:

Sample	Surface Area	Micropore Volume	Pore Width
	($m^2\ g^{-1}$)	($cm^3\ g^{-1}$)	(Å)
βCD - epiclon	/	/	/
βCD - EDTA	/	/	/
βCD - BPD	/	/	/
βCD - HEFSA	710	0.15	5-13

Table 11: Physical characteristics of the four carbons from βNS

The HEFSA-nanosponges shows a very high specific surface area and a narrow pore size distribution. It will be interesting in the future to characterize this type of materials in the same application of the C-βNS, because during the Ph.D. were not investigated.

3.1.8 Effect of the cross-linker in the synthesis of the Lc and on the final carbon

The same cross-linker used for the βCD were tested for synthetizing the nanosponge from Lc. For obtaining these Ns the classical synthesis used for the Lc has been done, so the same amount of triethylamine was used and the ratio between the Lc:cross-linker was 1:4.

Following the classical procedure, was not possible to obtain a hyper-cross-linked polymer for all the cross-linker reported. Fig. 28 is a schematic representation of the results obtained for the various synthesis:

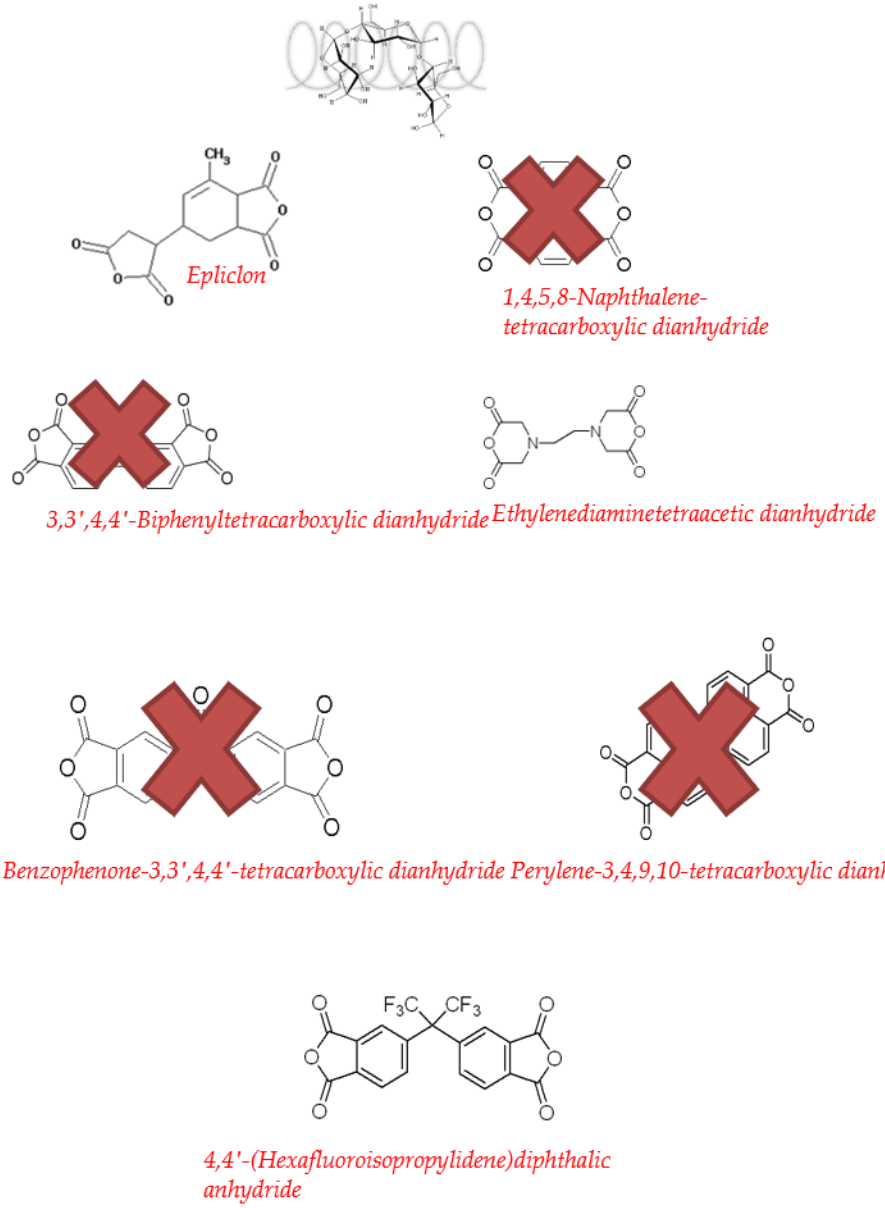

Figure 28: Schematic representation of the results obtained for the synthesis

From Fig. 28, it is possible to see that only epiclon, EDTA and HEFSA work as a cross-linker using the classical synthesis. For understanding if the synthesis for being performed required time, all the samples were left to react for one month. After that time, the reaction was considered not possible.

In table 12 are reported the yield of the synthesis and the time required for completing the cross-linking reaction for the three cross-linker considered suitable for the synthesis:

Cross-linker	Yield	Time
epiclon	79%	few seconds
EDTA	68%	1 hour
HEFSA	97%	few seconds

Table 12: Yield and time required for the synthesis

For understanding if it was possible to obtain a porous carbon material, all the samples were subjected to pyrolysis at 800°C. The yield in pyrolysis for the four Ns were reported in table 13:

Cross-linker	Yield
epiclon	18%
EDTA	13%
HEFSA	26%

Table 13: Yield in carbon after the pyrolysis

All the Ns have a yield in pyrolysis that is less than the one observed for the LcNs (32%).

The residues were collected, and the specific surface area and the porosity were evaluated using the ASAP 2010. The specific surface area was evaluated with the Langmuir equation, while the porosity with the DFT method. The results are reported in table 14:

Sample	Surface Area	Micropore Volume	Pore Width
	($m^2\ g^{-1}$)	($cm^3\ g^{-1}$)	(Å)
Lc - epiclon	328	0,09	10-17
Lc - EDTA	/	/	/
Lc - HEFSA	1083	0,22	15-16

Table 14: Physical characteristics of the four carbons from LcNs

From the results, it is possible to see that only the Lc-EDTA has non-detectable area. The Lc-epiclon shows a quite high surface area, of about 328 $m^2\ g^{-1}$, whereas in the same condition and pyrolysis the βCD-epiclon has no area. Moreover, as observed for the βCD-HEFSA, the carbons from Lc-HEFSA displays a very high surface area, higher then the one recorded the C-βNS and C-LcNs, that was 560 $m^2\ g^{-1}$ and 682 $m^2\ g^{-1}$, respectively. The HEFSA seems to be a very suitable cross-linker for the synthesis of both kind of Ns, showing a very high reactivity during the synthesis leading to a high yield in Ns. Furthermore, the pyrolysis of both the Ns from Lc and βCD-HFESA lead to a high yield of carbon that show a very a high specific surface area and a narrow pore size distribution. Unfortunately, no more analyses were performed in order to evaluate some possible industrial applications.

3.1.9 Effect of saccharides in the synthesis of the Ns and on the final carbon

The classical synthesis of the NS was perfomed using other sugar: Cyclic Nigerosyl-(1→6)-nigerose (CNN) and the glucose. In table 15 are reported the yield of the synthesis and the time required for completing the cross-linking reaction.

Sugar	Yield	Time
CNN	88%	few seconds
Glucose	99%	few seconds

Table 15: Yield and time required for the synthesis

The reaction between the CNN or the glucose with the pyromellitic dianhydride is very fast and also very exothermic, so in particular for the glucose, required to use an ice-water bath (about 0°C) during the reaction for avoiding the caramelization of the Ns. The yield in cross-linked polymer is very high using the glucose.

For understanding if it was possible to obtain a porous carbon material, all the samples were subjected to pyrolysis at 800°C. The yield in pyrolysis for the two samples were reported in table 16:

Sugar	Yield
CNN	16%
Glucose	23%

Table 16: Yield in carbon after the pyrolysis

All the samples have a yield in pyrolysis that is less than the one observed for the βNs and LcNs (28% and 32%, respectively).

The residues were collected, and the specific surface area and the porosity were evaluated using the ASAP 2010. The specific surface area was evaluated with the Langmuir equation, while the porosity with the DFT method. The results are reported in table 17:

Sample	Surface Area	Micropore Volume	Pore Width
	($m^2\ g^{-1}$)	($cm^3\ g^{-1}$)	(Å)
CNN-PMDA	145	0,03	10-17
Glucose-PMDA	910	0.15	7-18

Table 17: Physical characteristics of the four carbons from LcNs

From the results, it is possible to see that both the carbon from different sugars has an area. CNN-PMDA shows a low surface area, of about 145 $m^2\ g^{-1}$, whereas in the same condition and pyrolysis the glusose has a very high specific surface area. Moreover, the carbons from cross-linked glucose displays a very high surface area, higher than the one recorded the C-βNS and C-LcNs, that was 560 $m^2\ g^{-1}$ and 682 $m^2\ g^{-1}$, respectively. The glucose seems to be useful starting material for the synthesis of an hyper cross-linked polymer, showing a very high reactivity during the synthesis. Also, the CNN can be applied for the synthesis of cross-linked polymer, but the yield in pyrolysis and the low specific surface area, makes them unsuitable for the production of porous carbon materials. On the contrary, the pyrolysis of the glucose-PMDA lead to a high yield of carbon that shows a very a high specific surface area and a narrow pore size distribution. Unfortunately, no more analyses were performed in order to evaluate some possible industrial applications for both the samples.

3.1.10 Effect of water in the Ns and on the final carbon

First, it is introduced the definition of Swelling: gross structure of material as a moiety of particles, fibers, or a film (i.e., solid cellulosic phase) maintained, despite significant changes of physical properties and an increase in sample volume due to uptake of the swelling agent.

Ns are generally insoluble in water and in common organic solvents, even if some classes of them exhibit properties of swelling in the presence of aqueous solutions, giving rise to a gel-like behavior, similar to hydrogels. The possibility to obtain a gel-like structure could increase the porosity of the carbon from bNs. The gel of Ns was prepared by adding to the powder

of βNs a suitable amount of double-distilled water in order to obtain the maximum level of hydration h =5, whereas h is defined as weight ratio H_2O:βNs. The gel-like βNS picture is reported in Fig. 29:

Figure 29: βNS swollen

A TGA analysis of the swollen βNS was performed in order to evaluate the quantity of water present in the sample. The TGA was carried out in N_2 at 10°C min^{-1} to 800°C. The result obtained is reported in Fig. 30:

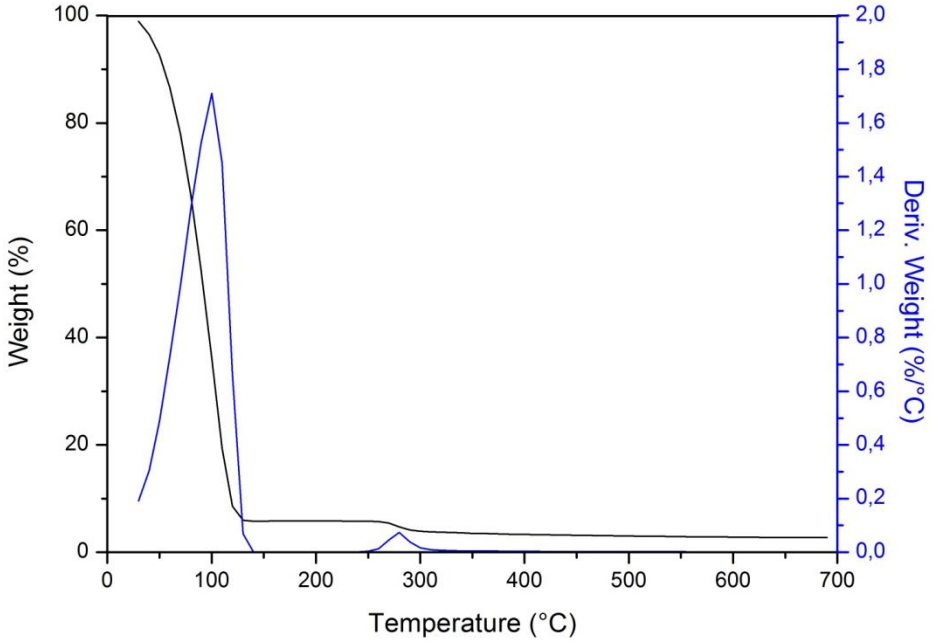

Figure 30: TGA of the swollen βNs

As expected, the 95% of the weight of the sample is composed by adsorbed water. Indeed, the main step of weight loss starts immediately and finishes at about 130°C, testifying that this step can be due mainly to the evaporation of the water used for the swelling.

For understanding if there were some modification in the chemical structure of the βNS, an ATR-FTIR analysis was performed and in fig 31 are reported the spectra recorded compared with the one of the βNS:

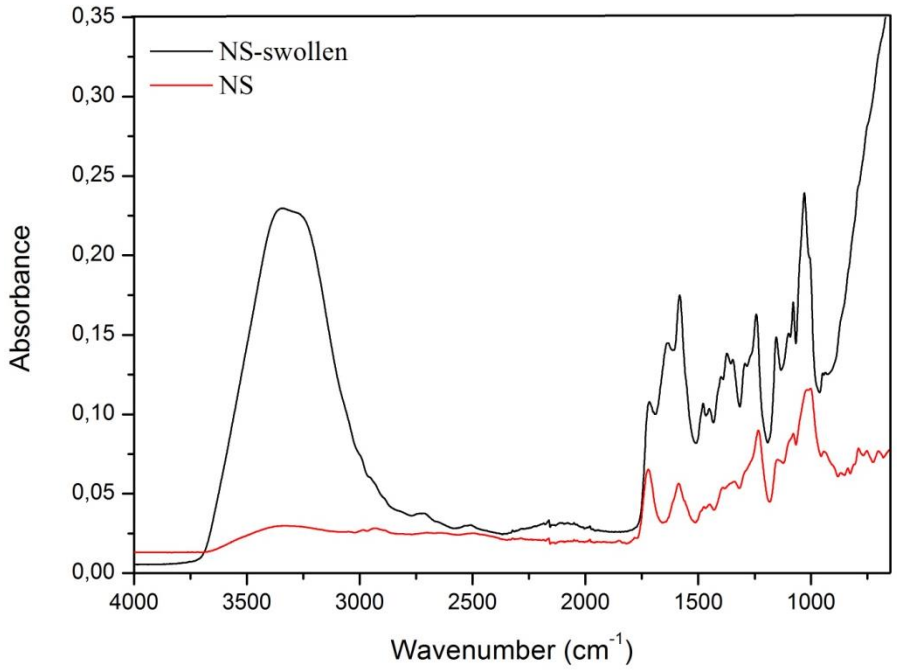

Figure 31: ATR spectra recorded for the βNs (red line) and the βNs-swollen (black line)

There are some differences in the two spectra. The first one it can be ssen in the range of the OH stretching, between 4000 and 3000 cm^{-1}. The second is between 1750 and 1550 cm^{-1}. For better underline this two differences the two range of spectra are reported in Fig. 32:

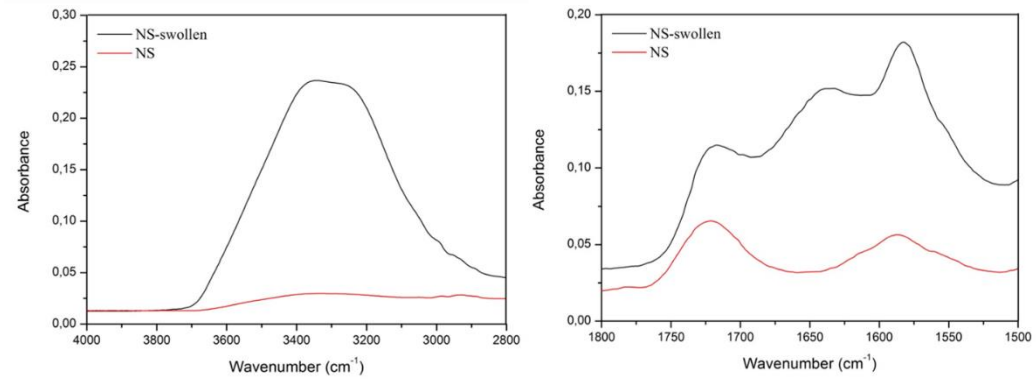

Figure 32: Two portion of the spectra of βNs and βNs-swollen

The increase of the band at 3330 cm^{-1}, attributed to the OH stretching suggest the presence of water in the structure. This is also confirmed by the appearing of a band at 1658 cm^{-1} that is typical of the water.

The βNs-swollen were subjected to pyrolysis at 800°C. The residues were collected, and the specific surface area and the porosity were evaluated using the ASAP 2010. The specific surface area was evaluated with the Langmuir equation, while the porosity with the DFT method. The result is reported in table 18:

Sample	**Surface Area**	**Micropore Volume**	**Pore Width**
	($m^2\ g^{-1}$)	($cm^3\ g^{-1}$)	(Å)
βNs-swollen	133	0,033	11-15

Table 18: Physical properties of the carbon from different βNS-swollen

It is possible to see that the βNs-swollen is not a good starting material for the synthesis of porous carbon. Indeed, during the pyrolysis, all the water adsorbed is rapidly realized before the degradation of the Ns. Moreover, it is possible to suppose that the water can hydrolyzed the ester bond between the βCD and PMDA, altering the structure of the Ns. It is not possible to evaluate from the TGA if the presence of water can alter the amount of char and so if there are some modification of the pyrolysis pathway follow by the Ns, but it is possible to affirm that the presence of water surely alters the formations of the pore structure in the final carbon causing the reduction the specific surface area. Thus, the Ns-swollen can not be use as a suitable precursor for the formation of porous carbon materials.

3.1.11 **Influence of the particle size on the final carbon from βNs**

The βNS after the synthesis are subjected to a grinding process. The dimension of the final carbon for both the samples depends on the size of the starting materials. For this reason, it was evaluated the possibility to modify the specific surface area changing the dimension of the Ns particle size.
For doing this the ball mill was applied and then sieved. The different size fractions obtained were:

- Over 100 μm
- Under 100 μm
- Under 40 μm

In Fig. 33 are reported the micrographs obtained for the three different parts collected using the SEM:

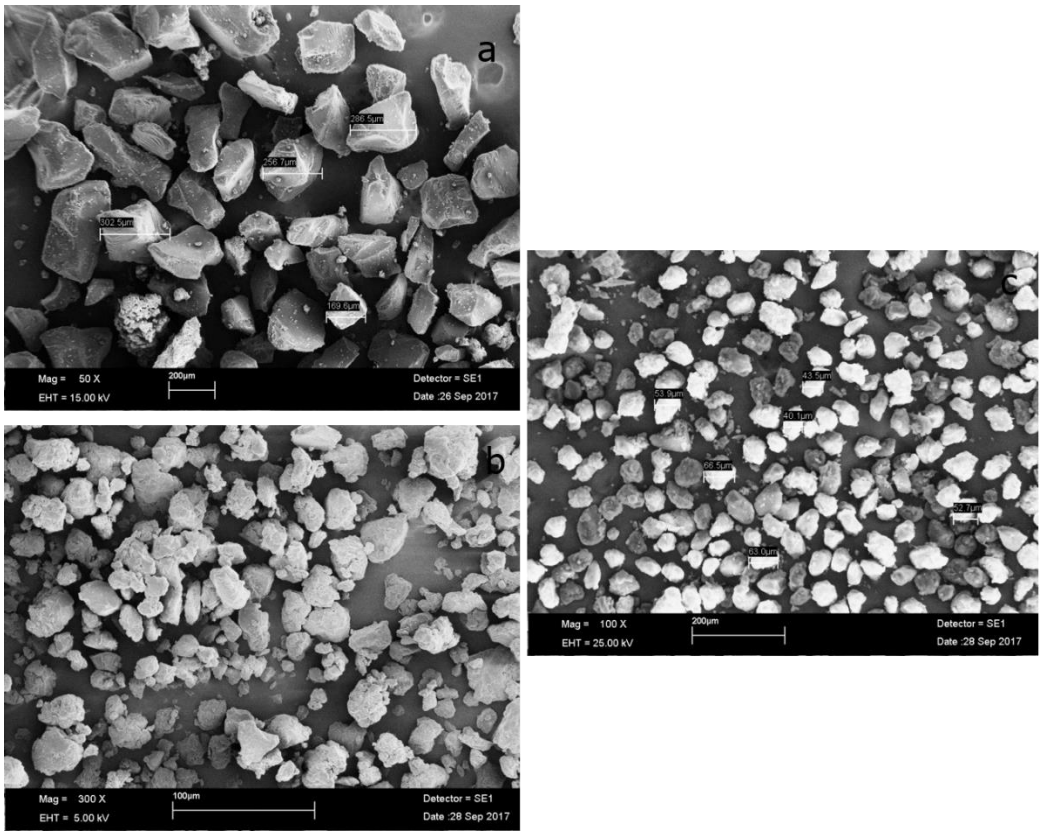

Figure 33: SEM micrographs of the βNs > 100 μm (a); βNs < 100 μm (b); βNs < 40μm (c)

The SEM confirms that the sieving process lead to have particle with the desire dimensions.

A TGA analysis of the samples was performed in order to determinate the yield of pyrolysis and for being sure that the dimension of the particles does not influence the pyrolysis process. The TGA was carried out in N_2 at 10°C min^{-1} to 800°C. The result obtained is reported in Fig. 34:

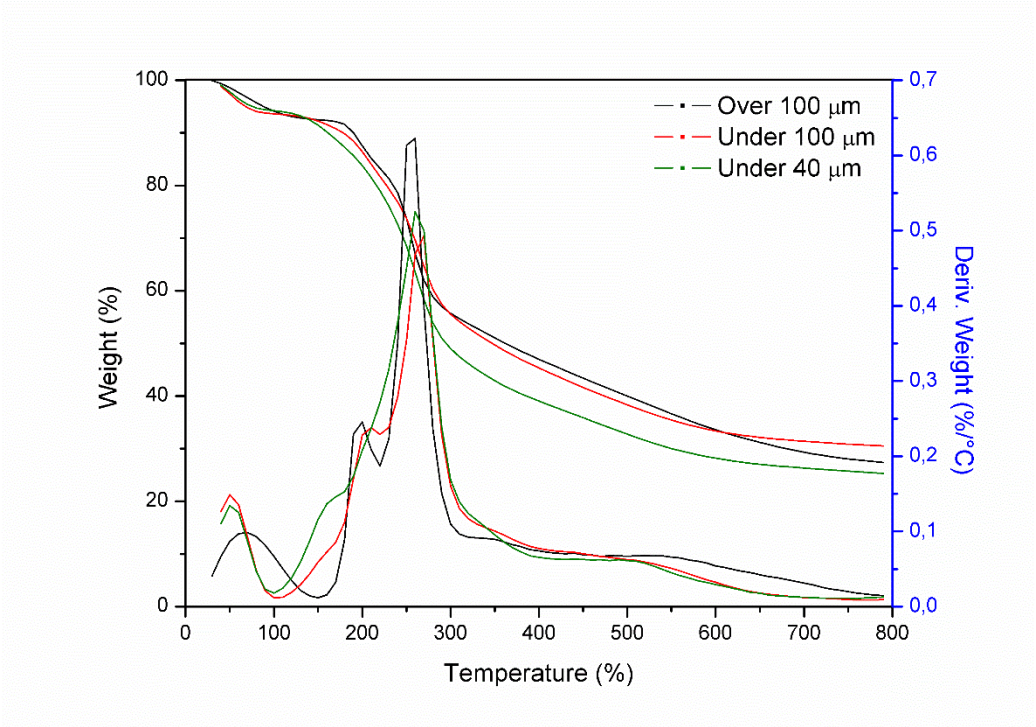

Figure 34: TGA of the βNs > 100 μm (black line); βNs < 100 μm (red line); βNs < 40μm (green line)

Decreasing the dimension of the particles there is a little shift to lower temperature (from 200°C to 210°C) of the main step of degradation. Is note that the dimension of the particles has an influence on the the thermal behavior of a sample due to the difficult of the heat to penetrate large samples [118]. More interesting is that the sample that contain particle less large than 100 μm has the high amount of carbon at 800°C (28% respect to 25% for the sample over 100 μm and 23% pf the sample under 40 μm).

After the pyrolysis, the residue of the three samples was collected and the morphology and the dimensions were evaluated using the SEM. The micrographs were reported in Fig. 35:

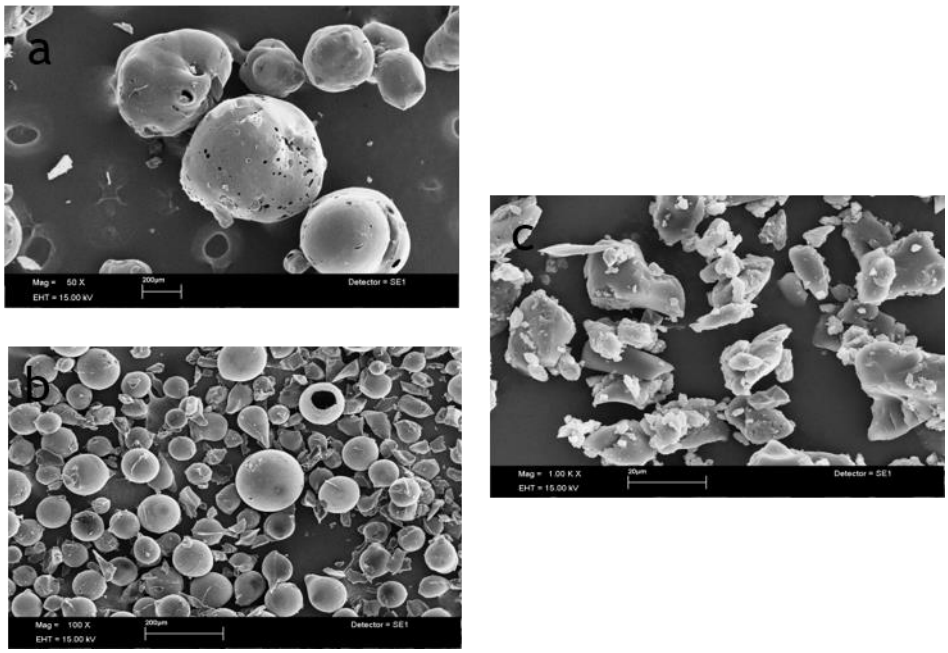

Figure 35: SEM of the C-βNs > 100 μm (a); C-βNs < 100 μm (b); C-βNs < 40 μm (c)

The particles of C-βNs < 40μm have a polyhedral shape whereas C-βNs > 100μm and C-βNs < 100μm is composed of almost homogeneously distributed, spherical particles (panels a-b) and it is interesting to note that these particles are not stuck to each other but are physically distinct. As described previously for the βNs, it is possible to suppose that this spherical morphology derived from a step of fluid phase before the carbonization. The surface tension during this stage drives to the formation of particles with spherical morphology. For the C-βNs < 40 μm. it is possible to image that this surface tension is not enough strong to lead the formation of spherical particles. However, it is interesting to note that all these particles are physically distinct probably due to the permeating volatiles that contributes to the separation of the single surface, voiding the sintering process.

The samples subjected to pyrolysis at 800°C were collected, and the specific surface area and the porosity were evaluated using the ASAP 2010. The specific surface area was evaluated with the Langmuir equation, while the porosity with the DFT method. The result is reported in table 19:

Sample	Surface Area	Micropore Volume	Pore Width
	($m^2\ g^{-1}$)	($cm^3\ g^{-1}$)	(Å)
βNs > 100 μm	565	0,143	6-15
βNs < 100 μm	544	0,141	5-17
βNs > 40 μm	550	0,118	6-13

Table 19: Physical properties of C-βNs > 100 μm; C-βNs < 100 μm; C-βNs < 40μm

Regarding the specific surface area and the porosity, it seems that the dimension of the starting material has no influence. It is very interesting, it is possible to tailor the dimension of the carbon materials without changing the physical characteristics.

3.1.12 Influence of the particle size on the final carbon from Lc

The LcNs, like the βNs, after the synthesis are subjected to a grinding process. The dimension of the final carbon for the samples depends on the size of the starting materials. For this reason, it was evaluated the possibility to modify the specific surface area changing the dimension of the Ns particle size.

For doing this the ball mill was applied and then sieved. The different size fractions obtained were:

- Over 100 μm
- Under 100 μm
- Under 40 μm

In Fig. 36 are reported the micrographs obtained for the three different parts collected using the SEM:

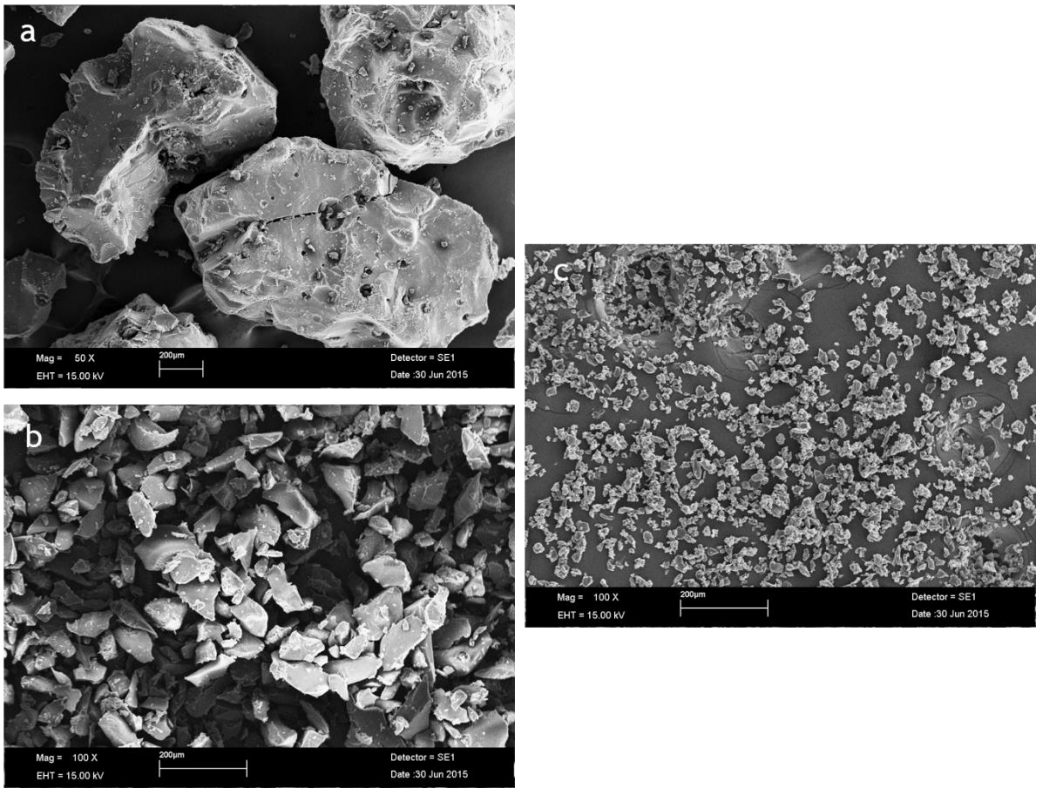

Figure 36: SEM micrographs of the Lc > 100 μm (a); Lc < 100 μm (b); Lc < 40μm (c)

The SEM confirms that the sieving process lead to have particle with the desire dimensions.

A TGA analysis of the samples was performed in order to determinate the yield of pyrolysis and for being sure that the dimension of the particles does not influence the pyrolysis process. The TGA was carried out in N_2 at 10°C min^{-1} to 800°C. The result obtained is reported in Fig. 37:

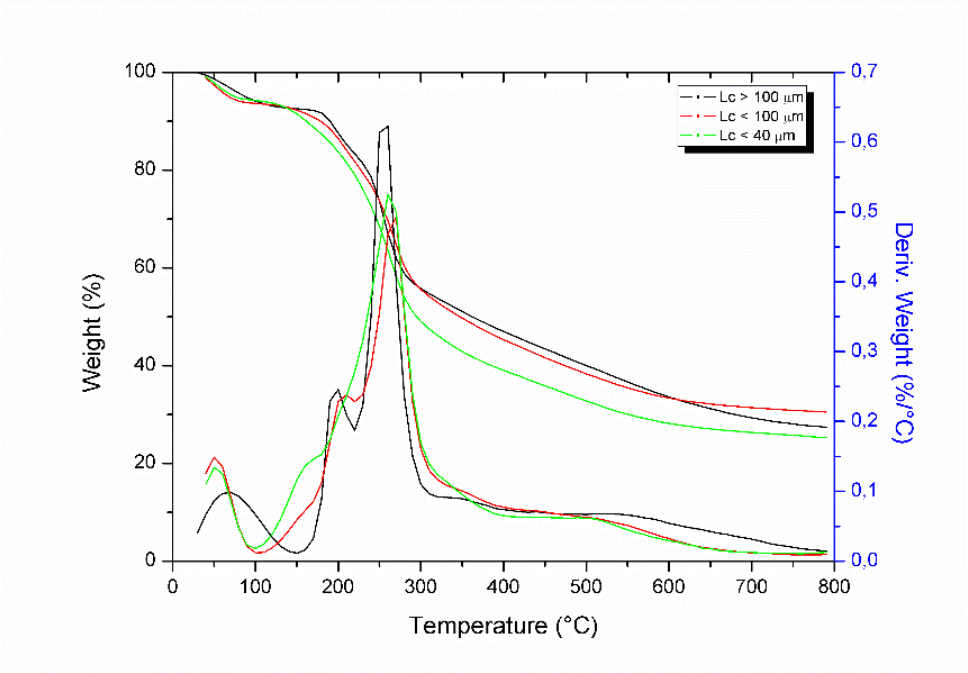

Figure 37: TGA of the Lc > 100 μm (black line); Lc < 100 μm (red line); Lc < 40μm (green line)

Decreasing the dimension of the particles there is a little shift to lower temperature (from 200°C to 210°C) of the main step of degradation. Is note that the dimension of the particles has an influence on the thermal behavior of a sample due to the difficult of the heat to penetrate large samples [118]. More interesting is that the sample that contain particle less large than 100 μm has the high amount of carbon at 800°C (30% respect to 27% for the sample over 100 μm and 25% pf the sample under 40 μm).

After the pyrolysis, the residue of the three samples was collected and the morphology and the dimensions were evaluated using the SEM. The micrographs were reported in Fig. 38:

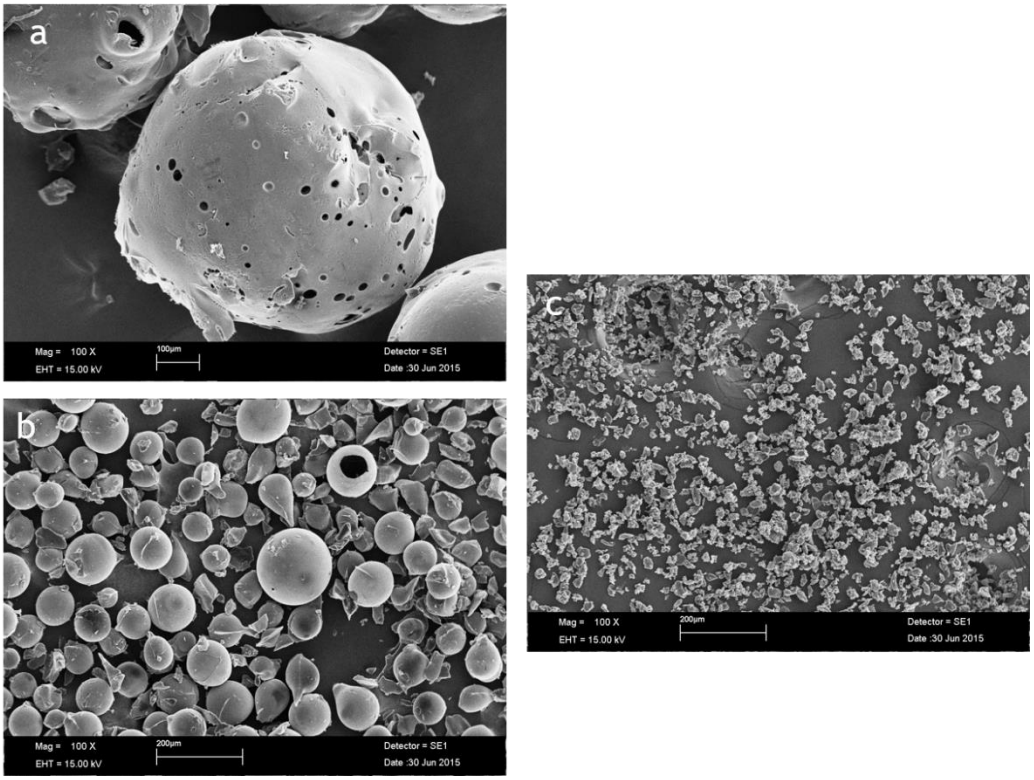

Figure 38: SEM micrographs of the C-Lc > 100 μm (a); C-Lc < 100 μm (b); C-Lc < 40μm (c)

The particles of C-Lc < 40μm have a polyhedral shape, as the C-βNs < 40μm. C-LcNs < 100μm and C-LcNs < 100μm are composed of almost homogeneously distributed, spherical particles (panels a-b) and it is interesting to note that these particles are not stuck to each other but are physically distinct.

As described previously for the βNs, it is possible to suppose that this spherical morphology derived from a step of fluid phase before the carbonization. The surface tension during this stage drives to the formation of particles with spherical morphology. For the C-LcNs < 40 μm, it is possible to image that this surface tension is not enough strong to lead the formation of spherical particles. However, it is interesting to note that all these particles are physically distinct probably due to the permeating volatiles that contributes to the separation of the single surface, voiding the sintering process.

The samples subjected to pyrolysis at 800°C were collected, and the specific surface area and the porosity were evaluated using the ASAP

2010. The specific surface area was evaluated with the Langmuir equation, while the porosity with the DFT method. The result is reported in table 20:

Sample	Surface Area	Micropore Volume	Pore Width
	($m^2\ g^{-1}$)	($cm^3\ g^{-1}$)	(Å)
βNs > 100 μm	559	0,15	5-12
βNs < 100 μm	474	0,04	4-11
βNs > 40 μm	195	0,05	6-12

Table 20: Physical properties of C-LcNs > 100 μm; C-LcNs < 100 μm; C-LcNs < 40μm

Regarding the specific surface area and the porosity, it seems that the dimension of the starting material has no influence when the dimension of the particles is high. The area decreases when the particle size is under 40 μm. It is strange, because usually the area of a small particle tends to be higher. Indeed, when a particle of a given volume is broken two parts total volume does not change, but the total surface area increases by the amount of the two new-exposed surfaces. Anyway, a surface is of a porous solid depends on many factors. For instance, the presence of roughness on the surface that can increase the specific surface area, or the presence of macropores and the density of the bulk [119]. The small dimension of the starting material, it is possible to suppose that during the pyrolysis the bulk density change, and so the obtained materials is more compacted decreasing the specific surface.

3.1.13 βNs blocks

After the classical synthesis of the bNs or LcNs, the block polymer was grounded in a mortar and then washed in a Buchner funnel with water and acetone. It was decided to not grinded the materials, in order to leave the block structure of the Ns and try to get a porous carbon materials with the same dimensions of the precursor. For this reason, the two Ns were not wash with water. Indeed, both the Ns are able to adsorb high quantity of water, swelling. The swelling causes the collapse of the block structure. Thus, the two blocks of Ns were only washed with acetone.

A piece of βNS-block, after the purification, was cut and subjected to a TGA analysis in order to evaluate the thermal behavior. Fig. 39 shows the thermogram obtained for the βNs-block and the βNS for making a comparison.

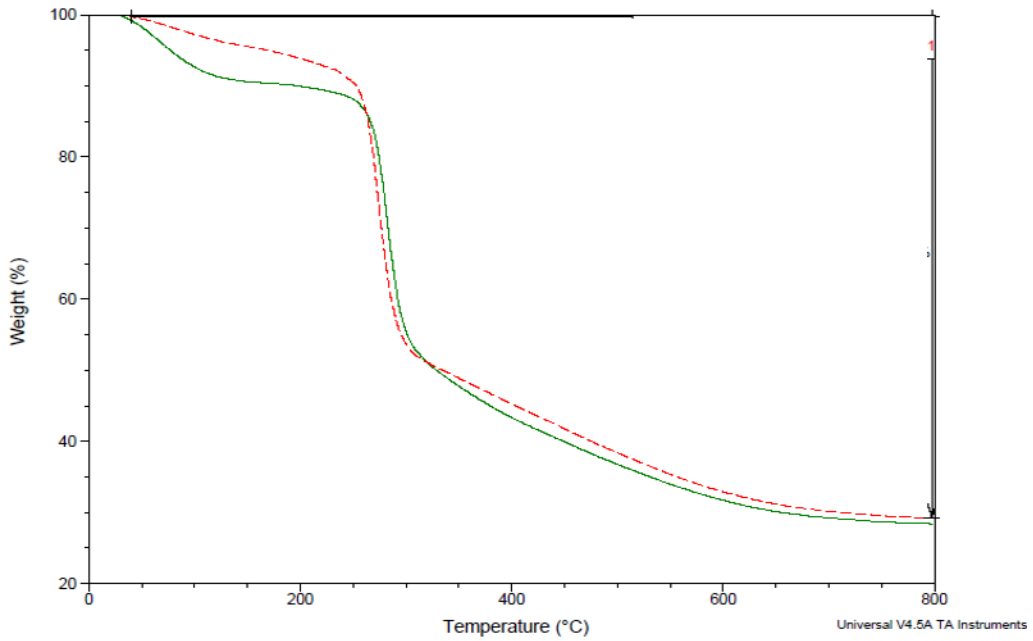

Figure 39: TGA of the βNs (red line) and the βNs-block (green line)

There are not particular differences in the two thermograms. Before 110°C, a greater step of water evaporation occurs and that indicates the block is wetter that the classical nanosponge. Probably, both the acetone

cannot penetrate perfectly inside the Ns and the large dimension of the sample avoid the quick evaporation of the water adsorbed after the purification.

For being sure that all the solvent (DMSO) was completely removed from the solid a C-H-N-S analysis were performed, analyzing the surface of the block and the bulk after 27 h of Soxhlet. The results are listed in table 21:

Sample	C	H	N	S
Outer βNS	50,15	6,38	2,95	0
Inner βNS	49,99	6,69	3,29	0

Table 21: C-H-N-S analysis

The quantity of Sulfur is almost zero, so the block of Ns can be considered completely purified.

The solid block was then subjected to a pyrolysis up to 800°C at 10°C min^{-1} in order to obtain a carbon material. Fig. 41 shows a piece of Ns in a combustion boat:

Figure 40: Piece of βNS-block

After the pyrolysis, the carbon obtained has the same shape and dimension of the starting-block. An image is reported in Fig. 42.

Figure 41: Piece of C-βNS-block

The block-pyrolyzed was then cut in order to obtain a piece with a weight of about 100 mg, suitable for the ASAP analysis. The specific surface area was evaluated with the Langmuir equation, while the porosity with the DFT method. The result is reported in table 22:

Sample	**Surface Area**	**Micropore Volume**	**Pore Width**
	($m^2\ g^{-1}$)	($cm^3\ g^{-1}$)	(Å)
βNs-block	610	0,174	5-11

Table 22: Physical properties of the βNs-block

Regarding the specific surface area and the porosity, it seems that the dimension of the starting material has no influence on the physical characteristics of the final porous carbon. It is very interesting because it is possible to tailor the dimension of the carbon materials, rendering it more handleably, without changing the physical characteristics.

3.1.14 **Lc block**

It was decided again to not grinded the LcNs after the synthesis, in order to leave the block structure of the Ns and try to get a porous carbon material with the same dimensions of the precursor. For this reason Ns was not wash with water for the same reasons explained for the βNS-block.

A piece of LcNs-block, after the purification for 27h in Soxhlet, was cut and subjected to a TGA analysis in order to evaluate the thermal behavior. Fig. 43 shows the thermogram obtained for the Lc-block and the LcNs for making a comparison.

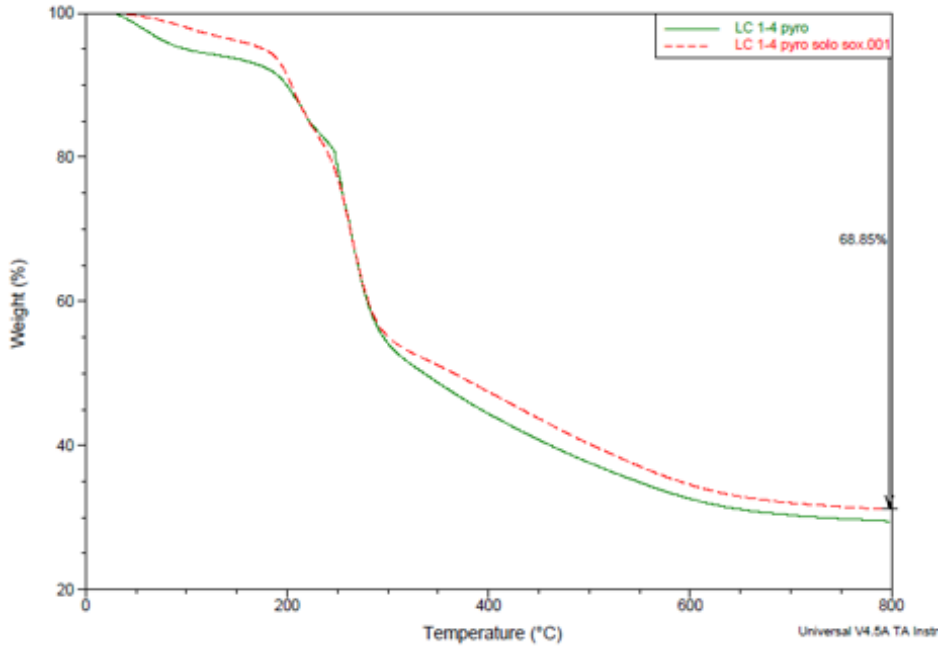

Figure 42: TGA of the LcNs (red line) and the LcNs-block (green line)

There are not particular differences in the two thermograms. Before 110°C, a greater step of water evaporation occurs for the LcNs-block and that indicates the block is wetter that the classical nanosponge, as shown for the βNS-block.

For being sure that all the solvent (DMSO) was completely removed from the solid a C-H-N-S analysis were performed, analyzing the surface of the block and the bulk after 27 h of Soxhlet. The results are listed in table 23:

Sample	C	H	N	S
Outer LcNs	51,60	7,14	3,35	0
Inner LcNs	50,05	6,64	3,16	0

Table 23: C-H-N-S analysis

The quantity of Sulfur is almost zero, so the block of Ns can be considered completely purified.

The solid block was then subjected to a pyrolysis up to 800°C at 10°C min^{-1} in order to obtain a carbon material. After the pyrolysis, the carbon obtained has the same shape and dimension of the starting-block. An image is reported in Fig. 44.

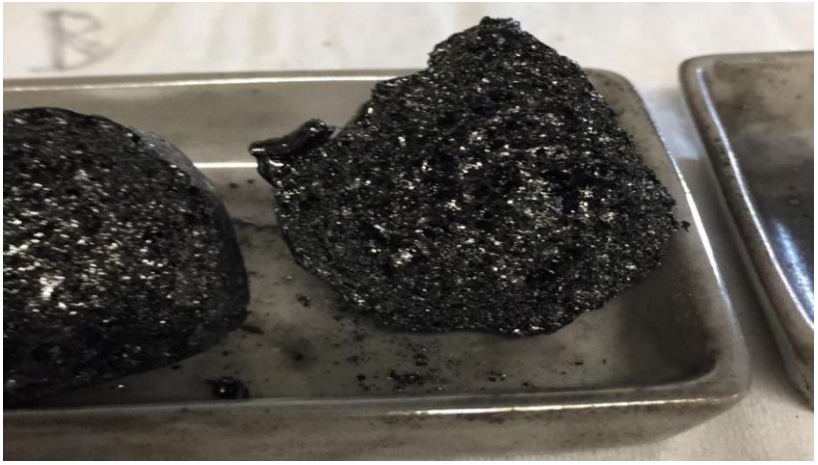

Figure 43: Piece of C-LcNs-block

The block-pyrolyzed was then cut in order to obtain a piece with a weight of about 100 mg, suitable for the ASAP analysis. The specific surface area was evaluated with the Langmuir equation, while the porosity with the DFT method. The result is reported in table 24:

Sample	Surface Area	Micropore Volume	Pore Width
	($m^2\ g^{-1}$)	($cm^3\ g^{-1}$)	(Å)
βNs-block	490	0,11	5-15

Table 24: Physical properties of the βNs-block

A shown for the βNS, it is possible to tailor the dimension of the carbon materials, rendering it more handleably, without changing the physical characteristics.

3.2 GAS ADSORPTION APPLICATIONS

In this part of the thesis, the possibility to use the C-βNS and C-LcNS as adsorbent materials for the PSA process. Some thermodynamic parameters were investigated in order to evaluate the type of adsorption for a future industrial application**.**

3.2.1 Microcalorimetric studies on C-βNS and C-LcNS

The energetic study of the adsorption process of a gas is an important step to understand the behavior of an absorbent in cyclical processes of separation of gas mixtures. The knowledge about the heat of adsorption is very important in the description of gas-solid interaction and it is a good tool for describe the properties of a surface. For this type of analysis, the microcalorimeter was applied and it allows to determinate not only the heat of adsorption developed during the adsorption, but also the quantity of gas-adsorbed. Indeed, the microcalorimeter is equipped with a gas-volumetric system in order to evaluate the quantity of gas adsorbed during the measure. It allows to build the adsorption isotherms and so it is possible to evaluate the reversibility of the adsorption process. In other words, appropriate doses of gas are admitted onto the adsorbent and each dose is left to reach the equilibrium. The heat and the pressure at the equilibrium point is recorded til the first adsorption run is performed. Then, the system is evacuated and then a second run with the similar doses used

for the first is did. If the first and the second runs are overlapped, it is possible to conclude that the gas-adsorption is reversible. On the contrary, the process is irreversible, because some dose of gas is left entrapped inside the sample. Thus, form the elaboration of the raw data recorded during the adsorption it is possible to build the adsorption isotherms. Furthermore, the instrument annotates the heat developed for each dose of gas sent on the sample. From the elaboration of that value, it is possible to obtain the isosteric heat of adsorption (q). It can be defined as the difference between the activation energy of adsorption and desorption, which represents the strength of adsorbent– adsorbate interactions.
The evaluation of this data was carried out using different gases, such as CO_2, CO, N_2 and O_2. It was found out the both the carbons were able to adsorb only the CO_2 and so the study was then focused only on the adsorption of CO_2. Moreover, some adsorptions of water were carried out, in order to evaluate the hydrophobicity of the samples.
In Fig. 44 are reported the two CO_2 adsorption isotherms of the C-βNs and C-LcNs performed at 30°C.

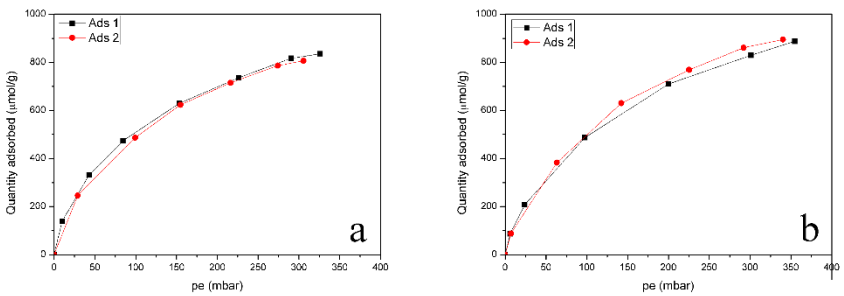

Figure 44: CO_2 adsorption isotherms at 30°C performed for C-βNs (a) and C-LcNs (b).

Fig. 44 a and b shows the two CO_2 adsorption isotherm obtained for the C-βNS and C-LcNS. As it is evident, the first isotherm and the second isotherm were overlapped, hence the adsorption of the CO_2 is reversible. Moreover, it is possible to see that the adsorptions do not reach the plateau, so the carbons are able to entrap more CO_2 increasing the pressure. However, the maximum adsorption for the C-βCD is 835 μmol g^{-1} whereas for the C-LcNS is 895 μmol g^{-1} at c.a. 350 mbar.

The microcalorimeter allows to direct determinate the heat develops during the adsorption. Thus, it is possible to evaluate the Differential heat of adsorption, Qdiff, that is obtained by the direct calorimetric Q values by carrying out the operation specified in this equation:

$$Qdiff = (\delta Q/\delta n_a)_{A,T} \qquad [4]$$

Where Q depends on some parameters of the instrument, n_a is the amount of carbon dioxide adsorbed at fixed temperature, A is the specific surface area of the sample and T is the temperature of the measure.
Interestingly, it is possible to plot the differential heat of adsorption vs the coverage. This plot allows to determinate the site energy distribution. The initial heat value (q_0), corresponding to the highest energy of interaction of the CO_2 with the strongest sites, was evaluated by extrapolating the heat when the coverage is 0. Fig. 45 shows the results obtained for the two samples:

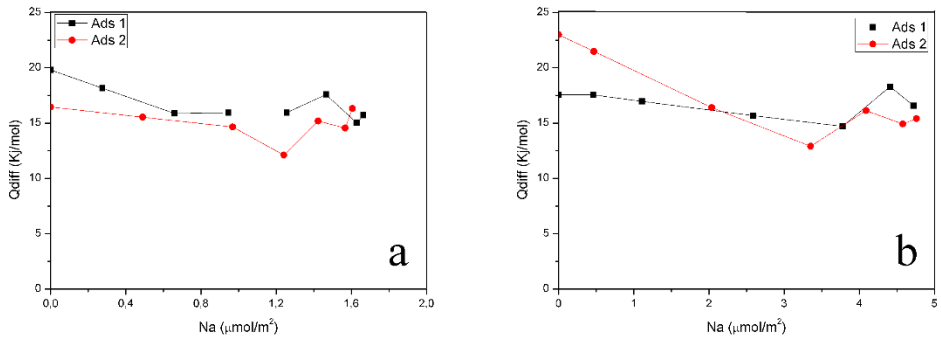

Figure 45: Qdiff vs Na plot for C-βNs (a) and C-LcNs (b)

For the C-βNS primary adsorption we estimated q_0 of 19,79 kJ mol^{-1} for the second 15,75 kJ mol^{-1}. For the C-LcNS primary adsorption we estimated q_0 of 15,73 kJ mol^{-1} for the second 22,99 kJ mol^{-1}. These values show that the adsorption on these materials could be considered like a physisorption. These results are important because the interaction between the CO_2 and the surface is not strong in order of the chemical

bond, which would facilitate the regeneration of the carbons in an industrial application [120]. Furthermore, the heats of adsorption have been considered as an indicator of the heterogeneity of the surface. In the case of the C-βNS and C-LcNS, the heat of adsorption for both the samples do not change during the adsorption, hence all the sites of the surface are homogeneous. Indeed, it is possible to see from the two graphs in Fig. 45, that the Qdiff it is not depended on the amount of adsorbate. Energetic heterogeneity of the surface of an adsorbent depends on the distribution of micro- and mesopore and also on the shape and size of them [121]. In the case of the two carbons exanimated, it is possible to affirm that the porosity of the systems is well-defined and distributed and all the pore have relatively the same dimension and shape.
The hydrophilicity or hydrophobicity of a solid is important to know for a large number of applications. To evaluate the hydrophilicity/ hydrophobicity of the surface the evolution of the heat adsorption of water vapor with the coverage has been studied using the microcalorimeter. The results obtain are shown in Fig. 46.

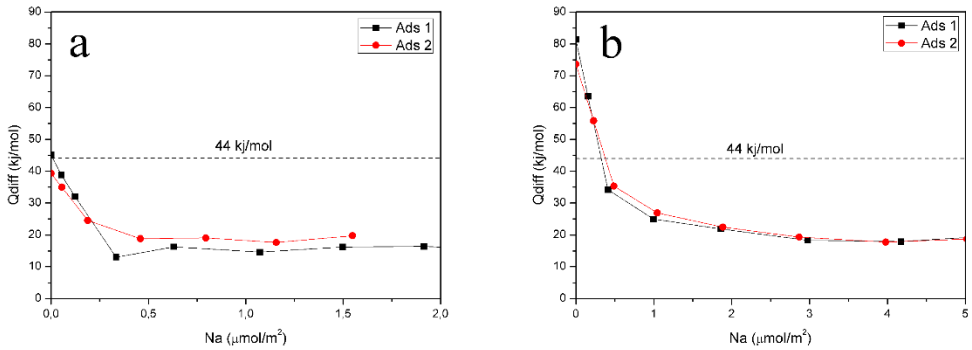

Figure 46: Qdiff vs Na plot of H_2O for C-βNs (a) and C-LcNs (b)

Fig. 46 shows the heat of adsorption for water as a function of amount adsorbed on C-βNS (a) and C-LcNS (b). The horizontal dashed line corresponds to the heat of condensation of water that is 44 kJ mol^{-1}. The adsorption for both the samples is less than 370 kJ mol^{-1} and so it is possible to affirm that the water is not chemically bonded [122]. Moreover,

the differential heat of adsorption could be compared with the latent heat of liquefaction of water and any site interacting with water with an energy higher than 44 KJ mol^{-1} is hydrophilic. The carbons obtained by nanosponges exhibited some hydrophilic sites, which are filled up first. Then, the heat of adsorption fell below the latent heat of liquefaction for both the samples, hence the surface has many hydrophobic sites.

3.2.2 **Microgravimetric studies on C-βNS and C-LcNS**

The microbalance was used for testing the ability of the materials in the capture of carbon dioxide at different temperature, form 30°C to 120°C. The pressure range used for the analysis is form 0 bar to 20 bar. A previous purification of the samples was made, outgassing and keeping the samples at 300°C overnight in order to eliminate any adsorbed impurities. The series of volumetric isotherms performed for the C-βNS and C-LcNS are reported in Fig. 47:

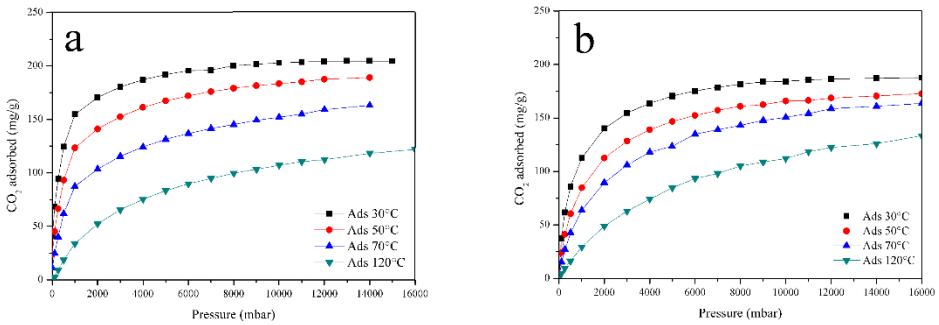

Figure 47: CO_2 adsorption isotherms on C-βNs (a) and C-LcNs (b).

Fig. 47 shows the isotherms obtained at 30°C, 50°C, 70°C and 120°C for the C-βNS (a) and C-LcNS (b). The adsorption experiments were repeated twice in order to evaluate the presence of irreversible adsorption, namely CO_2 not removed after an overnight outgassing at work temperature. The maximum adsorption at 30°C is 204 mg g^{-1} for C-βNS and it becomes half when the adsorption is leaded at 120°C. for the C-LcNs the adsorption at 30°C is 187 mg g^{-1} whereas at 120°C is about 133 mg g^{-1}. It is very encouraging to find out that at 120°C our carbons are still able to adsorb CO_2.

From these type of analysis, it is possible to obtain thermodynamic parameters.

3.2.3 **Evaluation of thermodynamic parameters**

For evaluating the thermodynamic parameters, the isotherms from each carbon experimental plot were used. On the basis of these experimental data, the $\Delta H°$ value can be calculated by using the Clasius-Clapeyron equation. In general, the same consideration made for the microcalorimetric technique can be done. Basically, the value of - $\Delta H°$ lower than 40 kJ mol^{-1} indicates physisorption whereas larger than 80 kJ mol^{-1} can indicate strong chemisorption. Moreover, Langmuir equation has been used for evaluating the adsorption/desorption constant K. The linear fitting of the Langmuir equation p/n vs p provides an intercept that can be used for the K. Then, using the fundamental thermodynamic equation, $\Delta G°$ and $\Delta S°$ can be calculated from the known K and $\Delta H°$. Thus, the obtained thermodynamic parameters can be used for characterizing the materials. Three randomly horizontal lines were drawn. As long as the horizontal line crosses with the isotherms, the intersects point must feature the same quantity of adsorbed molecules, basically the identical fractional coverage, θ. In Fig. 48 are reported the isotherms performed at 30°C, 50°C and 70°C and the selected coverage used for C-βNS (a) and C-LcNS (b).

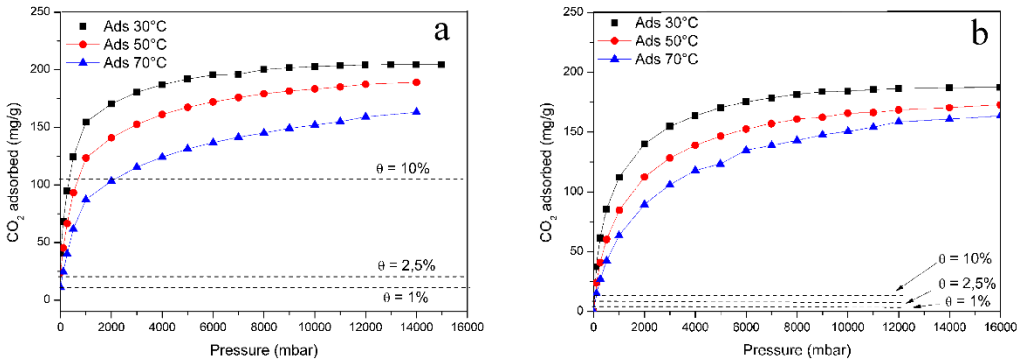

Figure 48: Isotherms plots and coverage of the C-βNs (a) and C-LcNs (b)

The percentage of coverage chosen for the analysis are 1%, 2,5% and 10% for both the samples, as shown in Fig. 30. On the basis of the Clausis – Clapeyron equation (5), the coordinate data of the three points can be used for evaluating the ΔH°, plotting lnp vs 1/T of the three isotherms at the same value of θ. The results of the fitting for C-βNS and C-LcNS are reported in figure 49.

$$\left(\frac{\delta \ln p}{\partial T}\right)_{\theta} = -\frac{\partial H^{o}}{RT^{2}} \qquad (5)$$

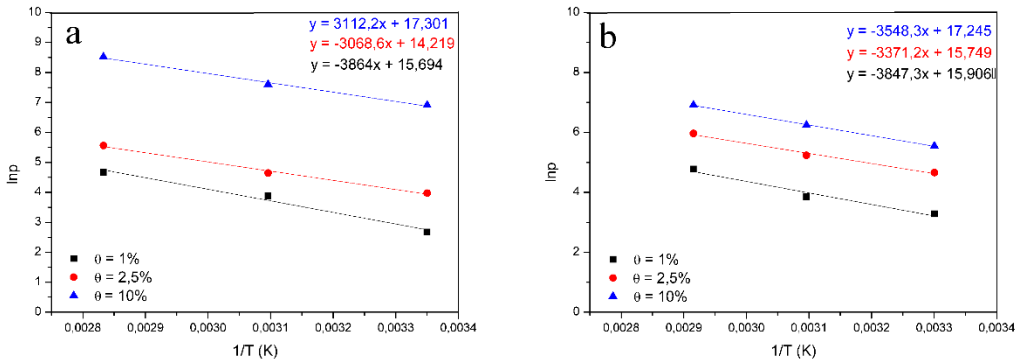

Figure 49: Linear plot of 1/T vs lnp for C-βNs (a) and for C-LcNs (b)

The ΔH° can be evaluated form the linear fit for each coverage multiplying the slope by the constant R (8,314472 J mol^{-1}). In table 25 are reported for the two carbons the values of ΔH° obtained for the different θ.

Sample	ΔH° at θ= 1%	ΔH° at θ= 2,5%	ΔH° at θ= 10%
C-βNs	-32 Kj/mol	-26 kj/mol	-30 Kj/mol
C-LcNs	-32 kj/mol	-27 kj/mol	-30 kj/mol

Table 25: AH° evaluated at different coverage for the C-βNS and C-LcNS

On the basis of the ΔH° value the adsorption on the two carbons seems to be physical and so a weak physisorption. These results have been confirmed by the direct measure of the isosteric heat of adsorption using the microcalorimeter. The values of q° recorded with the microcalorimeter were for the C-βNS 19,79 kJ mol^{-1}, whereas for the C-LcNS 15,73 kJ mol^{-1}. The values obtained using the calorimetric technique exceed respect the ones got with the Clasius-Clapeyron equation. This behavior is associated with the fact that in the adsorption calorimetry, simultaneous measurement of the heat generated at each point of the isotherm is recorded making this a technique more accurate for the energetic study of adsorption process of a gas. Anyway, with the ΔH° value, it is possible to calculate more thermodynamic parameters. Starting from the shape of the isotherms obtained for the two samples, it is possible to speculate that the CO_2 tends to be monolayer adsorbed which is in accordance with the Langmuir adsorption theory. It is so possible to convert the isotherms in a plot p/n vs p taking into account the Langmuir equation. This study allows to determinate the adsorption/desorption equilibrium constant, K. In Fig. 50 are reported the two Langmuir linear fitting for the C-βNS (a) and C-LcNS (b) based on the isotherms carried out at 30°C:

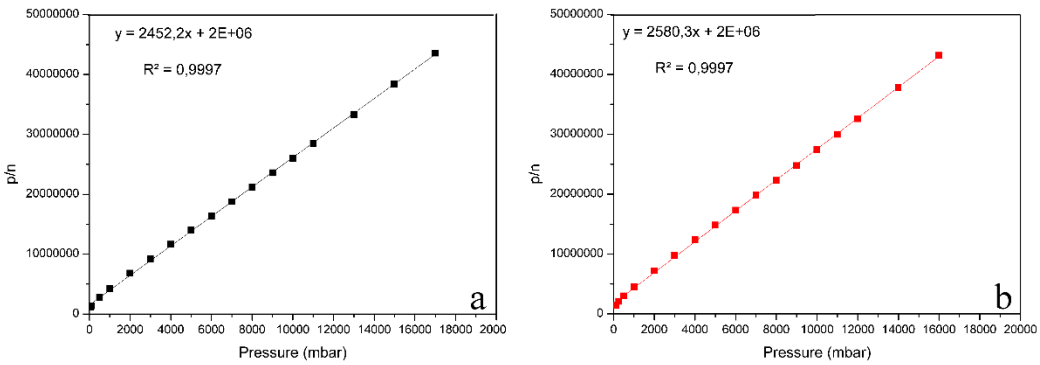

Figure 50: Linear fit for the C-βNs (a) and C-LcNs (b)

According to the coverage fraction θ that can be expressed as:

$$\theta = \frac{K}{1+K} \tag{6}$$

Since q is a fraction of the amount of CO_2 (n expressed in mol) that can complete coverage the surface of the sample (n_∞), the equation (5) can be written as:

$$\frac{p}{n} = \frac{p}{n_\infty} + (kn_\infty)^{-1} \tag{7}$$

And so, it is possible to value the for the C-βNs that is $4{,}90 \times 10^9$, while for the C-LcNs is $4{,}49 \times 10^9$. Once obtained the equilibrium constant K for a certain temperature, it is possible to value the ΔG° of the adsorption reaction from the relation:

$$\Delta G^0 = -RT \ln K \tag{8}$$

Thereafter, it can be calculated the ΔS° from:

$$AG^0 = \Delta H^0 - T\Delta S^0 \tag{9}$$

Therefore, the thermodynamic parameters obtained are listed in table 26:

Sample	ΔG°	ΔH°	ΔS°
C-βNs	-56 kj/mol	-19 kj/mol	0,25 kj/K
C-LcNs	-56 kj/mol	-22 kj/mol	0,26 kj/K

Table 26: Thermodynamic parameters evaluated for the two samples

These values support the view that the surface of the two carbons have an affinity for the CO_2. The enthalpy values show that the adsorption process is exothermic whereas the ΔG° indicates that the adsorption of

the carbon dioxide onto the surface of the carbons is spontaneous ($\Delta G°<0$). The entropy values are positive ($\Delta S°>0$) confirming the spontaneously of the process.

3.2.4 **Temperature Programmed desorption study**

This measurement was carried out in collaboration with Politecnico di Milano.

Temperature controlled desorption (TPD) can be described as the measurement of the rate of desorption of adsorbed molecules, as a function of temperature. Therefore, this method can be useful in the extraction of very important information. It can be used in the identification and characterization of sites active in adsorption and catalytic reactions, in the study of adsorption states, binding energies, surface concentration and desorption kinetics.

In these TPD experiments, six gases are adsorbed at the surface, at 50°C after a preliminary outgassing at 300°C in order to remove all the species that be adsorbed on the surface of C-LcNs, such as water. Then, desorption of adsorbate is monitored while increasing the solid sample temperature in a controlled fashion till 300°C. The first gas adsorbed were C_3H_6 and the result obtained is reported in Fig 51.

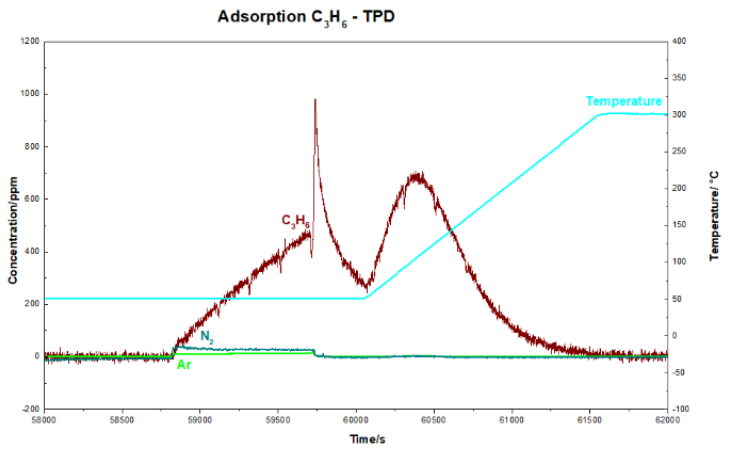

Figure 51: TPD analysis on C-LcNs using C_3H_6

The data shown in Fig. 51 are presented as variation of concentration of gas (y axis) as a function of time (x axis) and temperature (y_2 axis). Thus, the red line designates the trend of the gas analyzed in function of temperature and times. It is important to point out that this is a flow system, so the gas-flow has to be controlled and constant in time. For this reason, the signal intensity of the gas-carries is monitored, as shown by the two lines in Fig. 51, cyan and green, respectively. Afterwards, form Fig. 51, following the red profile, it is possible to see a "bell-profile". It indicates that when the sample is exposed to 1000 ppm C_3H_6, the gas is adsorbed by the sample and then the quantity of gas that was adsorbed is desorbed by heating the C-LcNs. This TPD profile, can reveals some information. Firstly, it is seen that C_3H_6 can be adsorbed by C-LcNs, and so it is possible to use it in some industrial application. Indeed, it is a novel study the possibility to use porous carbon for the separation of the propylene form the propane [123]. The splitting of propane-propylene is one major challenges in separation technology. The system involve the separation of two molecules with very similar properties [71]. Much of the literature published [123] in this area was devoted to adsorbent characterization. Most of the work dealt with zeolites [124] and only a few dealt with carbonaceous materials because they usually shown a poor affinity toward propylene [125] . For example, Padin et al. found that some CMS (Bergbau-Forschung) did not adsorb either propane or propylene [126].

Conversely, from the TPD data seems that C-LcNs has an affinity toward the C_3H_6, so it is possible to image to use it for the separation of propylene from methane in a gas mixture in PSA process.

In the end for the data shown, the maximum of TPD profile is located at RT, meaning that the adsorption phenomena is a physisorption [127]. So it is possible to image for an future industrial application a simple restrore of the carbonaceous material after use.

Fig. 52 shown the results obtained after the adsorption/desorption of hydrogen on the C-LcNs:

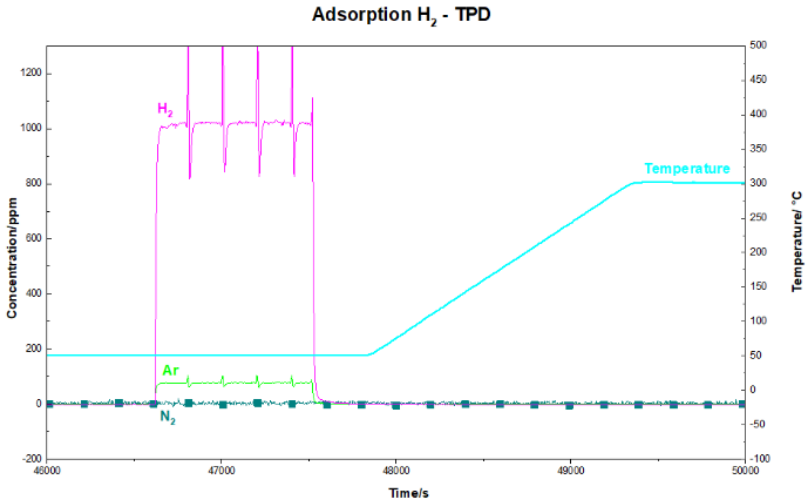

Figure 52: TPD analysis on C-LcNs using H_2

Following the pink line, it is possible to see that the C-LcNs are not able to adsorb the H_2. Indeed, after the inlet of 1000 ppm onto the reactor, the amount of gas remains constant during the time. When the outgas is applied, the quantity of hydrogen decreases rapidly, testifying that there is not interaction between the surface of the sample and the gas.

Fig 53 shows the results obtained after the adsorption/desorption of CO on the C-LcNs:

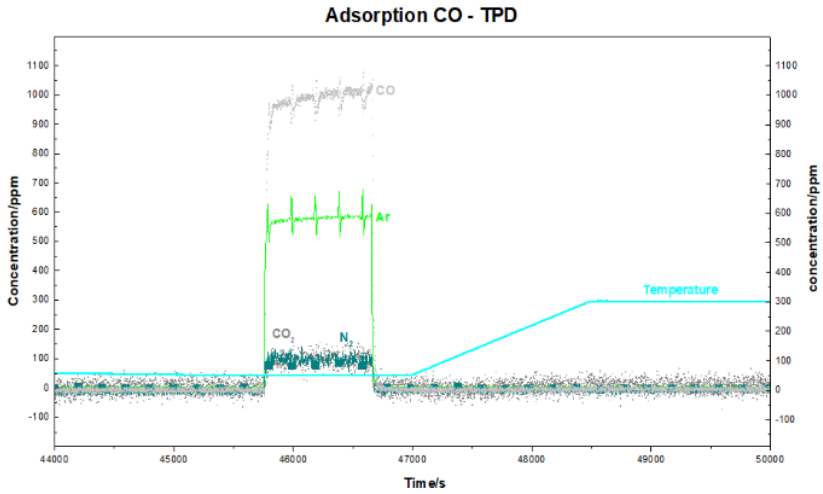

Figure 53: TPD analysis on C-LcNs using CO

In Fig. 53 it is possible to see that there is a grey line that represents the trend of the CO_2 during the experiment. It was monitored because it is not easy to separate completely the CO_2 form the CO, so a certain amount of CO_2 is still present during the analysis. Anyway, the light grey line characterizes the adsorption/desorption of the carbon monoxide. The shape of it, underlines that there is not an interaction between the C-LcNs and the CO, so the CO is not adsorbed by the carbon.

Fig. 54 shows the TPD analysis carried out using the ammonia:

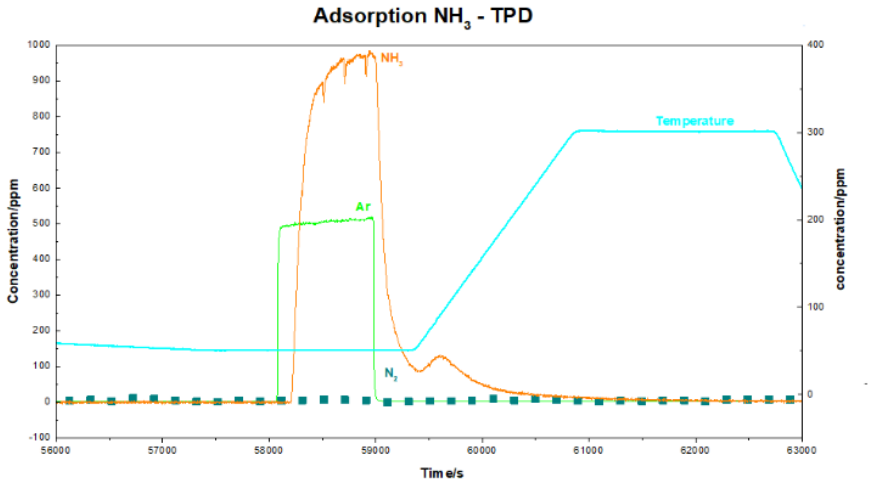

Figure 54: TPD analysis on C-LcNs using NH_3

The trend of the ammonia suggests that this gas is not adsorbed by the C-LcNs. Indeed, after admitting the NH3 into the reactor, the amount of ammonia does not change during the analysis. When the desorption process starts, the ammonia is outgassed very quick proving that the NH_3 has not affinity towards the substrate.

Fig. 55 depicts the adsorption/desorption measurement of on C-LcNs:

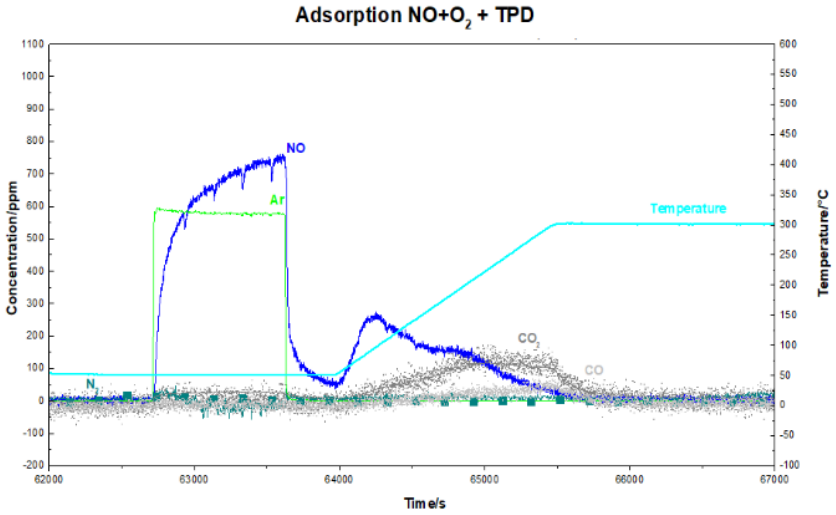

Figure 55: TPD analysis on C-LcNs using NO

The NO is not adsorbed by the C-LcNs. After the admittance of 1000 ppm of NO, the quantity of it does not change during the analysis and it is, again, rapidly removed. The presence of the other gases in the analysis, such as CO, CO_2 and N_2 can be attributed to the fact that the NO gas used for the measurement is not pure.

Fig. 56 represents the TPD performed on the C-LcNs using the CO_2:

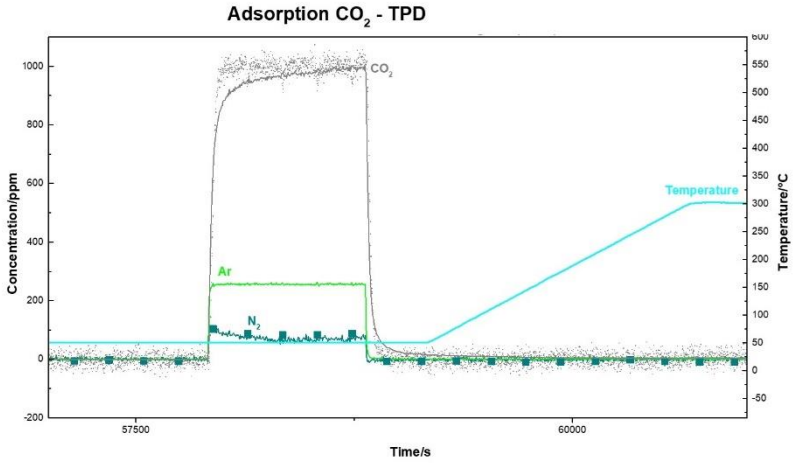

Figure 56: TPD analysis on C-LcNs using CO_2

Form the trend of the adsorption/desorption of CO_2 shown in Fig. 56, it is possible to conclude that the CO_2 can not be adsorbed by the C-LcNs. This data seems to be in contrast with all the analysis performed and widely explained previously. These different results can be clarified taking in account two facts. First of all, different method can give different results. The microbalance and the microcalorimeter are two powerful technique but they work at higher pressure respect to the reactor of the TPD. The admittance of 1000 ppm of gas in TPD correspond to a CO_2 pressure of 0,06 bar that is a very low-pressure respect to the one used for the other to analyzes. For better understand this, the following equilibrium roughly represents what goes on during physisorption of a gas onto a surface.

Gas+Surface ⇄ adsorption/desorption Gas−−Surface

The effect of pressure can be understood on the basis of Le Chatelier's principle, which states that if a stress (such as a change in pressure) is applied to a system in equilibrium, the equilibrium will shift so as to tend to counteract the effect of the constraint. In this case, increasing the pressure, the system would respond by wanting to reduce the number of gas phase molecules. More gas molecules are present in the gas phase more molecules are immobilized on the surface. Thus, the pressure used for the TPD analysis is not enough for underline the adsorption phenomenon. It is important to know that the adsorption is influenced by many parameters and not only the different of pressure. The adsorption is a very complicated phenomenon in which many parameters can play an important role. For instance, the adsorption is strongly dependent on the temperature used for the measurement. It is noted [128] that the increasing of temperature reduces the adsorption. In our case, it was demonstrated with the microbalance that the carbon dioxide can be adsorbed on the C-LcNs even at higher temperature, higher than the 50°C used for the TPD. Consequently, it is possible to exclude this parameter as the cause of the different results. Another important parameter that has an effect on the adsorption is the time. Each gas-substrate system an adequate time for reach the equilibrium. If the admittance or the outlet of gas is faster than the time required for the equilibrium, the adsorption phenomenon can be overestimated or underestimated [128] . For all the analysis, this parameter

can be excluded: in all the measurements, for the adsorption and the desorption, it has been leaved enough time for reaching the equilibrium.

In conclusion, the different working pressure is the responsible of the different results. Obviously, if there is not interaction between the surface of a substrate and a gas, the adsorption phenomenon does not take place, even at high pressure. Indeed, using the TPD, it was found out that the C-LcNs is not able to adsorb the hydrogen. The same result was obtained using the microbalance admitting hydrogen pressure in a range of 0-20 bar.

3.3 LI-S BATTERIES

This part was performed in collaboration with Usman Zubair, Mojtaba Alidoost, Julia Amici, Carlotta Francia, Silvia Bodoardo e Nerino of Politecnico di Torino.

First of all, using the FESEM it was possible to have an image of the C-βNS after the impregnation with Sulfur, the melting with sulfur and after the wrapping with the rGO. The micrographs of them are reported in Fig. 57:

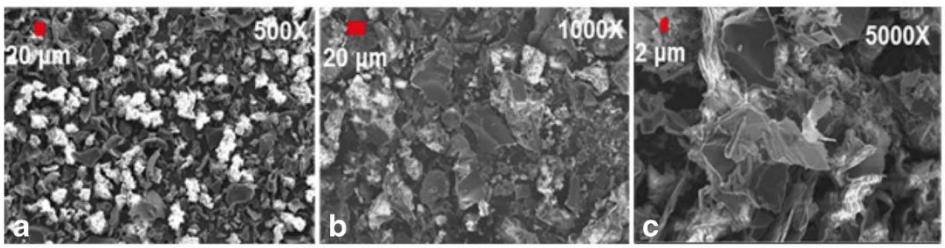

Figure 57: FESEM of C-βNS_SI, C-βNS_MI, and C-βNS_MI_rGO

The Sulphur in Fig. 57 a appears in light grain and seems to be homogeneously distributed on the surface of the C- βNS. The microporous structure of the carbons is not suitable for accommodate inside the pores the structure of the S_8. The structure of S_8 is shown in Fig 58.
The microporous structure of the carbons is not suitable for accommodate inside the pores the structure of the S_8.

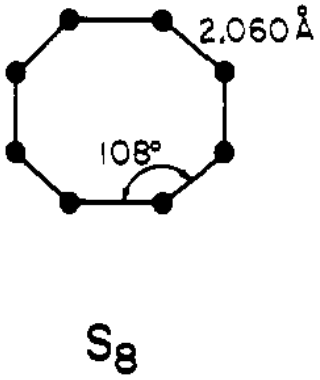

Figure 58: Hypothetical structure of S_8 [129]

S_8 crystals mostly occur in either orthorhombic α-Sulphur form with one S_8 molecules within unit cell or monoclinic β-Sulphur with six S_8 molecules. Fig. 57 b shows a very low quantity of Sulphur in the surface. The melting point of the S is 115°C, but the thermal treatment conducted on the C-βNS_MI at 155°C could have started the degradation of the S into lower molecular metastable allotropes such as S_2, S_3 S_4 and S_6 [129] that can penetrate inside the pores of the C-βNS. Fig. 57 c shows the C-βNS_MI_rGO. It is possible to observe the typical planar structure of the graphene sheets distributed randomly forming a disordered system. Anyway, the particles are very well wrapped by the rGO.
The SEM-EDS elemental mapping were performed in order to unveil the presence of Sulphur onto the carbon matrix. In all the samples, the S can be detected as diffused in the structure, but in very low quantity in the voids of the surface. Regarding the sample wrapped with the rGO, the Sulphur seem to be spread in the network that can indicate that the S is both on the surface of the carbon and wrapped itself in the rGO sheets.

For have an analytical determination of the quantity of S contained inside the samples, an elemental analysis was carried out for the 3 Sulphur-containing carbons and on the pristine C-βNS. The results obtained are reported in table 27:

Samples	%C	%H	%N	%S	$\%O_{calculated}$
C-βNS	78	0,69	1,26	0	20,05
C-βNS_SI	37	0,34	0,65	63	0
C-βNS_MI	40	0,26	0,81	59	0
C-βNS_MI_rGO	46	0,83	0,59	49	3,58

Table 27: C-H-N-S analysis on C-βNS, C-βNS_SI, C-βNS_MI and C-βNS_MI_rGO

The quantity of Sulphur in the pristine C-βNS is almost 0, so the S contained in the other samples comes from the treatment done. The elemental analysis of the C-βNS_SI, C-βNS_MI and C-βNS_MI_rGO revealed a sulfur amount around 63%, 59% and 49%, respectively.

For investigating if the S is inside the carbon matrix of the samples, the nitrogen adsorption-desorption analysis was carried out. As exposed previously, the bare C-βNS shows a type 1 isotherm (microporous material) with a specific surface area of 560 $m^2\ g^{-1}$, a pore volume of 0,05 $cm^3\ g^{-1}$ and a pore size about 5-11 Å. All the Sulphur- containing samples showed a very poor adsorption behavior. C-βNS_SI, C-βNS_MI and C-βNS_MI_rGO have a specific surface area of about 11, 17 and 12 $m^2\ g^{-1}$, respectively. This significant decrease of the specific surface area could indicate that the S is embedded inside the carbon matrix. It is possible to suppose that the S during the various treatment could penetrate inside the micropore, filling them. Indeed, even the FESEM analysis reveals that the surface of the carbons was completely covered by the S. It is not improbable that it can be loaded on the surface, closing the pores and causing the dramatically reducing of the specific surface area.

Fig. 59 shows the XRD patterns obtained for Sulphur, C-βNS, C-βNS_SI, C-βNS_MI and C-βNS_MI_rGO.

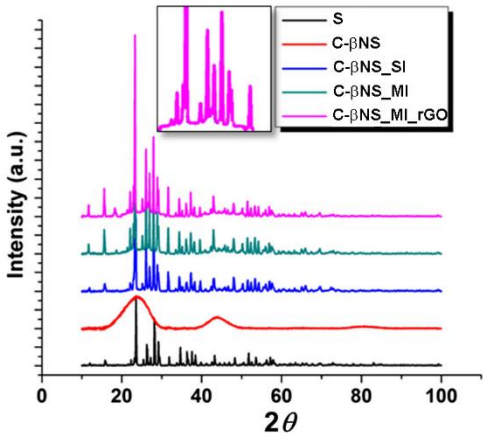

Figure 59: XRD of Sulphur, C-βNS, C-βNS_SI, C-βNS_MI and C-βNS_MI_rGO.

The sharp diffraction peaks denote that Sulphur exists in a crystalline state, while the broad diffraction around 24° in the C-βNS pattern indicates the amorphous characteristic of carbon spheres. It can be highlighted that XRD pattern for C-βNS_SI seems to be similar to the patterns showed by pristine Sulphur. Conversely, C-βNS_MI and C-βNS_MI_rGO showed the amorphous peak showed by the C-βNS and the Sulphur peaks that illustrate that most of the Sulphur is now diffused into micropores of the carbon material.

Moving to the electrochemical measurement, as observable in Fig. 59 a, the first discharge capacity at 0,1C of C-βNS_SI cathode is about 510 mA h g^{-1}. The characteristic two plateaus of discharge are well distinguishable, and the cathode retains only about 60% of the initial discharge capacity at the second discharge. This behavior can be ascribed to Sulphur that is on the surface of C-βNS, which promptly dissolves into electrolyte, generating polysulphides. For C-βNS_MI, two plateaus at 2,3 and 2,1 V are present, as shown in Fig. 59 b. The first can be ascribed to the reaction from S_8 to S_4^{2-}, due to cyclo-S_8 located on the carbon surface. The second derives from conversion of S_2^{-4}, that it is possible inside the micropores, increasing the capacity retention. The initial discharge capacity of C-βNS_MI is 842 mA h g^{-1} and the second is 610 mA h g^{-1} at 0,1 C, testifying that the Sulphur is well-distributed inside the micropores.

Moreover, the potential plateau at 2,3 V, corresponding with Li^+/Li, is still present after the first cycles, further proving that the Sulphur is in the pore structure. The C-βNS_MI_rGO (Fig. 59 c) shows excellent electrochemical properties due to the conductive network of the graphene that is able to put in contact the S particles. However, polysulphides formed during discharge can still readily diffuse out of graphene sheets generating the "shuttle" effects. Indeed, it is possible to see that the performance of C-βNS_MI_rGO has at first discharge capacity of 1103 mA h g^{-1}. On the second cycle, the discharge capacity decreases to 897 mA h g^{-1}, with capacity retention of 81% after SEI layer formation. At the fifth cycle at 0,1 C, the discharge capacity is still 60 mA h g^{-1}. Fig. 59 d shows a cell in which it was insert an interlayer between the cathode and the separator. This interlayer seems to act as a barrier for trapping the polysulphides limiting the parasitic reaction [130]. It reduces the "shuttle" effects at the Li cathode suggesting that the most of the polysuphides are trapped. Moreover, the interlayer has not adverse effect on the cathode and it seems to enhance the electrochemical stability of the cell. In this study, two interlayers used were a glass fiber and carbon fiber paper. They show high capacity ant it can be attributed to the interlayer that is able to trap the polysuphides, inhibiting the abatement of the current. The comparison between C-βNS_MI_rGO with the glass fiber and C-βNS_MI_rGO with carbon fiber shows that their initial performance is similar, demonstrating 1103 and 1108 mA h g^{-1} at 0,1 C, respectively. However, the discharge capacity after 100 cycles at C/5 is significantly lower for the one with glass fiber, resulting in 483 mA h g^{-1}, compared with 723 mA h g^{-1} of the other one.

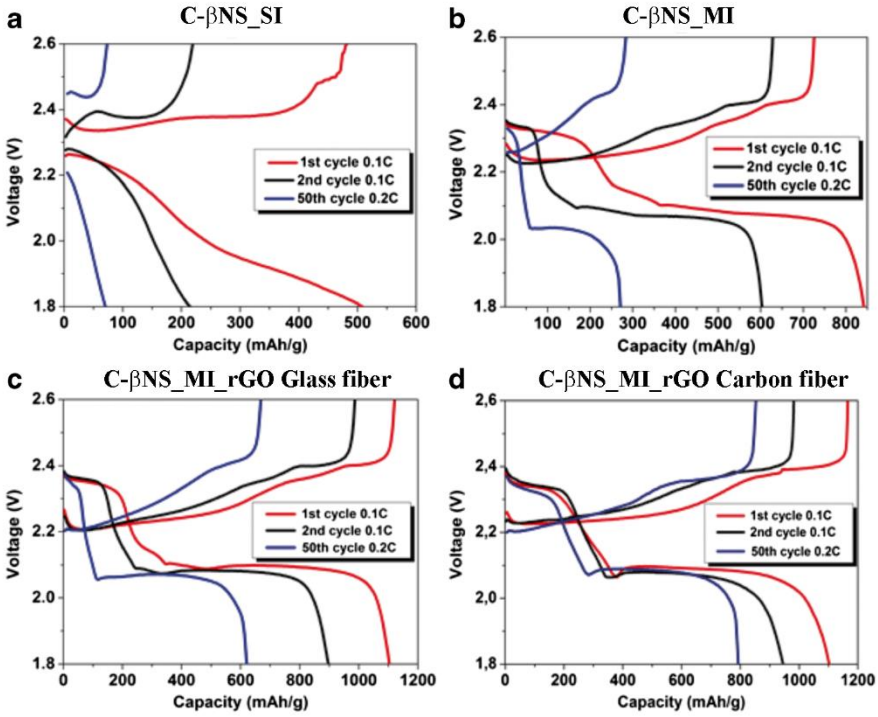

Figure 60: Charge and discharge capacity of the carbons.

Discharge capacity	C-βNS_SI	C-βNS_MI	C-βNS_MI_rGO glass fiber	C-βNS_MI_rGO Carbon fiber
1st cycle at C/10	508,25	841,89	1103,01	1108,10
2nd cycle at C/10	214,72	603,09	897,04	946,95
5th cycle at C/10	157,89	447,06	746,87	909,37
6th cycle at C/5	92,90	342,24	626,05	846,82
10th cycle at C/5	95,66	298,39	547,50	839,36
50th cycle at C/5	70,11	271,01	621,48	808,61
100th cycle at C/5	49,23	203,43	482,97	722,71

Table 28: Discharge capacity reported for diverse cycles with different C rates.

The long-term cycling performance of the three Li–S cells was studied and the results are listed in table 28. At a rate of 0,2 C, an initial capacity of about 100 mA h g^{-1} was measured for C-βNS_SI, followed by a decrease to relatively stable capacity of 70 mA h g^{-1} after 50 continuous cycles, indicating the poor efficiency of this type of cathode. For C-βNS_MI about 0,40% decrease in the capacity from the 6^{th} to the 100th cycle at the same rate of 0,2 C was noted. At the end of the cycling test, the discharge capacity was at about 200 mA h g^{-1}. As for the C-βNS_MI_rGO, the performance of 620 mA h g^{-1} at the 50th cycle. The initial capacity observed for C-βNS_MI_rGO at 0,2 C can be probably due to the activation of the loaded materials. Initial lower values of capacity can also be due to incomplete soaking of the cathode by the electrolyte. Then, the cathode with carbon paper interlayer showed excellent performance for prolonged cycling at 0,2 C and it showed capacity 850 mA h g^{-1} that is stable for more than 100 cycles with about 0,14% capacity loss per cycle. Moreover, this electrode had superior rate capability of more than 450 mA h g^{-1} at 1 C and good capacity recovery, from about 800 mA h g^{-1} at 0.2 C to 600

mA h g^{-1} at 0,5 C and then back to 800 mA h g^{-1}, indicating its high reversibility.

3.4 REMOVAL OF ORGANIC POLLUTANTS FORM WATER SOLUTION

In this part of the thesis, the aim was to have a material able to remove organic pollutants from water. For this purpose, it was decided to use two charged-dyes, the methylene blue (MB) and the methyl orange (MO). We decided to use the βNS-carbons, pyrolyzing the NS at 3 different temperature, 300°C, 500°C and 800°C. The samples were coded, C-βNS300, C-βNS500 and C-βNS, respectively. It is note [131] that the pyrolysis temperature has an influence on the surface. The possibility to tailor the structure and so the surface of the materials depends also on the composition of the starting materials [28]. For investigating the possibility to have some active groups on the surface, an elemental analysis was performed. The results are listed in table 29 and a comparison with the bare βNS is also reported.

Samples	%C	%H	%N	%S	$\%O_{calculated}$
βNS	49,7	6,5	3,0	0	40,08
C-βNS300	65,7	3,5	1,3	0	29,5
C-βNS500	73,1	2,6	1,28	0	23,5
C-βNS	78	0,69	1,26	0	20,05

Table 29: C-H-N-S of βNS, C-βNS300, C-βNS500 and C-βNS.

In general, with respect to the bare precursors, it is possible to observe that, by increasing the pyrolysis temperature, the carbonization pathway leads to a progressive increment of C (from 49,7 in βNS to 78 in C-βNS) and a reduction in H (from 6,5% in βNS to 20,69% in C-βNS) contents, suggesting the progressive carbonization process. The content of heteroatoms (nitrogen) remains constant during the pyrolysis suggesting a progressive enrichment in N of the materials respect to the quantity of carbon that leads to a N-doped carbon. The decrease in the contents of H and O at higher temperature was likely due to the decomposition of the oxygenated bonds and release of low molecular weight by-products containing H and O. Interestingly, the N content can be attributed to the incorporation of nitrogen into the structures which were resistant to lower temperature and not easily volatilized [132].

Furthermore, the ratios of H/C (the degree of aromaticity) [133] and O/C (the degree of polarity) [134] varied as a function of pyrolysis temperature. In our study, the H/C ratios significantly decreases from 0,13 for the βNS to 0,051 for C-βNS300 and 0,036 C-βNS500 to 0,0088 C-βNS with the increasing temperature. For the O/C ratio, it is possible to observe 0,08 for the βNS, 0,45 for C-βNS300, 0,32 for C-βNS500 and 0,26 for C-βNS. The gradually reduced in the H/C and O/C atomic ratios with the increasing pyrolysis temperature was mainly contributed to the dehydration reactions [135], which could be occurred. In addition, the H/C and O/C ratios also indicated that the structural transformations [133] and surface hydrophilicity of carbons from Ns are modified by the extending of carbonization and the losing of functional groups containing O and H (such as hydroxyl, carboxyl, et al.) at higher temperature resulting in the lower ratios of H/C and O/C, indicating that the surface is becoming more aromatic.

The SEM was performed on βNS-derived carbons. As shown in Fig. 61, the precursor βNS (Fig. 61 a) presents geometrical shape due to the grinding process carried out after the synthesis whereas the carbon materials present a hollowed spherical morphology, with an irregular surface in the case of C-βNS300 (Fig. 61 b) becoming much smooth passing from C-βNS500 (Fig. 61 c) to C-βNS (Fig. 61 d).

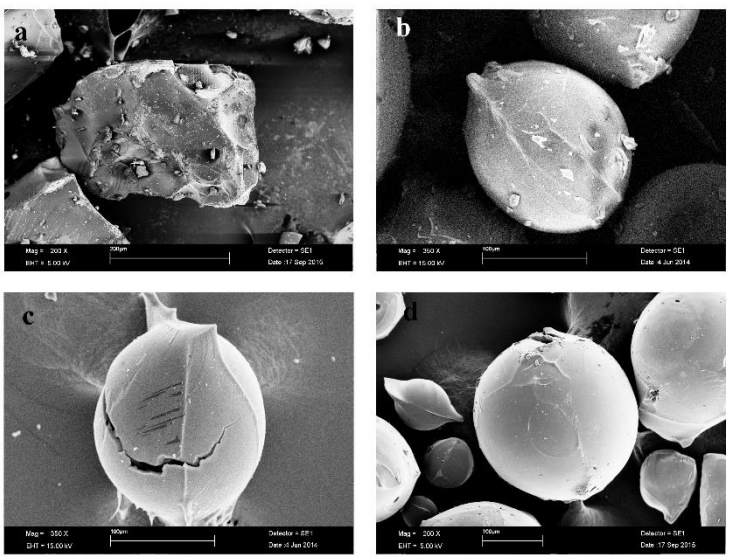

Figure 61: SEM micrographs of βNS (a), C-βNS300, C-βNS500, C-βNS.

The physical properties of all carbonaceous materials were evaluated using a gas-volumetric technique and the results were summarized in Table 30:

Sample	Surface Area	Micropore Volume	Pore Width
	($m^2\ g^{-1}$)	($cm^3\ g^{-1}$)	(Å)
C-βNS300	2,63	0	0
C-βNS500	164	0,05	13-19
C-βNS	560	0,05	5-16

Table 30: Physical properties of the carbons

The adsorption isotherms are reported in Fig. 62 and they suggest that adsorption is very limited for C-βNS300 sample whereas it increases with the pyrolysis temperature as a consequence of the increase of surface area caused by the development of porosity. C-βNS500, in fact, shows an isotherm of the I type of the IUPAC classification ascribable to microporous solids. In detail, C-βNS300 has a specific surface area of ca. 2 $m^2\ g^{-1}$, whereas C-βNS500 has 121 $m^2\ g^{-1}$. For the evaluation of the specific surface are, the Langmuir equation was used, while for the porosity, the DFT method.

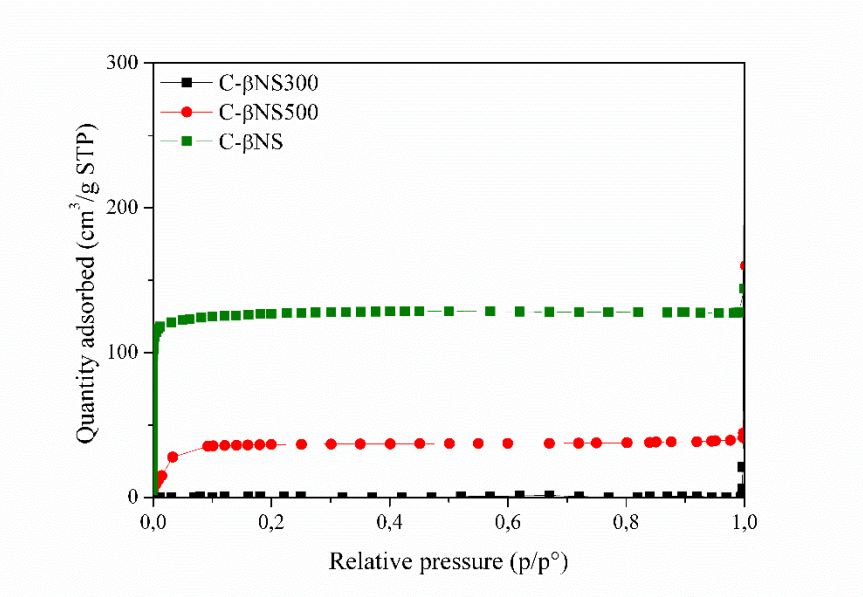

Figure 62: N_2 adsorption isotherms for C-βNS300, C-βNS500, C-βNS.

In Fig. 63 are reported the calibration curves for MB and MO respectively:

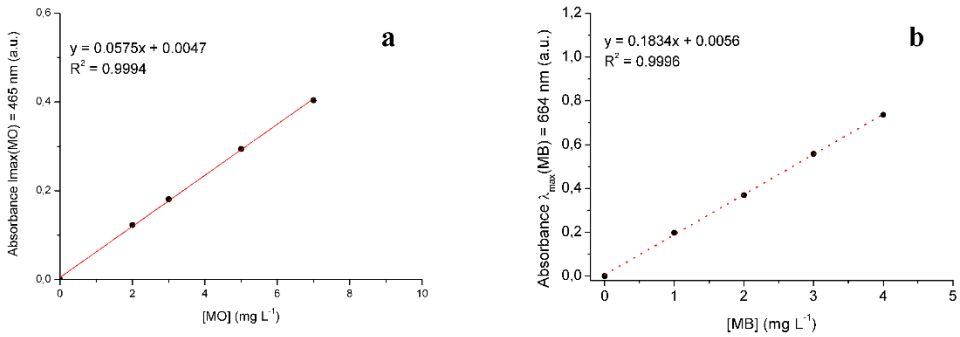

Figure 63: Calibration curves of MO (a) and MB (b).

Preliminary tests were performed on the carbons in the presence of MB and MO in the following conditions: initial dye concentration C_0 = 100 mg L^{-1}, sorbent concentration [sorbent] = 1000 mg L^{-1}, contact time t = 24 h, ionic strength [KCl] = 0.01M, pH = 6, circumneutral and temperature T = 25°C. The results obtained clearly evidenced that the adsorption is negligible in the presence of MB in presence of C-βNS, and so a different

kind of analysis were performed. Moreover, all the samples show a strong electrostatic repulsion between the negatively charged dye MO and the negatively charged surface of the carbons. Conversely, interesting performances in terms of MB adsorption were evidenced by C-βNS300 and C-βNS500, phenomenon attributable to the electrostatic attraction between the positively charged dye MB and the negatively charged surfaces of the adsorbing materials, thus suggesting that these carbons are charge-selective sorbing materials. The MB adsorption isotherm on C-βNS300 and C-βNS500 are reported in Fig. 64.

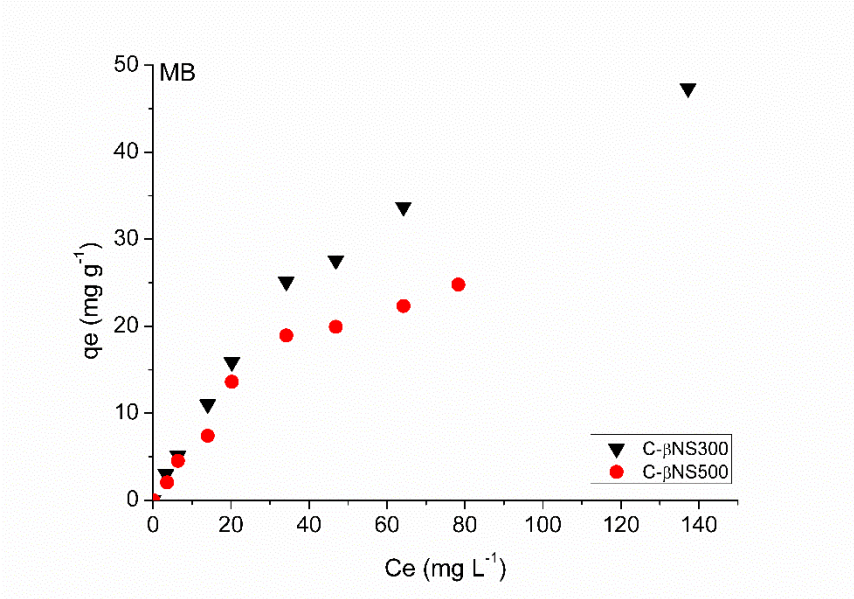

Figure 64: Adsorption isothermal experiments (expressed as mg g^{-1} vs. mg L^{-1}) for C-βNS300 and C-βNS500.

The results obtained evidenced that the adsorption performances of the prepared carbonaceous materials are 27,72 mg g^{-1} for C-βNS300 and 20,31 mg g^{-1} for C-βNS500. Nevertheless, the observed performances are equivalent to those of analogous systems described in the literature. In particular, Lonappan et al. [136] evidenced that carbonaceous materials obtained from different sources (i.e., pig manure, paper and pine wood) show a MB sorption capacity, for analogous dye concentration C_e, in the range 7,8-25,0 mg g^{-1}, while Fan et al. [137] reported that a carbon prepared from co-pyrolysis of municipal sewage sludge and tea waste have a MB sorption capacity of 12,6 mg g^{-1}.

Considering the specific surface area trend, C-βNS500 present a higher surface area than C-βNS300, but its performance towards MB is worse. This behavior can be rationalized considering the chemical nature of the materials surface. In fact, both FTIR spectra shown previously and elemental analyses suggest that materials pyrolyzed at the higher temperatures began the transition to graphite losing most part of the polar functionalities of the precursor, which are still present at the surface of C-βNS300. Probably, these polar moieties are responsible for the more efficient adsorption of MB. To prove this hypothesis, the comparison was performed reporting the MB adsorbed amounts, as mg m^{-2}, referring to the specific surface area of the adsorbing materials. The curves are reported in Fig. 65. The conclusion is evident: higher the number of the residual polar moieties at the surface of the carbonaceous materials, lower the pyrolysis temperature, higher the affinity between the adsorbing material and MB molecules.

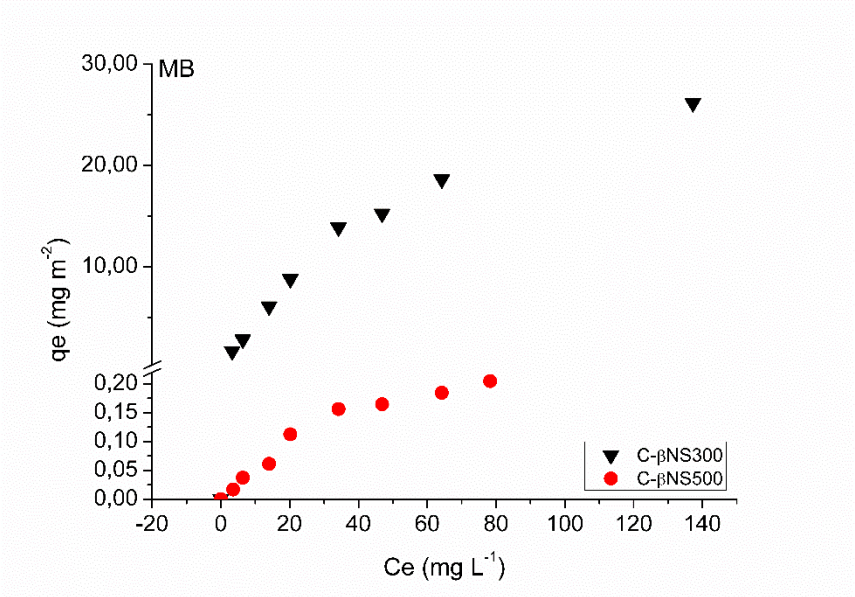

Figure 65: Adsorption isothermal experiments (expressed as mg m^{-2} vs. mg L^{-1}) for C-βNS300 and C-βNS500.

In conclusion, C-βNS300 possesses the lowest specific surface areas but shows the highest affinity towards polar substrates.

Lastly, in order to evaluate the possibility of regenerating the exhausted sorbents, desorption experiments were performed on MB-saturated samples by washing the carbons with two different solutions in sequence: i) 0.01M KCl (at pH = 6) and, ii) 0.1M NaOH. Experimental results indicated that the cationic MB can be completely removed from both C-βNS300 and C-βNS500 (Fig. 65), thus indicating the possibility of recycling these materials.

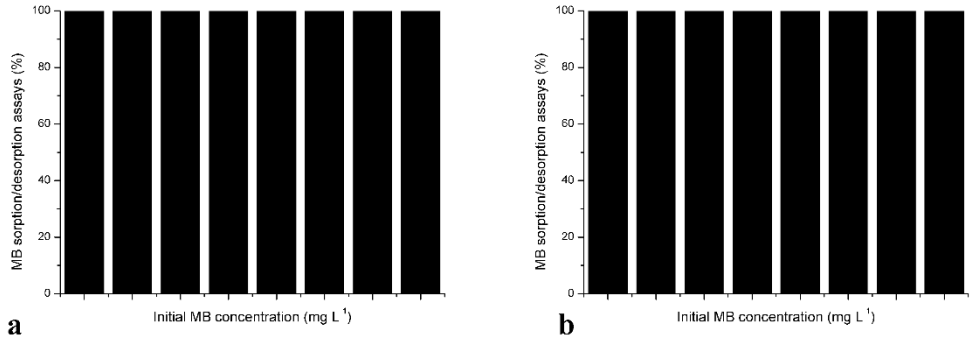

Figure 66: Desorption experiments of MB: dye removed after washing with 0.01M KCl at pH = 6 and 0.1M NaOH the C-βNS300 and C-βNS500.

In Fig. 67 is reported the adsorption of MB by the C-βNS, using a concentration of 5 ppm. The preliminary results carried out overnight suggests trying to adsorb the MB at low concentration and to evaluate it in function of time.

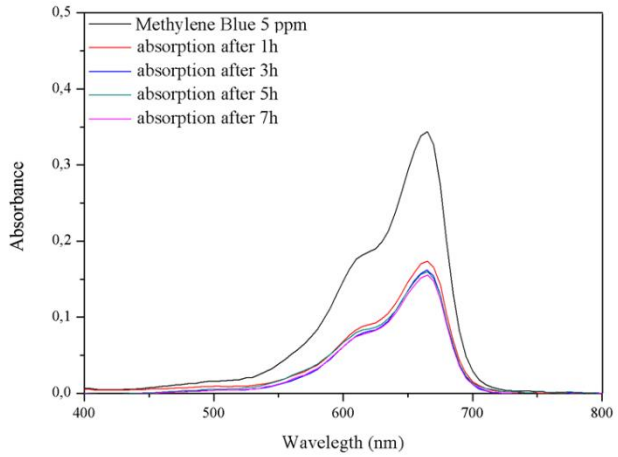

Figure 67: Adsorption of MB after different contacts time for the C-βNS.

The maximum loading of MB is reached after 1 h of contact time. Anyway, leaving the solution in contact with the substrate a little amount of MB can be absorbed. The results obtained are listed in table 31:

Time	mg g^{-1} absorbed
1h	11,86
3h	14,83
5h	15,00
7h	13,14

Table 31: Quantity of MB adsorbed in function of time.

In conclusion, the nanosponges can be effective green sources for the production of low-cost carbon materials via pyrolysis at mild conditions. Different pyrolysis temperatures suggest that it is possible to have a versatile material, changing the pyrolysis temperature, that can be used for removing both low and high quantity of organic pollutants.

4 CONCLUSIONS

In this thesis, it was described a simple strategy for the synthesis of porous carbon material from NS. Using the pyrolysis at mild condition it was possible to obtained carbons with specific feature that makes them suitable for many industrial applications. From the data collected during the pyrolysis study, the nanosponges during the heating treatment have an alteration of the saccharide structure and the scission of the bonds of the cross—linking bridges. The numerous unsaturated species can act as a precursor for the rearrangement of the structure and the formation of the polycyclic aromatic structure typical of the char. The analogies with the pyrolysis of the cellulose and starch allows to understand that both the materials can undergo pyrolysis via two competitive pathways. The first, called *dehydration*, in which the formation of the char is favorite. Simultaneously, the second path, named *depolymerization,* can occurs leading to the formation of high boiling products. This route involves intramolecular reaction and it is possible to affirm that the βCD and Lc follow, during the degradation, mainly this path. The presence of the cross-linker has a great influence on the pyrolysis path, favoring mostly the dehydration and so the formation of char. Thus, the PMDA has a great influence on the pyrolysis path. It can affect the competition between the two competitive between volatilization and carbonization, favoring the second and so altering the amount of residue produced. Basically, the cross-linking bond between the saccharide and the PMDA is an ester bond that can be easily by the temperature causing the formation of fragments that can interact among them reducing the quantity of volatiles released and consequently increase the amount of carbon produced. Moreover, the dehydration of the glucose rings of the βCD and of the Lc can also promote the generation of C=C bonds increasing the quantity of char produced. Lastly the presence of an aromatic group in the PMDA can give a further contribution to the char yield.

The C-βNS shows a Langmuir specific surface area of 560 $m^2\ g^{-1}$ and a narrow pore size in the range of 5-16 Å corresponding to 0,08 $cm^3\ g^{-1}$ of total porosity. The C-LcNS has a specific surface are of 684 $m^2\ g^{-1}$ and 5–17 Å of pore size for a total porosity of 0.16 $cm^3\ g^{-1}$.

SEM observation reveals a peculiar morphology of the carbons, composed of perfectly hollow spherical particles.

The effect of heating rate on the pyrolysis was also investigated. Whereas the heating rate has not an influence on the physical properties of the final carbons for the βNS, for the LcNS, a fast heating rate inhibits the development of the specific surface area and of the porosity of the systems. This fact can be attributed to two factors, high heating rate prevents the rearrangement of the structure and avoids the development of this empty spaces. It is possible to suppose that the volatiles could be generated too fast during the pyrolysis and so they not have enough time for leaving the system blocking the pores developing. All these events can only cause the decreasing of the specific surface area and the reduction of the total volume of the pores.

For obtaining a carbon with better physical characteristics, the quantity of catalyst has been decreased in order to improve the properties of the sample and to lead the synthesis towards more green preparation, amine-free. Obviously, it was found out that decreasing the quantity of catalyst the performance, in term of time and amount of products that can be made, has been reduced, dramatically. Anyway, all the samples obtained with different molar ratio between the βCD and TEA were subjected to pyrolysis at 800°C. The residues were collected and the specific surface area and the porosity were evaluated. these data, it is possible to conclude that the TEA has not any type of influence in the development of the specific surface area or in the growth of the pores. It seems that the TEA is not involved in the pyrolysis reactions that lead to the formation of the porous carbon materials form βNS. Anyway, for an efficient and fast synthesis of the NS high amounts of TEA are compulsory.

Other two catalysts were employed: triethanolamine (TEAOH) and 1,4-diazabicyclo[2.2.2]octane (DABCO) using the synthetic conditions of the classical synthesis. The two NS were pyrolyzed and then their residues were collected and the analyzed using the gas-volumetric instrument. It was possible to obtained a cross-linking reaction using only 1:1 βCD:TEAOH and 1:4 βCD:DABCO. It was found out that The use of the TEAOH in the synthesis seems to lead to a carbon with the same characteristic obtained with the one with TEA. Cornerwise, the presence of DABCO generates a carbon with less pores and consequently a lower specific surface area.

The energetic study of the adsorption process of a CO_2 was carried out using the microcalorimeter. It allowed to determinate the heat of adsorption developed during the adsorption and the quantity of gas-adsorbed. For the C-βNS primary adsorption we estimated q_0 of 19,79 kJ mol^{-1} for the second 15,75 kJ mol^{-1}. For the C-LcNS primary adsorption we estimated q_0 of 15,73 kJ mol^{-1} for the second 22,99 kJ mol^{-1}. These values show that the adsorption on these materials could be considered like a physisorption. These results are important because the interaction between the CO_2 and the surface is not strong in order of the chemical bond, which would facilitate the regeneration of the carbons in an industrial application. The hydrophilicity or hydrophobicity of a solids was also evaluated. To evaluate the hydrophilicity/ hydrophobicity of the surface the evolution of the heat adsorption of water vapor with the coverage has been studied and it was found the adsorption for both the samples is less than 370 kJ mol^{-1} and so it is possible to affirm that the water is not chemically bonded. Moreover, the carbons obtained by nanosponges exhibited some hydrophilic sites, which are filled up first. Then, the heat of adsorption fell below the latent heat of liquefaction of water for both the samples, hence the surface has many hydrophobic sites.

The microbalance was remarkable used for testing the ability of the materials in the capture of carbon dioxide at different temperature, form 30°C to 120°C. The maximum adsorption at 30°C is 204 mg g^{-1} for C-βNS and it becomes half when the adsorption is leaded at 120°C. for the C-LcNs the adsorption at 30°C is 187 mg g^{-1} whereas at 120°C is about 133 mg g^{-1}. It is very encouraging to find out that at 120°C our carbons are still able to adsorb CO_2. Form this analysis very important thermodynamic parameters were evaluated. The enthalpy values show that the adsorption process is exothermic whereas the $\Delta G°$ indicates that the adsorption of the carbon dioxide onto the surface of the carbons is spontaneous ($\Delta G°<0$). The entropy values are positive ($\Delta S°>0$) confirming the spontaneously of the process.

Thanks to the collaboration with the Politecnico di Torino, we have proposed a novel carbon matrix derived from bio-based material to host sulphur for Li–S battery application. It was successfully demonstrated that the C-βNS can entrap the S inside its matrix. It is necessary to provide a suitable conductive network by rGO wrapping, but we were able to reach

1103 mA h g^{-1} at 0,1 C and 626 mA h g^{-1} at 0,2 C with capacity loss of 0,2% per cycle for more than 100 cycles. The presence of the interlayer raised the capacity of the cathode. Thus, it was found out that the C-βNS can be successfully use in Li-S batteries for automotive field.

In the end, different pyrolysis temperatures were selected and the relative C-βNS were deeply characterized. We demonstrate that the βNS materials pyrolyzed at increased temperature show an increasing of the specific surface area caused by porosity development and the formation of hollowed microporous particles. The adsorbing properties of these systems were evaluated in simulated-wastewater treatments, by measuring their sorption performances in the removal of differently-charged chemicals from aqueous environment at circumneutral pH and at 25°C. These preliminary tests evidenced that these carbon materials are effective in the removal of positively-charged molecules from water, indicating an important charge-selectivity which can be exploited in wastewater purification treatments. Additionally, the adsorption of the cationic target molecule to C-βNS-derived materials is completely reversible thus making them very appealing in the industrial viewpoint.

The analysis of the adsorption curves reported as a function of the specific surface area of the adsorbing materials revealed that the lowest the temperature of the pyrolysis, corresponding to the highest number of polar functional groups on the surface, the highest the affinity of the material towards polar substrates, suggesting that the strategy to obtain carbons with enhanced adsorption capacity towards polar substrates is to pyrolyze at low temperature, saving energy and time, and perform post-pyrolysis treatments aimed at increasing the specific surface area of the adsorbing materials.

BIBLIOGRAPHY

1 A. R. Millward and O. M. Yaghi, *J. Am. Chem. Soc.*, 2005, **127**, 17998–17999.

2 L. Zou, Y. Sun, S. Che, X. Yang, X. Wang, M. Bosch, Q. Wang, H. Li, M. Smith, S. Yuan, Z. Perry and H. C. Zhou, *Adv. Mater.*, 2017, **29**, 1–35.

3 P. Misaelides, *Microporous Mesoporous Mater.*, 2011, **144**, 15–18.

4 H. Hentze, *Curr. Opin. Solid State Mater. Sci.*, 2001, **5**, 343–353.

5 R. J. White, V. Budarin, R. Luque, J. H. Clark and D. J. Macquarrie, *Chem. Soc. Rev.*, 2009, **38**, 3401.

6 J. Lee, J. Kim and T. Hyeon, *Adv. Mater.*, 2006, 18, 2073–2094.

7 M. K. Amosa, M. S. Jami, M. F. R. Alkhatib, D. N. Jimat and S. A. Muyibi, *Water Qual. Expo. Heal.*, 2015, **7**, 603–616.

8 H. Yang, Z. Xu, M. Fan, R. B. Slimane, A. E. Bland and I. Wright, *J. Environ. Sci.*, 2008, **20**, 14–27.

9 Y. Xu, Y. Wen, Y. Zhu, K. Gaskell, K. A. Cychosz, B. Eichhorn, K. Xu and C. Wang, *Adv. Funct. Mater.*, 2015, **25**, 4312–4320.

10 X. Xie, M. Ye, L. Hu, N. Liu, J. R. McDonough, W. Chen, H. N. Alshareef, C. S. Criddle and Y. Cui, *Energy Environ. Sci.*, 2012, **5**, 5265–5270.

11 Y. Guo, J. Zhao, H. Zhang, S. Yang, J. Qi, Z. Wang and H. Xu, *Dye. Pigment.*, 2005, **66**, 123–128.

12 Z. Li, L. Yuan, Z. Yi, Y. Sun, Y. Liu, Y. Jiang, Y. Shen, Y. Xin, Z. Zhang and Y. Huang, *Adv. Energy Mater.*, 2014, **4**, 1–8.

13 Z. Karim, A. P. Mathew, M. Grahn, J. Mouzon and K. Oksman, *Carbohydr. Polym.*, 2014, **112**, 668–676.

14 P. H. Emmett, *Chem. Rev.*, 1948, **43**, 69–148.

15 R. E. Franklin, *Proc. R. Soc. A Math. Phys. Eng. Sci.*, 1951, **209**, 196–218.

16 P. J. F. Harris, *J. Mater. Sci.*, 2013, **48**, 565–577.

17 A. C. Forse, C. Merlet, P. K. Allan, E. K. Humphreys, J. M. Griffin, M. Aslan, M. Zeiger, V. Presser, Y. Gogotsi and C. P. Grey, *Chem. Mater.*, 2015, **27**, 6848–6857.

18 P. J. F. Harris, *Int. Mater. Rev.*, 1997, **42**, 206–218.

19 R. J. White, *The Search of Functional Porous Carbon Materials from Susitainable Precursor*, RCS Green., 2015.

20 S. I. Tsyganova, I. V. Korol'kova, O. Y. Fetisova, G. N. Bondarenko, V. F. Kargin, S. I. Tsyganova, I. V. Korol'kova, O. Y. Fetisova, G. N. Bondarenko and V. F. Kargin, *Russ. J. Appl. Chem.*, 2014, **87**, 360–364.

21 S. De, A. M. Balu, J. C. Van Der Waal and R. Luque, *ChemCatChem*, 2015, **7**, 1608–1629.

22 A. Ahmadpour and D. D. Do, *Carbon N. Y.*, 1997, **35**, 1723–1732.

23 J. Han, G. Xu, B. Ding, J. Pan, H. Dou and D. R. MacFarlane, *J. Mater. Chem. A*, 2014, **2**, 5352–5357.

24 D. W. Wang, F. Li, M. Liu, G. Q. Lu and H. M. Cheng, *Angew Chem*, 2008, **47**, 379–382.

25 M.-M. Titirici and M. Antonietti, *Chem. Soc. Rev.*, 2010, **39**, 103–116.

26 M. Sevilla and A. B. Fuertes, *Chem. - A Eur. J.*, 2009, **15**, 4195–4203.

27 A. D. Roberts, X. Li and H. Zhang, *Chem. Soc. Rev.*, 2014, **43**, 4341–4356.

28 A. Bridgwater and G. Peacocke, *Renew. Sustain. Energy Rev.*, 2000, **4**, 1–73.

29 L. van Zwieten, S. Kimber, S. Morris, K. Y. Chan, A. Downie, J. Rust, S. Joseph and A. Cowie, *Plant Soil*, 2010, **327**, 235–246.

30 S. Kloss, F. Zehetner, A. Dellantonio, R. Hamid, F. Ottner, V. Liedtke, M. Schwanninger, M. H. Gerzabek and G. Soja, *J. Environ. Qual.*, 2012, **41**, 990.

31 S. Soares, G. Camino and S. Levchik, *Polym. Degrad. Stab.*, 1995,

49, 275–283.

32 F. Shafizadeh and Y. Z. Lai, 1978, **397**, 278–284.

33 E. L. Akim, *Pure Appl. Chem.*, 1967, **14**, 475–480.

34 S. Li, J. Lyons-Hart, J. Banyasz and K. Shafer, *Fuel*, 2001, **80**, 1809–1817.

35 T. Hosoya, H. Kawamoto and S. Saka, *J. Anal. Appl. Pyrolysis*, 2008, **83**, 64–70.

36 H. Kawamoto, H. Morisaki and S. Saka, *J. Anal. Appl. Pyrolysis*, 2009, **85**, 247–251.

37 M. J. Iqbal and M. N. Ashiq, *J. Hazard. Mater.*, 2007, **139**, 57–66.

38 S. M. Manocha, *Sadhana*, 2003, **28**, 335–348.

39 H. R. J. and R. S. Williams, *J. FUELS Lubr.*, 1990, **99**, 753–775.

40 R. W. Pekala, J. C. Farmer, C. T. Alviso, T. D. Tran, S. T. Mayer, J. M. Miller and B. Dunn, *J. Non. Cryst. Solids*, 1998, **225**, 74.

41 R. W. Pekala, *J. Mater. Sci.*, 1989, **24**, 3221–3227.

42 R. J. White, N. Yoshizawa, M. Antonietti and M.-M. Titirici, *Green Chem.*, 2011, **13**, 2428.

43 T. P. Fellinger, R. J. White, M. M. Titirici and M. Antonietti, *Adv. Funct. Mater.*, 2012, **22**, 3254–3260.

44 C. Moreno-Castilla and F. J. Maldonado-Hódar, *Carbon N. Y.*, 2005, **43**, 455–465.

45 Q. Zhang, J. Q. Huang, W. Z. Qian, Y. Y. Zhang and F. Wei, *Small*, 2013, **9**, 1237–1265.

46 N. Saifuddin, A. Raziah and A. Junizah, *J. Chem.*, 2013, **2013**, 1–18.

47 D. Yuan, L. Ding, H. Chu, Y. Feng, T. P. Mc nicholas and J. Liu, *Nanoletters*, 2008, **8**, 2576–2579.

48 M. Kumar and Y. Ando, *Diam. Relat. Mater.*, 2003, **12**, 1845–1850.

49 A. B. Suriani, A. A. Azira, S. F. Nik, R. Md Nor and M. Rusop, *Mater. Lett.*, 2009, **63**, 2704–2706.

50 2009.

51 S. A. B. D. Malhotra, S. Srivastava, *Mater. Res. Soc. Symp*, 2015, **1725**, 1–12.

52 M. Meyyappan, L. Delzeit, A. Cassell and D. Hash, 2003, **12**, 205–216.

53 M.-F. Yu, B. S. Files, S. Arepalli and R. S. Ruoff, *Phys. Rev. Lett.*, 2000, **84**, 5552–5555.

54 A. Bianco, K. Kostarelos and M. Prato, *Curr. Opin. Chem. Biol.*, 2005, **9**, 674–679.

55 R. L. Mieville and K. K. Robinson, *Mega-Carbon Co.*

56 H. C. Foley, *Microporous Mater.*, 1995, **4**, 407–433.

57 H. F. Stoeckli, *Carbon N. Y.*, 1990, **28**, 1–6.

58 A. R. Mohamed, M. Mohammadi and G. N. Darzi, *Renew. Sustain. Energy Rev.*, 2010, **14**, 1591–1599.

59 H. Liu, F. Xie, L. Yu, L. Chen and L. Li, *Prog. Polym. Sci.*, 2009, **34**, 1348–1368.

60 H. Wang, Q. Dai, Q. Li, J. Yang, X. Zhong, Y. Huang, A. Zhang and Z. Yan, *Solid State Ionics*, 2009, **180**, 1429–1432.

61 L. Ding, B. Zou, Y. Li, H. Liu, Z. Wang, C. Zhao, Y. Su and Y. Guo, *Colloids Surfaces A Physicochem. Eng. Asp.*, 2013, **423**, 104–111.

62 V. Budarin, J. H. Clark, J. J. E. Hardy, R. Luque, K. Milkowski, S. J. Tavener and A. J. Wilson, *carbonaceous Mater.*, 2006, **118**, 3866–3870.

63 F. Trotta, M. Zanetti and G. Camino, *Polym. Degrad. Stab.*, 1966, **1964**, 2139–2143.

64 B. H. Han, W. Zhou and A. Sayari, *J. Am. Chem. Soc.*, 2003, **125**, 3444–3445.

65 H. Chang, S. H. Joo and C. Pak, *J. Mater. Chem.*, 2007, **17**, 3078.

66 C. Moreno-Castilla, O. P. Mahajan, P. L. Walker, H. J. Jung and M. A. Vannice, *Carbon N. Y.*, 1980, **18**, 271–276.

67 M. Pérez-Mendoza, M. Domingo-García and F. J. López-Garzón,

Appl. Catal. A Gen., 2002, **224**, 239–253.

68 R. S. Drago, S. C. Petrosius, G. C. Grunewald and W. H. Brendley, 1994, 340–352.

69 H. Li, Z. Song, X. Zhang, Y. Huang, S. Li, Y. Mao, H. J. Ploehn, Y. Bao and M. Yu, *Science (80-.).*, 2013, **342**, 95–98.

70 A. Kapoor and R. T. Yang, *Chem. Eng. Sci.*, 1989, **44**, 1723–1733.

71 C. A. Grande, S. Cavenati, F. A. Da Silva and A. E. Rodrigues, *Ind. Eng. Chem. Res.*, 2005, **44**, 7218–7227.

72 R. B. Eldridge, *Ind. Eng. Chem. Res.*, 1993, **32**, 2208–2212.

73 R. K. Srivastava and W. Jozewicz, *J. Air Waste Manag. Assoc.*, 2001, **51**, 1676–1688.

74 K. T. Chue, J. N. Kim, Y. J. Yoo, S. H. Cho and R. T. Yang, *Ind. Eng. Chem. Res.*, 1995, **34**, 591–598.

75 I. Kim and H. F. Svendsen, *Ind. Eng. Chem. Res.*, 2007, **46**, 5803–5809.

76 J. T. Yeh, K. P. Resnik, K. Rygle and H. W. Pennline, *Fuel Process. Technol.*, 2005, **86**, 1533–1546.

77 H. P. Huang, Y. Shi, W. Li and S. G. Chang, *Energy and Fuels*, 2001, **15**, 263–268.

78 O. Dr. Bolland, *Carbon dioxide capture*, 2009.

79 A. Manthiram, S.-H. Chung and C. Zu, *Adv. Mater.*, 2015, **27**, 1980–2006.

80 P. G. Bruce, S. A. Freunberger, L. J. Hardwick and J.-M. Tarascon, *Nat. Mater.*, 2012, **11**, 19–29.

81 U. Zubair, A. Anceschi, F. Caldera, M. Alidoost, J. Amici, C. Francia, M. Zanetti, F. Trotta, S. Bodoardo and N. Penazzi, *J. Solid State Electrochem.*, 2017, **21**, 3411–3420.

82 H. S. Ryu, J. W. Park, J. Park, J.-P. Ahn, K.-W. Kim, J.-H. Ahn, T.-H. Nam, G. Wang and H.-J. Ahn, *J. Mater. Chem. A*, 2013, **1**, 1573–1578.

83 N. Jayaprakash, J. Shen, S. S. Moganty, A. Corona and L. A. Archer, *Angew. Chem.*, 2011, **123**, 6026–6030.

84 M. Vakili, M. Rafatullah, B. Salamatinia, A. Zuhairi, M. Hakimi, K. Bing, Z. Gholami and P. Amouzgar, *Carbohydr. Polym.*, 2014, **113**, 115–130.

85 J. Lee, S. Choi and R. Thiruvenkatachari, 2006, **69**, 196–203.

86 K. Chen, J. Wu, C. Huang and Y. Liang, 2003, **101**, 241–252.

87 R. Gong, Y. Ding, M. Li, C. Yang, H. Liu and Y. Sun, 2005, **64**, 187–192.

88 L. Wang, J. Zhang and A. Wang, *DES*, 2011, **266**, 33–39.

89 W. S. W. Ngah, L. C. Teong and M. A. K. M. Hanafiah, *Carbohydr. Polym.*, 2011, **83**, 1446–1456.

90 A. Aluigi, F. Rombaldoni, C. Tonetti and L. Jannoke, *J. Hazard. Mater.*, 2014, **268**, 156–165.

91 I. M. Banat, P. Nigam, G. Mcmullan, R. Marchant and D. Singh, 1997, **23**, 547–551.

92 B. Shi, G. Li, D. Wang, C. Feng and H. Tang, 2007, **143**, 567–574.

93 N. Al-bastaki, 2004, **43**, 1561–1567.

94 I. Arslan and A. Balciog, 2000, **47**, 207–218.

95 C. Wang, A. Yediler, D. Lienert, Z. Wang and A. Kettrup, 2003, **52**, 1225–1232.

96 B. Devassy, D. Goyal and S. Khanna, *Int. Biodeterior. Biodegradation*, 2009, **63**, 462–469.

97 S. D. Eastburn and B. Y. Tao, *Biotechnol. Adv.*, 1994, **12**, 325–339.

98 G. Wenz, *Angew. Chemie-International Ed. English*, 1994, **33**, 803–822.

99 a E. Christian, H. S. Byun, N. Zhong, M. Wanunu, T. Marti, a Fürer, F. Diederich, R. Bittman and G. H. Rothblat, *J. Lipid Res.*, 1999, **40**, 1475–82.

100 E. M. M. Del Valle, *Process Biochem.*, 2004, **39**, 1033–1046.

101 S. Brochsztain and M. J. Politi, *Langmuir*, 1999, **15**, 4486–4494.

102 J. Szejtli, *Chem. Rev.*, 1998, **98**, 1743–1754.

103 H. Liu, F. Xie, L. Yu, L. Chen and L. Li, *Prog. Polym. Sci.*, 2009, **34**, 1348–1368.

104 T. Y. Bogracheva, V. J. Morris, S. G. Ring and C. L. Hedley, *Biopolymers*, 1998, **45**, 323–332.

105 F. Caldera, M. Tannous, R. Cavalli, M. Zanetti and F. Trotta, *Int. J. Pharm.*, 2017, **531**, 470–479.

106 L. Guo, G. Gao, X. Liu and F. Liu, *Mater. Chem. Phys.*, 2008, **111**, 322–325.

107 H. Ataee-Esfahani, Y. Nemoto, L. Wang and Y. Yamauchi, *Chem. Commun.*, 2011, **47**, 3885.

108 F. Trotta, *Cyclodextrins Pharm. Cosmet. Biomed. Curr. Futur. Ind. Appl.*, 2011, 323–342.

109 V. A. Davankov, M. M. Ilyin, M. P. Tsyurupa, G. I. Timofeeva and L. V. Dubrovina, *Macromolecules*, 1996, **29**, 8398–8403.

110 D. A. Volkova and V. A. Andryushina, 2000, **33**, 601–603.

111 L. Fan, M. Li, Z. Lv, M. Sun, C. Luo, F. Lu and H. Qiu, *Colloids Surfaces B Biointerfaces*, 2012, **95**, 42–49.

112 D. Li and M. Ma, *Clean Prod. Process.*, 2000, **2**, 0112–0116.

113 R. Cavalli, F. Trotta and W. Tumiatti, *J. Incl. Phenom. Macrocycl. Chem.*, 2006, **56**, 209–213.

114 R. MacHín, J. R. Isasi and I. Vélaz, *Carbohydr. Polym.*, 2012, **87**, 2024–2030.

115 A. Anceschi, G. Magnacca, F. Trotta and M. Zanetti, *RSC Adv.*, 2017, **7**, 36117–36123.

116 M. . Donohue and G. . Aranovich, *Adv. Colloid Interface Sci.*, 1998, **76**–**77**, 137–152.

117 M. Zanetti, A. Anceschi, G. Magnacca, G. Spezzati, F. Caldera, G. P. Rosi and F. Trotta, *Microporous Mesoporous Mater.*, 2016, **235**, 178–184.

118 P. D. Archer, D. W. Ming and B. Sutter, *Planet. Sci.*, 2013, **2**, 1–21.

119 E. C. Arvaniti, M. C. G. Juenger, S. A. Bernal, J. Duchesne, L. Courard, S. Leroy, J. L. Provis, A. Klemm and N. De Belie, *Mater.*

Struct., 2015, **48**, 3687–3701.

120 D. P. Vargas, L. Giraldo and J. C. Moreno-Piraján, *J. Therm. Anal. Calorim.*, 2014, **117**, 1299–1309.

121 Z. Zhao, X. Cui, J. Ma and R. Li, *Int. J. Greenh. Gas Control*, 2007, **1**, 355–359.

122 J. Phillips, D. Kelly, L. Radovic and F. Xie, *J. Phys. Chem. B*, 2000, **104**, 8170–8176.

123 C. A. Grande, V. M. T. M. Silva and C. Gigola, 2003, **41**, 2533–2545.

124 F. A. Da Silva and E. Rodrigues, 1999, 2051–2057.

125 R. Fair, 1993, 2201–2207.

126 J. Padin, S. U. Rege, R. T. Yang and L. S. Cheng, 2000, **55**, 4525–4535.

127 A. Auroux, *Springer Series in Materials Science 154 Calorimetry and Thermal Methods in Catalysis*, .

128

129 B. Meyer, *Chem. Rev.*, 1976, **76**, 367–388.

130 S. H. Chung and A. Manthiram, *Adv. Funct. Mater.*, 2014, **24**, 5299–5306.

131 S. X. Zhao, N. Ta and X. D. Wang, *Energies*, , DOI:10.3390/en10091293.

132 A. R. A. Usman, A. Abduljabbar, M. Vithanage, Y. S. Ok, M. Ahmad, M. Ahmad, J. Elfaki, S. S. Abdulazeem and M. I. Al-Wabel, *J. Anal. Appl. Pyrolysis*, 2015, **115**, 392–400.

133 X. Wang, W. Zhou, G. Liang, D. Song and X. Zhang, *Sci. Total Environ.*, 2015, **538**, 137–144.

134 J. Zhang, F. Lü, C. Luo, L. Shao and P. He, *J. Environ. Sci. (China)*, 2014, **26**, 390–397.

135 X. Li, Q. Shen, D. Zhang, X. Mei, W. Ran, Y. Xu and G. Yu, *PLoS One*, , DOI:10.1371/journal.pone.0065949.

136 L. Lonappan, T. Rouissi, R. K. Das, S. K. Brar, A. A. Ramirez, M.

Verma, R. Y. Surampalli and J. R. Valero, *Waste Manag.*, 2016, **49**, 537–544.

137 S. Fan, J. Tang, Y. Wang, H. Li, H. Zhang, J. Tang, Z. Wang and X. Li, *J. Mol. Liq.*, 2016, **220**, 432–441.